

LASER-BASED DIAGNOSTICS ON NO IN A DIESEL ENGINE

Cover: A surrealistic impression of the rapidly advancing diesel engine technology as viewed from the author's perspective by kind courtesy of DAF Trucks

Laser-based diagnostics on NO in a diesel engine / Theodorus Maria Brugman.

Thesis Katholieke Universiteit Nijmegen. - Illustrated.

With references. - With summaries in English and Dutch.

ISBN 90-9012248-6

NUGI 812

Subject headings: laser spectroscopy / diesel engine / nitric oxide (NO) / laser-induced fluorescence (LIF) / imaging

LASER-BASED DIAGNOSTICS ON NO IN A DIESEL ENGINE

EEN WETENSCHAPPELIJKE PROEVE OP HET GEBIED VAN DE
NATUURWETENSCHAPPEN, WISKUNDE EN INFORMATICA

PROEFSCHRIFT

TER VERKRIJGING VAN DE GRAAD VAN DOCTOR
AAN DE KATHOLIEKE UNIVERSITEIT TE NIJMEGEN,
VOLGENS BESLUIT VAN HET COLLEGE VAN DECANEN
IN HET OPENBAAR TE VERDEDIGEN
OP WOENSDAG 13 JANUARI 1999
DES NAMIDDAGS OM 3.30 UUR PRECIES

door

THEODORUS MARIA BRUGMAN

geboren op 20 juli 1952
te Amsterdam

Promotor: Prof. Dr. J.J. ter Meulen

Co-promotores: Dr. N. Dam

Dr. W.L. Meerts

Manuscriptcommissie: Prof. Dr. D.H. Parker

Prof. Dr. Ir. R.S.G. Baert
Technische Universiteit Eindhoven

Dr. V. Sick
University of Michigan, USA

*Disputation is a proof
of not seeing clearly*

Chuang Tzu

Voor Boris, Bethany en Joke

This research is supported by the Dutch Technology Foundation (STW). The financial support of NOVEM B.V., Utrecht, The Netherlands and TNO, Delft, The Netherlands is gratefully acknowledged.

Voorwoord

Het zal eenieder ongetwijfeld wel duidelijk zijn dat de totstandkoming van dit boekje allerm minst een solo-project is geweest. Heel veel mensen hebben er direct of indirect aan bijgedragen en op deze plaats wil ik graag iedereen bedanken voor hun inbreng.

Op de eerste plaats komen de beide (inmiddels emeritus) hoogleraren Jörg Reuss en Ed van Walwijk die als initiatiefnemers en inspirators dit onderzoek op de rails hebben gezet. Jörg leverde een laserlab met welwillende promovendus en Ed stelde een dieselmotor beschikbaar voor een operatie waarvan vantevoren vaststond dat die motor hem nooit meer helemaal te boven zou komen. Vakbekwaam chirurg in kwestie was Gerrit Huigen die het inwendige van de motor optisch toegankelijk maakte met een constructie die alle zware beproevingen in de latere motorsessies met glans heeft doorstaan. Aanvankelijk slechts zeer bezielend begeleid door Hans ter Meulen die later in de hoedanigheid van hoogleraar Toegepaste Fysica mijn promotor zou worden, werd het dieselteam al spoedig uitgebreid met Leo Meerts en Nico Dam, mijn beide co-promotores. Ofschoon er gaandeweg tussen Leo en mij diepgaande verschillen in inzicht rezen met betrekking tot het schrijven van computerprogramma's, heeft dit onze verstandhouding noch de door mij geschreven programma's nimmer vertroebeld; het tegendeel is eerder waar. Het montere cynisme van Nico heeft mij bij voortduring geïnspireerd en gemotiveerd om zijn ongelijk te bewijzen. Dit lukte me slechts zeer zelden en daar ben ik achteraf natuurlijk heel erg gelukkig mee.

Dankzij een van de brainwaves van Eugène van Leeuwen kon de motor gesmeerd worden zonder daar in spectroscopische zin al te veel last van te hebben. Deze truc is cruciaal geweest voor het succes van het onderzoek dat daardoor in een continu vurende motor kon gebeuren. Heel veel dank, Eugène, en wat betreft onze gedeelde liefde voor de muziek van Django Reinhardt hou je nog wat van me tegoed. Het enthousiasme en het vakmanschap van Frans van Rijn resulteerde ondermeer in de onontbeerlijke en vlekkeloos verlopende elektronische synchronisatie van de laser- en de beeld-apparatuur met de interne bewegingen van de motor. Maar ik wil hem ook bedanken omdat hij altijd bereid was om zijn licht te laten schijnen op de elektronische probleempjes in mijn huis-studio. De deskundigheid van vader en zoon Reinier en Erik Merkus stond immer garant voor een snelle en doeltreffende eerste hulp in geval van rondvliegende oliepeilstokken en/of andere motoronderdelen. Zonder jullie hulp bij de veelvuldige vastlopers van de motor, en daarmee het onderzoek, zou dit boekje stellig nooit het licht hebben gezien. Ook kwartsspecialist Peter van Dijk verdient hulde voor het geduld en het vakmanschap waarmee hij, gelukkig vooral in de beginfase van het onderzoek, telkens opnieuw hoogwaardige vensters wist te produceren.

Speciale woorden van dank gaan uit naar Robert Klein-Douwel en Genie Stoffels, die allebei heel belangrijke rollen hebben gespeeld in verschillende perioden van het onderzoek. Niet alleen heeft Robert mij ingewijd in de geheimen van het Matrox-begeuren, ook later kon ik altijd op hem rekenen bij het bedwingen van de soms nogal weerbarstige meetopstelling. Men zegt wel dat het geniale idee om alle defect geraakte apparatuur gewoon uit het raam te gooien oorspronkelijk uit zijn brein ontsproten is, en ik als labgenoot kan dat volmondig beamen. Gelukkig heb ik hem meerdere malen ervan kunnen weerhouden om mijn dieselmotor de voorgestelde weg te laten volgen, waarschijnlijk omdat hij nog veel meer last had van de motor wanneer die niet defect was.

Maar ook *zijn* practical jokes mochten er wezen... Niettemin dank ik hem voor zijn kameraadschap en wens ik hem veel succes toe bij zijn huidige onderzoeksactiviteiten in Amerika. Genie wil ik graag bedanken voor haar morele steun in soms zeer barre tijden. Nooit eerder in mijn niet geringe arbeidsverleden heb ik zo nauw en toch prettig met iemand samengewerkt als met haar. Het is in dit verband opmerkelijk dat de welhaast Engelse discipline waarmee zij èn Robert theepauzes inlasten, mij als notoir koffiedrinker slechts zelden in de weg heeft gezeten. Naar het zich nu laat aanzien zal zij, maar een paar maanden na mij, als tweede promoveren op het dieselproject en ik wens haar dan ook veel sterkte en vooral wijsheid toe bij de afronding van haar dissertatie. Genie, bedankt voor alles en mochten jij en Giel nog eens in de buurt komen... (Ik denk dan aan de langste Vierdaagse afstand maar natuurlijk ook aan zo maar eens een aardig fietstochtje voor twee op een vrije middag...) We zullen in ieder geval, ook straks in het nieuwe huis, dat overigens nog dichterbij aan de Vierdaagse route ligt, wat lekkere exotische thee'tjes voor je in voorraad houden!

In later jaren werd het dieselteam verder uitgebreid met de altijd goed gehumeurde Charles Spaanjaars, die mij menigmaal op zeer plezierige wijze geholpen heeft om allerlei zaken in het gareel te houden. Korte tijd na Charles kwam een derde promovendus het team versterken in de persoon van Easy Jay alias Erik-Jan van den Boom. Zijn onderzoek in het zgn. Motorhome (het diesellab in de Graalburcht) richt zich op de verbranding in een heuse vrachtwagenmotor en ik wens zowel Charles als Erik-Jan veel geduld en sterkte toe bij het verwerken van de tegenslagen en het oplossen van de enorme problemen die er aan deze schaalvergroting blijken te kleven. Jongens, bedankt voor jullie humor en steun in de afgelopen jaren van noeste thuisarbeid en data-analyse...

Gaande het onderzoek rees de behoefte aan vergelijkende metingen onder beter controleerbare omstandigheden en voor dat doel is er een speciale meetcel ontwikkeld door een team van deskundigen bestaande uit Teun Diels, Albert Anijs en Jaap Nieboer onder leiding van Marius Kaptein. De eerste metingen in deze cel konden worden verricht in de laatste maanden van mijn aanstelling en tezamen met enige aanvullende metingen in de Graalburcht in de zomer van 1997 vormen zij een mooie afsluiting van dit proefschrift. Ik wil graag dit team bedanken voor hun inzet en hun vermogen om zich in te leven in de wensen van een vertrekkende promovendus onder tijdsdruk. Ook Ferry Derksen van de zelfservice, Wim Schut, Paul Walraven en Leander Gerritsen (nu op MOLAS werkzaam) van de instrumentmakerij alsook laserspecialist Christiaan de Snoo van Optilas wil ik graag bedanken voor hun bijdragen.

En natuurlijk wil ik alle mensen bedanken die in de afgelopen jaren de afdeling maakten tot een echte thuisbasis voor ploeterende promovendi: Annette van der Heijden en haar opvolgster Magda Speijers; Gerard Meijer; Dave Parker; Cor Sikkens, die poster van het Abu Simbel complex in Zuid-Egypte hangt nog steeds boven onze piano; Chris Timmer; John Holtkamp; Patricia Huisman-Kleinherenbrink, ondermeer voor haar prettig gezelschap en de perfecte voorbereiding van de werkcolleges die ik mocht geven; Harold Linnartz; Arjen Linskens; Maarten Boogaarts; Ger van den Hoek; Marc Jonkers; Jean Schleipen; Karen Remmers; Giel huppekee Berden; Erik Vrijenhoek; Frans Harren; Huug de Vries; Frans Bijnen; André Eppink; Rienk Jongma; Iwan Holleman; Mike Putter; Jack van Rooij; Richard Engeln; Jules Spaanjaars, ja, oudere broer van; Sacco te Lintel Hekkert, altijd te porren voor een weddenschap; Jos Oomens, tekstschrijver en medeproducer van onze helaas nimmer uitgebrachte House-hit; Marcel Drabbels, bedenker van de geheel voor zijn

rekening komende classificerende term: IR-boer; de immer schrandere en plezierige kamergenoot Koen Schreel, king of BIOS setups; Adrian AEX Marijnissen, ook een prettige kamer- en tevens perron nul-genoot, impresario van zangeressen voor House-hits en nu ongetwijfeld al optie-beursbengel in ruste en, tot slot, de aan de wel zeer uitgekiende combinatie van broodjes shoarma en elektronische babbelboxen verslaafde Patrick Schmidt.

Mijn laatste maar zeker niet de minste woorden van dank gaan uit naar mijn ape-trotse ouders en schoonouders die steeds, voor zover dat in hun vermogen lag, mijn verrichtingen op de voet volgden; naar mijn beide broertjes met hun gezinnen voor hun begrip voor het veel te sporadische contact in de laatste jaren en naar Joke voor haar geduld en medeleven met de bij tijd en wijle behoorlijk verstrooide echtgenoot die ik voor haar geweest ben. Bedankt voor je voortdurende steun en je onwankelbare vertrouwen in de goede afloop, lieverd! Bovendien heb je me nog twee ontzettend lieve kindertjes geschonken en aan hun en jou draag ik dan ook graag dit proefschrift op.

Arnhem, 16 november 1998

CONTENTS

1	GENERAL INTRODUCTION	1
1.1	Environmental considerations	2
1.2	Laser-based imaging diagnostics in i.c. engines	4
1.3	Laser-induced fluorescence spectroscopy of NO and its imaging	6
1.3.1	Laser-induced fluorescence	6
1.3.2	Rate equations	9
1.3.3	Imaging	13
1.4	Outline	14
2	RELEVANT EXPERIMENTAL TOPICS	15
2.1	The ArF excimer laser	15
2.2	The engine	17
2.3	The reflection filter	19
2.4	Imaging setup	20
3	LASER-INDUCED FLUORESCENCE IMAGING OF NO IN AN n-HEPTANE AND DIESEL-FUEL-DRIVEN DIESEL ENGINE	23
3.1	Introduction	23
3.2	Experimental	24
3.3	Results and discussion	27
3.4	Summary	34
4	IMAGING AND POST-PROCESSING OF LASER-INDUCED FLUORESCENCE FROM NO IN A DIESEL ENGINE	35
4.1	Introduction	35
4.2	Experimental	36
4.2.1	The essentials	36
4.2.2	The measuring sequence	38
4.2.3	The double resonance setup	39
4.3	Signal processing	40
4.4	Results and discussion	45
4.4.1	Validation of the detection method	45
4.4.1.1	Two-colour excitation	45
4.4.1.2	Dependence of the LIF signal on laser power	46
4.4.1.3	Saturation	48
4.4.2	NO distributions in the running engine	48
4.5	Summary	52

5	APPROACHES TO THE QUANTITATIVE INTERPRETATION OF LASER-INDUCED FLUORESCENCE FROM NO IN AN IDI DIESEL ENGINE	55
5.1	Introduction	55
5.2	Experimental	56
5.3	Modelling	58
5.4	Results and discussion	60
5.4.1	Excitation spectra	60
5.4.2	In-cylinder NO distributions	62
5.4.3	NO density versus crank angle	67
5.5	Summary and conclusions	70
6	LASER-INDUCED FLUORESCENCE YIELD FROM $D^2\Sigma^+$ NO IN N_2 AND AIR AT ELEVATED TEMPERATURES AND PRESSURES	71
6.1	Introduction	71
6.2	Experimental	72
6.3	Data reduction	74
6.4	Results and discussions	75
6.4.1	Excitation spectra at atmospheric pressure	76
6.4.2	Higher pressure excitation spectra	81
6.4.3	Data analysis	87
6.5	Summary and conclusions	91
7	EPILOGUE	93
	References	99
	Summary	103
	Samenvatting	105
	Appendix - Engine data	107
	Curriculum Vitae	109
	Publications	111

Chapter 1

General Introduction

In 1897 Rudolf Diesel (1858-1913) demonstrated a new type of internal combustion (i.c.) engine in which the high compression pressure of about 35 times the atmospheric pressure led to a sufficiently high temperature to cause the auto-ignition of kerosine. Ever since diesel engines remained popular owing to their relatively high efficiencies and their ability to combust a large variety of fuels predominantly containing heavier crude oil components (i.e., longer aliphatic hydrocarbon chains). The original engines were 4-stroke engines in which one complete engine cycle takes two revolutions of the crank shaft. The latter transforms the translational energy of the piston in the cylinder into more convenient rotational energy with respect to vehicle propulsion. As schematically depicted in figure 1.1, in the first stroke the piston moves downwards in the cylinder and ambient air is taken in above the piston (inlet stroke). In the second stroke the inlet valve is closed and the piston moves upwards compressing the intake air (compression stroke). Just before the piston reaches its Top Dead Centre (TDC) fuel is sprayed in the combustion chamber and combustion takes place driving the piston downwards again in the third stroke (expansion stroke). Finally, the exhaust valve opens and the piston moves upwards again in the fourth stroke (exhaust stroke) pushing the combustion gases out of the cylinder. In later years 2-stroke diesel engines were developed in which, by using the space of the crank case below the piston as well, the work usually done in four strokes is now performed by one revolution of the crank shaft. Around 1940 the first turbo-charging diesel engines were developed in which the energy contained in the exhaust gases is used to compress the intake air in order to boost the power of the engines.

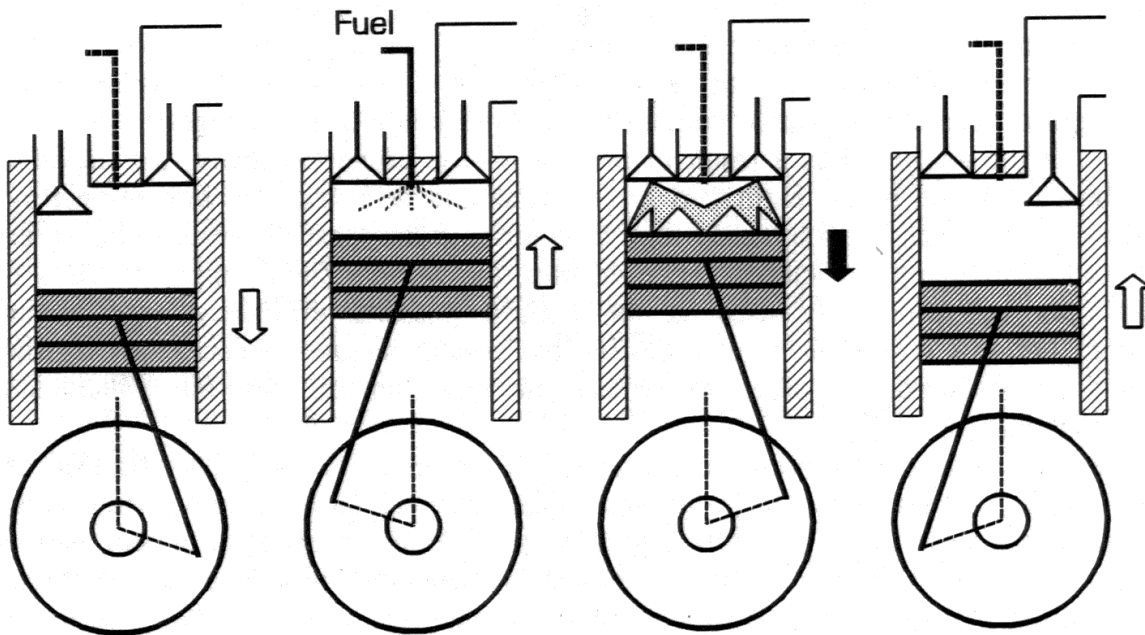


Figure 1.1 *Schematic of the 4-stroke diesel engine cycle*

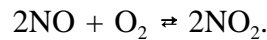
However, the high combustion temperatures in diesel engines also cause the formation of polluting exhaust gas components like sulphur oxides, nitrogen oxides and soot particles. Nowadays, engine developers are also facing the serious environmental challenge to drastically reduce the toxic emissions of their engines while maintaining the high efficiency. Fortunately, as technology progresses new laser-based research techniques allow for the detailed study of the physics and the chemistry of the combustion process itself in order to fight against toxic emissions at their very source. The objective of the experiments reported in this thesis was the development of non-intrusive laser-based diagnostic techniques by means of which the cycle-averaged in-cylinder NO distributions in an optically accessible IDI (InDirect Injection) diesel engine can be visualized as a function of the engine operating conditions. By imaging the Laser-Induced Fluorescence (LIF) from NO molecules in a plane in the cylinder, the distribution of these molecules within that plane can be measured on a nanosecond time scale. The intensity of the LIF signal generally depends on a number of spectroscopic and experimental parameters, the local density of NO molecules, the local laser intensity, the temperature and the pressure of the combustion gas as well as on the chemical composition of the latter. These dependencies vary from relatively simple linear ones for the local NO density and the local laser intensity to much more complicated relations for the other parameters. The various experiments reported in this thesis focus on both the validation of the 2D-LIF detection method and the detailed study of the dependence of the LIF signal on the mentioned parameters in order to correct and quantify the essentially qualitative LIF results.

1.1 Environmental considerations

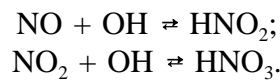
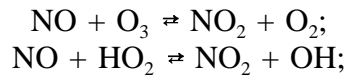
Massive amounts of nitrogen oxides (causing acid rain) are emitted into the environment as a result of the ever increasing energy consumption by the industrialized part of the world. The even larger amounts of carbon dioxide produced in the combustion of fossil fuels by powerhouses and internal combustion engines might cause changes in the climatic condition of the world [1] as a result of the greenhouse effect (basically, the impediment of the heat reflection of the earth into space). It should be noted that with respect to the i.c. engines diesel engines obviously tend to contribute the least to the greenhouse effect as a result of their high efficiency [1]. Evidently, the world's finite supply of fossil fuels should only be responsibly used at the highest possible efficiency with minimum pollution. For this reason, in most industrialized countries governments enact legislation on emission standards in order to protect the environment. Not all contamination, however, is man-made.

As far as nitrogen oxides are concerned forest fires, initiated either by man or by natural causes, are estimated to be at least equally damaging to the environment as the combustion of fossil fuels [2]. On a smaller scale other sources of global NO_x are: lightning, volcanic activity and the oxidation of ammonia produced during bacterial decomposition of proteins [2]. However, of all combustion sources of NO_x the road and air traffic in the industrialized countries is by far the most polluting [2]. Although seven nitrogen oxides are known (NO , NO_2 , NO_3 , N_2O , N_2O_3 , N_2O_4 and N_2O_5) the nitrogen oxides resulting from the combustion of fossil fuel are mainly NO and NO_2 with NO typically representing 90 to 95% of the total NO_x in the combustion gas [2]. At

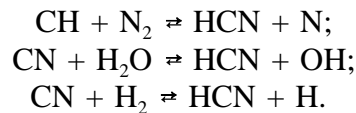
atmospheric conditions NO readily further oxidizes to NO₂ via [3]



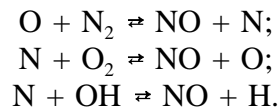
The acidification of the environment by nitrogen oxides in the higher layers of the atmosphere mainly is the result of reactions with ozone and photochemically generated peroxy and hydroxyl radicals [2,4]



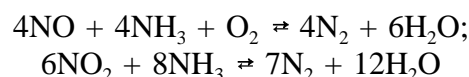
Generally, three intermediate types of exhaust NO are distinguished: prompt NO, fuel NO and thermal NO. Although still subject to study one of the possible causes of prompt NO is the oxidation of HCN which is intermediately produced in the combustion via [2]



Fuel NO originates from the gas-phase oxidation of nitrogen containing compounds of the fuel. Thermal NO is formed by fixation of atmospheric nitrogen via the Zeldovich mechanism consisting of three primary reactions [2]



The contribution of each of these three sub-mechanisms to NO emission probably depends on fuel-type, temperature, pressure and stoichiometry of the combustion. Over the years a number of combustion modification techniques like the reduction of fuel nitrogen levels, the decrease of oxygen levels at peak temperatures, the reduction of these peak temperatures themselves (e.g. by injecting water or steam) and EGR (Exhaust Gas Recirculation) have proved to be reasonably successful in reducing exhaust NO_x levels [5]. For obvious practical reasons the catalytic or non-catalytic reduction of NO_x levels by ammonia via [2]



is less suitable for implementation in non-stationary i.c. engines with their large range of operating conditions and researchers are still working on this problem. In Europe the present 7 g/kWh (Euro-2) NO_x emission standards for trucks will be sharply reduced to 3 g/kWh in the year 2004 (Euro-4). This drastic reduction of tail-pipe NO_x levels requires intense research efforts directed towards a better understanding of the chemically very

complex combustion processes.

1.2 Laser-based imaging diagnostics in i.c. engines

At this point in time, increasingly powerful lasers and ever faster detection systems are being developed, allowing for the non-intrusive detailed study of combustion processes on a nanosecond time scale in rather inhospitable research environments, such as in large-scale high-pressure industrial flames and in combustion chambers of optically accessible i.c. engines. Presently, owing to its high sensitivity for minority constituents of the combustion gases, the LIF detection is among the most commonly used techniques in obtaining molecule-specific information from combustion systems. In short, laser-induced fluorescence is the emission of light from an atom or a molecule following promotion to an electronically-excited state by the absorption of laser photons. Besides being used in the detection of many important combustion minority species like CN, CH, NH and CO, this technique has already proved to be of great value in the detection of NO and OH in i.c. engine studies as well [6-14]. The LIF spectroscopy of NO and its imaging will be extensively discussed in the next section.

As for the LIF studies of NO in diesel engines most of the research is performed with low-sooting substitute fuels in order to preserve the transparency of the access channels, therewith facilitating longer measuring times, while the attenuation of the laser beam by absorbing and scattering particles is minimized as well. Arnold *et al.* [7] and Hentschel *et al.* [10] performed LIF imaging experiments in an optically accessible 4-cylinder 1.9 litre DI (Direct Injection) passenger car diesel engine using n-heptane as fuel, whereas Alataş *et al.* [8] and Nakagawa *et al.* [14] use a 50-50 mixture of iso-octane and n-tetradecane in their single cylinder test engines. The 1.6 litre DI test engine of Nakagawa *et al.* [14] was also fuelled with a 40-60 mixture of ethyl alcohol and n-dodecane. Some of the (first) experiments reported in chapter 3 of this thesis were also performed using n-heptane as fuel; however, the engine experiments reported in the chapters 4 and 5 were performed in the 0.6 litre IDI single cylinder test engine pertinent to this work using standard diesel fuel. In contrast to the experiments of Alataş *et al.* [8], Nakagawa *et al.* [14] and the engine experiments described in this work, Arnold *et al.* [7] and Hentschel *et al.* [10] did not supply extra oxygen to the air inlet of their engines and, nevertheless, they succeeded in maintaining a high transparency of the windows for several minutes. They present 30-cycles averaged NO fluorescence distributions at in-cylinder pressures of 0.5 and 5 MPa. Alataş *et al.* [8] added about 10% extra oxygen to the intake-air and in order to even further reduce the window fouling by soot depositions their 0.6 litre DI test engine was operated in the skip-fired mode (i.e., the engine was fired every sixth cycle). These authors present 50-cycles averaged NO fluorescence distributions at moderate in-cylinder pressures (not specified). Nakagawa *et al.* [14] supplied up to 15% extra oxygen to their continuously firing engine and they present 5-cycles averaged NO fluorescence distributions at in-cylinder pressures of about 6 MPa. However, the extra 10-15% oxygen taken in by the test engine during the imaging experiments reported in this thesis allowed for high transparencies of the windows for an almost unlimited period of time. As a result of this feature, several NO excitation scans from the idling and the loaded engine with a recording time of about 15-20 minutes each are presented in the chapters 3 and 5 of this work.

It should be noted that for NO, being a more or less stable molecule, the overall in-cylinder concentration can also be measured directly by applying sophisticated in-cylinder gas-sampling techniques [10,15]. Hentschel *et al.* [10] observed a steadily increasing NO concentration during the first part of the expansion stroke. At full load of the engine (66 kW at 4000 rpm) the in-cylinder NO concentration reached its maximum value of about 1800 ppm at 30° ATDC (After Top Dead Centre) whereas with part load a lower maximum value of about 700 ppm is reached about 15° sooner. Note that in these experiments the injection timing was adjusted to the load: at full load fuel injection started around 8° BTDC (Before Top Dead Centre) whereas at part load the injection was about 6° retarded. Donahue *et al.* [15] observed a very similar behaviour of the in-cylinder NO concentration in their turbo-charged 1.2 litre DI test engine and according to these authors the most important measures for NO_x reduction in (turbo-charged) diesel engines remain to be: retarded injection timing, lower intake-air temperature, boosted inlet pressure, EGR and fuel reformulation.

By adding fluorescing tracers to the fuel or, in some cases, by selecting the proper laser wavelength, the temporal behaviour of the fuel sprays in optically accessible combustion chambers has been widely studied [16-20]. However, dopants must be selected with great care with respect to the relevant fuel properties (e.g. vapour pressure, molecular diffusion constants). For instance, Neij *et al.* [20] studied fuel behaviour in an iso-octane driven diesel engine using a KrF excimer laser at 248 nm and 3-pentanone as fluorescing tracer. Arnold *et al.* [7] report fluorescence from commercial diesel fuels induced by a XeCl excimer laser at 308 nm. The information obtained from the fuel spray studies may have a large impact on the understanding of the emission levels of, in particular, soot particles and NO_x. If the injected fuel is not completely burned in the combustion large amounts of soot particles will be emitted at the exhaust. On the other hand if the combustion temperature is too high (e.g. as a result of the stoichiometry) large NO_x emissions are observed whereas the soot concentration is reduced (see e.g. [1,8]). Due to the complexity of the fuel-air mixing process a slightly altered position of the injectors or a change in the nozzle configuration may easily lead to very different combustion conditions. LIF studies of fuel spray behaviour are often combined with high-speed camera techniques, imaging either the natural luminosity of the combusting fuel plume or the scattering of a laser light-sheet or both simultaneously.

The formation of soot particles in i.c. engines may also be studied by imaging the resonantly scattered laser light [17-19]. Depending on the ratio of the average size of the scattering particles and the laser wavelength the scattering is called Rayleigh scattering (particle diameter smaller than or about equal to the laser wavelength) or Mie scattering (particle diameter larger than the laser wavelength). Since in the Rayleigh regime the scattered intensity is proportional to the density as well as to the average diameter of the scatterers to the sixth power [17], this method, unfortunately, cannot be used to acquire information on either variable alone. If, however, at a given crank angle all soot particles are assumed to be equally sized the scattered signal provides direct information on the soot density distribution.

Presently, in-cylinder soot distributions are also studied by imaging the Laser-Induced Incandescence (LII) resulting from the pulsed laser-heating of soot particles to temperatures around 4000 K far above the typical background temperature of about 2000 K [21-26]. Generally, the emitted radiation is assumed to be black- or grey-body radiation governed by Planck's law. However, whether LII is a non-intrusive or an intrusive

technique depends mainly on the laser pulse energy employed and the average particle size since smaller soot particles are easily vaporized if the laser intensity is too high [22]. At high laser intensities the LII signal depends on the density of soot particles as well as on the cubed average particle diameter [21]. The combination of LII with scattering techniques in the Rayleigh regime then permits the determination of average particle sizes since the ratio of the scattered signal from a particle in the imaged area and the LII signal from the same particle will be proportional to the average particle diameter to the third power [23]. However, the large range of soot particle sizes usually present in diesel engines considerably complicates the interpretation of both elastic scattered images and LII images [24,25].

Non-intrusive laser-based diagnostic techniques such as Coherent Anti-Stokes Raman Spectroscopy (CARS) and Degenerate Four Wave Mixing (DFWM) should be mentioned here as well for their use in combustion studies. Due to its relatively low sensitivity the applicability of CARS is limited to point-measurements, while the reported sensitivity of Raman spectroscopy for interfering incandescence [22,27], as inevitably present in i.c. engines, complicates the applicability of CARS to engine combustion research even further. Although DFWM is relatively simple to implement for planar imaging, the latter is still in its infancy as far as combustion diagnostics is concerned [28], especially in turbulent environments.

Finally, although not an imaging technique, Laser Doppler Velocimetry (LDV) should be mentioned as a laser-based diagnostic tool for its wide application in studies of the complicated gas flows in (motored) engines. Two coherent laser beams are crossed in the focus of the same lens with a small intersection angle generating an interference pattern in the beam intersection region similar to the grating formed by DFWM. This pattern consists of equally spaced straight light and dark lines viewed in the plane perpendicular to the plane of the laser beams. When a small particle passes through this fringe pattern, it will resonantly scatter light with a frequency which is directly proportional to the velocity component normal to the fringes. By introducing a slight frequency difference between the two crossed beams, the fringes will move in space, allowing for the detection of the direction of the particle motion. By generating two orthogonal and coincident fringe patterns (using two different laser wavelengths) two orthogonal velocity components of the particle motion may be determined simultaneously. However, LDV is an intrusive technique because, for optimum performance, it requires the seeding of the gas flows with particles of about 1 μm diameter (e.g. the fine powder of titanium dioxide). Larger particles may not adequately follow the dynamics of the combustion flows [29].

1.3 Laser-induced fluorescence spectroscopy of NO and its imaging

1.3.1 Laser-induced fluorescence

The LIF spectroscopy of NO has been widely and extensively studied in steady and unsteady combustion systems using various excitation wavelengths. As a result of many theoretical and experimental research efforts over the last two decades most of the spectroscopic observations are well understood. Current modelling includes detailed spectral simulation [30] using experimentally verified molecular spectroscopic constants [31] and pressure and temperature dependent collisional quenching parameters [32].

Besides in the studies of in-cylinder NO mentioned in the previous section, the LIF detection technique has also been successfully applied in heated or cooled cells at lower pressures [33-42] as well as in flames at atmospheric [43-45] and higher pressures [46-49]. Most of these authors also validate their modelling with experimental data and inspired by the close match of theory with experiment, even calibration procedures for NO LIF measurements in high-pressure flames are proposed [50] demonstrating the maturity of this technique.

The different vibronic transitions of NO in the electronic $X^2\Pi$ ground state are illustrated by the set of NO potential energy curves as shown in figure 1.2. Note that the potential energy curves of the $C^2\Pi$ state and the $D^2\Sigma^+$ state are represented by one and the same curve as the energy differences between the states are too small to be shown in this figure. The most frequently used vibronic transition in LIF studies of NO is the $A^2\Sigma^+(v'=0) \leftarrow X^2\Pi(v''=0)$ transition around 226 nm interrogating rotational sub-levels of the lowest lying vibrational level in the electronic ground state. Alternatively, the $D^2\Sigma^+(v'=0) \leftarrow X^2\Pi(v''=1)$ transition around 193 nm by means of which rotational sub-levels of the first vibrational level in the ground state are probed is used as well. In the same wavelength region around 193 nm the $B^2\Pi(v'=7) \leftarrow X^2\Pi(v''=0)$ and the $A^2\Sigma^+(v'=3) \leftarrow X^2\Pi(v''=0)$ transitions may also be invoked. Recently, Schulz *et al.* [11] and Knapp *et al.* [12] investigated the use of 248 nm to induce the $A^2\Sigma^+(v'=0) \leftarrow X^2\Pi(v''=2)$ transition in i.c. engines probing the second vibrational level of the NO ground state.

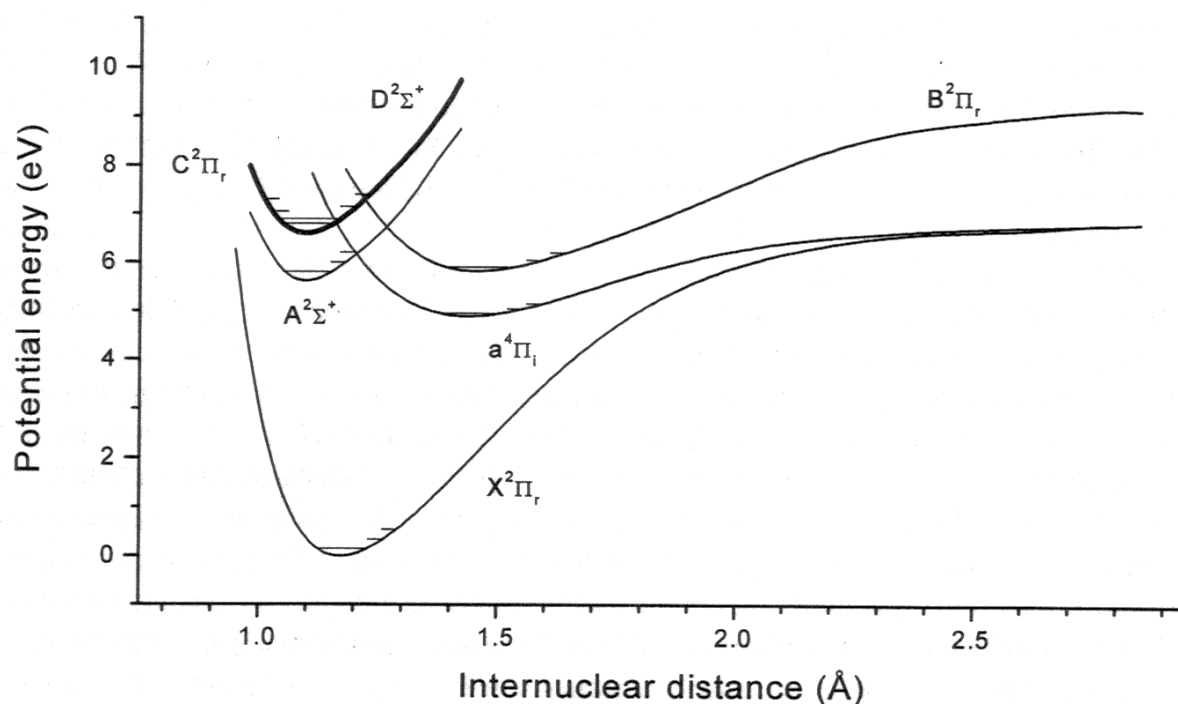


Figure 1.2 Molecular potential energy curves of relevant NO electronic states. The nearly coinciding energy curves of the $C^2\Pi$ state and the $D^2\Sigma^+$ state are represented by the one curve drawn. The vibrational energy levels are indicated on the left hand side and the right hand side for the $C^2\Pi$ state and the $D^2\Sigma^+$ state, in that order

The LIF signal from any rovibronic transition is proportional to the population number density of the probed rovibrational level in the electronic ground state. Provided saturation does not occur the LIF signal will also be proportional to the line strength of the transition as well as to the incident laser intensity. The line strength contains the Franck-Condon and Hönl-London factors for the selected transition and from fig. 1.2 it is evident that the vibrational overlap of the B state and the ground state is rather poor leading to relatively weak LIF signals from the $B^2\Pi(v'=7) \leftarrow X^2\Pi(v''=0)$ transition at 193 nm excitation. At these very wavelengths, the $A^2\Sigma^+(v'=3) \leftarrow X^2\Pi(v''=0)$ transition is only accessible for rotational quantum numbers starting at 30.5 and due to the relatively long lifetime of the A state, quenching of the fluorescence from this transition will be considerable [44]. This leaves the $D^2\Sigma^+(v'=0) \leftarrow X^2\Pi(v''=1)$ transition dominant at 193 nm excitation. Thus, the three lowest vibrational states ($v''=0,1,2$) in the electronic ground state of NO may be probed by 226 nm, 193 and 248 nm, respectively. However, in view of the strong in-cylinder laser extinction as generally observed in engine combustion studies, the maximum available laser intensity in each wavelength region needs to be considered. Whereas 226 nm radiation most commonly is generated by frequency doubling the output of a Nd:YAG pumped dye laser leading to relatively low laser pulse energies (typically 1 mJ/pulse), more powerful tunable ArF excimer lasers readily provide 193 nm pulses (typically 100 mJ/pulse) and even more powerful tunable KrF excimer lasers deliver 248 nm radiation (typically 250 mJ/pulse) with which in the same experiment the LIF signal from the OH $A^2\Sigma^+(v'=3) \leftarrow X^2\Pi(v''=0)$ transition may be studied as well. Lee *et al.* [40] report an about one order of magnitude larger Franck-Condon factor for the $D^2\Sigma^+(v'=0) \leftarrow X^2\Pi(v''=1)$ transition compared with the $A^2\Sigma^+(v'=0) \leftarrow X^2\Pi(v''=0)$ transition and in case no saturation occurs this obviously will directly affect the LIF signal strength of both transitions. However, from Boltzmann statistics it follows that at any given temperature the population number density of the different vibrational states rapidly decreases with increasing vibrational quantum number. As will be shown in chapter 5, besides implications for the overall LIF signal strength, in imaging studies this may also lead to different local sensitivities of the 2D-LIF signal in case of temperature gradients within the imaged area.

Generally, depopulation of the electronically-excited state may occur through a large variety of processes: spontaneous emission (fluorescence) to many different rovibrational levels in the electronic ground state, stimulated emission back to the probed rovibrational level in the ground electronic state, collisional quenching (collisional transfer to the electronic ground state), Rotational Energy Transfer (RET), Vibrational Energy Transfer (VET), Electronic Energy Transfer (EET), photoionization and photo-dissociation. The resulting fluorescence efficiency is commonly expressed as $A/(A+Q+L)$ in which A represents the Einstein coefficient for spontaneous emission (s^{-1}). Q stands for the collisional quenching rate, generally depending on gas composition, pressure and temperature. For practical reasons, in most studies the fluorescence losses as a result of multiphoton ionization and the various other energy transfer mechanisms are represented by a fluorescence loss rate L. Since the excited A, D and B states of NO are not predissociative the predissociation rate, in principle also contributing to L, is negligibly small. In this respect, it should be noted that the C state (slightly below the D state) is strongly predissociative for rotational levels above $J=5.5$ in the lowest vibrational state as a result of the crossing of its energy curve with the repulsive limb of the $a^4\Pi$ potential energy curve [35]. This crossing occurs below the lowest rovibrational level in the D state and, thus, the character of the quenching from this state is not directly affected. However,

EET is responsible for a significant population leakage from the D state to the C state. In fact, to our own observation and that of Wodtke *et al.* [43] at atmospheric pressure the dispersed LIF signal from the C state is observed to be as strong as about 25-50% of the LIF signal from the exclusively excited D state itself. Especially in view of the predissociative character of the C state, this strong C→X fluorescence is indicative for a fairly efficient D-C coupling indeed. Note that the mechanisms represented by L are independent of the actual gas pressure and that at atmospheric and higher pressures Q generally is much larger than A+L. With these considerations the fluorescence efficiency factor (or Stern-Vollmer factor) effectively reduces to A/Q. The collisional quenching rate is usually modelled as to be proportional to the density of colliding species, to the colliding species specific averaged temperature dependent quenching cross section as well as to the averaged Maxwellian velocity of the collision partners.

The current state of knowledge includes spectroscopic constants like the Einstein coefficients as well as the Franck-Condon and Hönl-London factors for all relevant NO transitions. With these data excitation spectra of the various transitions may be simulated in great detail [30]. However, the effects of RET and VET processes in the electronically-excited state as well as in the ground state are still subject to study. Whereas 226 nm A→X excitation spectra may be simulated including experimental data on the quenching parameters as well, such comprehensive data on D→X quenching parameters are not yet found in literature. The lack of these quenching parameter data considerably complicates the quantitative interpretation of the LIF signals at 193 nm excitation. However, by adapting a fluorescence model from 226 nm NO excitation studies the essentially qualitative results of the 2D-LIF measurements in the running test engine reported in chapter 5 may be transformed into semi-quantitative data. In chapter 6 a first approach to assess this problem of unknown collisional quenching from an empirical point of view is made on the basis of calibration 2D-LIF measurements of NO in a heated high-pressure cell.

1.3.2 Rate equations

A schematic of a simplified two-state model of the LIF process is given in figure 1.3 in which the excited state is labelled 1 and the electronic ground state is labelled 2. Each state interacts with a bath driving the population of the states to their equilibrium values. These interaction rates are γ_1 and γ_2 , respectively. The bath associated with the excited state drains the population from the excited rovibrational state and γ_1 represents the total efficiency of EET, collisional quenching, VET and multiphoton processes in this state. Since the spectrally filtered fluorescence is not rotationally resolved, RET processes in the excited state do not affect the observed LIF signal strength. However, in case of narrow bandwidth excitation it should be noted that these RET processes are believed to be fast enough [50] to literally kick excited molecules out of resonance for stimulated emission. The bath associated with the electronic ground state continuously replenishes the ground state population and γ_2 represents the VET and RET processes responsible. Usually, the spectrally filtered fluorescence from a specific vibronic transition to another vibrational state in the ground state is selected for imaging. This vibrational state is labelled 3 in fig. 1.3. Molecules are excited by the laser at a pump rate $B_{21}W$ and stimulated emission on the same transition occurs at a rate $B_{12}W$. In the case of a Q-type rotational transition the rotational degeneracies of both states are the same and B_{12} may be set equal to B_{21} .

However, as mentioned before, depending on the excitation bandwidth RET processes in the excited state may effectively reduce the stimulated emission. In this respect, it should be noted that the combined collision and Doppler NO linewidth greatly exceeds the power-broadened radiative linewidth of the NO D–X transitions and that, consequently, besides for broadband excitation the rate equation model also is valid for the narrow bandwidth excitation [51] as pertinent to this thesis.

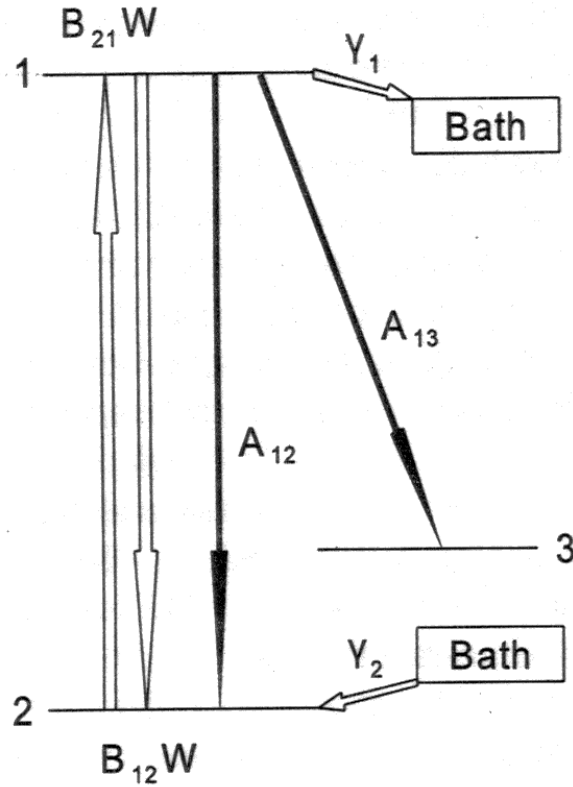


Figure 1.3 An outline of the two-state model of the LIF process

By assuming a rectangular laser pulse with respect to time, the rate equations describing the temporal behaviour of the populations in both states are

$$\frac{dN_1}{dt} = -(A_{12} + A_{13} + B_{12}^*W)N_1 + B_{21}WN_2 - \gamma_1(N_1 - N_1^{\text{eq}}) \quad (1.1)$$

$$\frac{dN_2}{dt} = +(A_{12} + B_{12}^*W)N_1 - B_{21}WN_2 - \gamma_2(N_2 - N_2^{\text{eq}}) \quad (1.2)$$

with A_{12} and A_{13} as the Einstein coefficients of spontaneous emission (s^{-1}), B_{21} and B_{12}^* as the Einstein coefficient of stimulated absorption and the effective Einstein coefficient of stimulated emission ($\text{cm}^2 \text{cm}^{-1} \text{J}^{-1}$), respectively, and W as the spectral intensity of the laser ($\text{J cm}^{-1} \text{s}^{-1}$). With respect to B_{12}^* and B_{21} it should be noted that these Einstein coefficients can be seen as the averages over all rotational states coupled by excited state and ground state RET processes, respectively. Finally, N_1^{eq} and N_2^{eq} stand for the equilibrium

populations of both rovibronic states and, obviously, $N_1^{\text{eq}}=0$. This set of coupled differential equations can be solved analytically as to produce the population number densities $N_1(t)$ and $N_2(t)$ in terms of the relevant parameters. At any time the LIF signal is proportional to $\sum_i[A_{i3}N_i(t)]$ with i representing all rotational states coupled by excited state RET and by time-integrating this term the overall observed fluorescence yield may be assessed. However, the (rotationally resolved) D state RET rates involved in the summation are not yet known and as a consequence, in this study the term $A_{i3}N_i(t)$ is considered instead.

The NO transitions of main interest in this thesis are rotational resonances of the $D^2\Sigma^+(v'=0) \leftarrow X^2\Pi(v''=1)$ transition invoked at 193 nm excitation and to date only very few parameters with respect to EET, collisional quenching, RET and VET in the excited D state are known. In anticipation of future experimental data the model is made fully parametric, i.e., all bath interaction, emission and absorption rates are expressed in terms of the laser pump rate $B_{21}W$. Regarding this pump rate generally two regimes are distinguished. In the high laser power regime the laser pump rate exceeds the sum of all depopulation rates of the excited state, i.e., $B_{21}W \gg (\sum_i A_{i1} + \gamma_1)$, whereas in the low laser power regime obviously the reverse situation occurs. However, considerations on the topic of saturation as given in section 4.1.3 of this thesis indicate that most of the imaging experiments in this work are performed in the high laser power regime at the verge of saturation. This allows the rate equations (1.1) and (1.2) to be written as

$$\frac{1}{B_{21}W} \frac{dN_1}{dt} = -P_3N_1 + N_2 - P_1N_1 \quad (1.3)$$

$$\frac{1}{B_{21}W} \frac{dN_2}{dt} = +P_3N_1 - N_2 - P_2(N_2 - N_2^{\text{eq}}) \quad (1.4)$$

with

$$P_1 = \frac{\gamma_1}{B_{21}W} \quad ; \quad P_2 = \frac{\gamma_2}{B_{21}W} \quad ; \quad P_3 = \frac{B_{12}^*W}{B_{21}W} \quad (1.5)$$

The LIF yield is evaluated by time-integrating the analytical solution $N_1(t)$ of this set of rate equations and the results for various values of the parameters P_1 , P_2 and P_3 are given in figure 1.4. The values are chosen in such a way as to include the expected experimental situation assessed in chapter 4 of this work: $P_1=1$, $P_2=1$ and $P_3=1$ ¹.

¹ In a two-level system the saturation parameter S is defined as the ratio of the laser pump rate $B_{21}W$ and the mean relaxation rate $(\gamma_1 + \gamma_2)/2$ [56]. From the discussion in section 4.3.1 of this thesis, S is estimated to be around unity and it follows that $(\gamma_1 + \gamma_2)/2 \approx B_{21}W$ which, in turn, leads to $(P_1 + P_2)/2 \approx 1$. Considering the additional interaction mechanisms in the excited state (EET and collisional quenching) P_1 is expected to be larger than P_2 and, consequently, the evaluation is performed for various values of the ratio P_1/P_2 ranging from 1 (i.e. by setting $P_1 \approx P_2 \approx 1$) to 10 where P_2 is varied over an order of magnitude. Obviously, the value of P_3 is expected to be around unity. However, as to study the effect of excited state RET on the stimulated emission probability in the more practical case of narrow bandwidth excitation, some smaller P_3 values are evaluated as well.

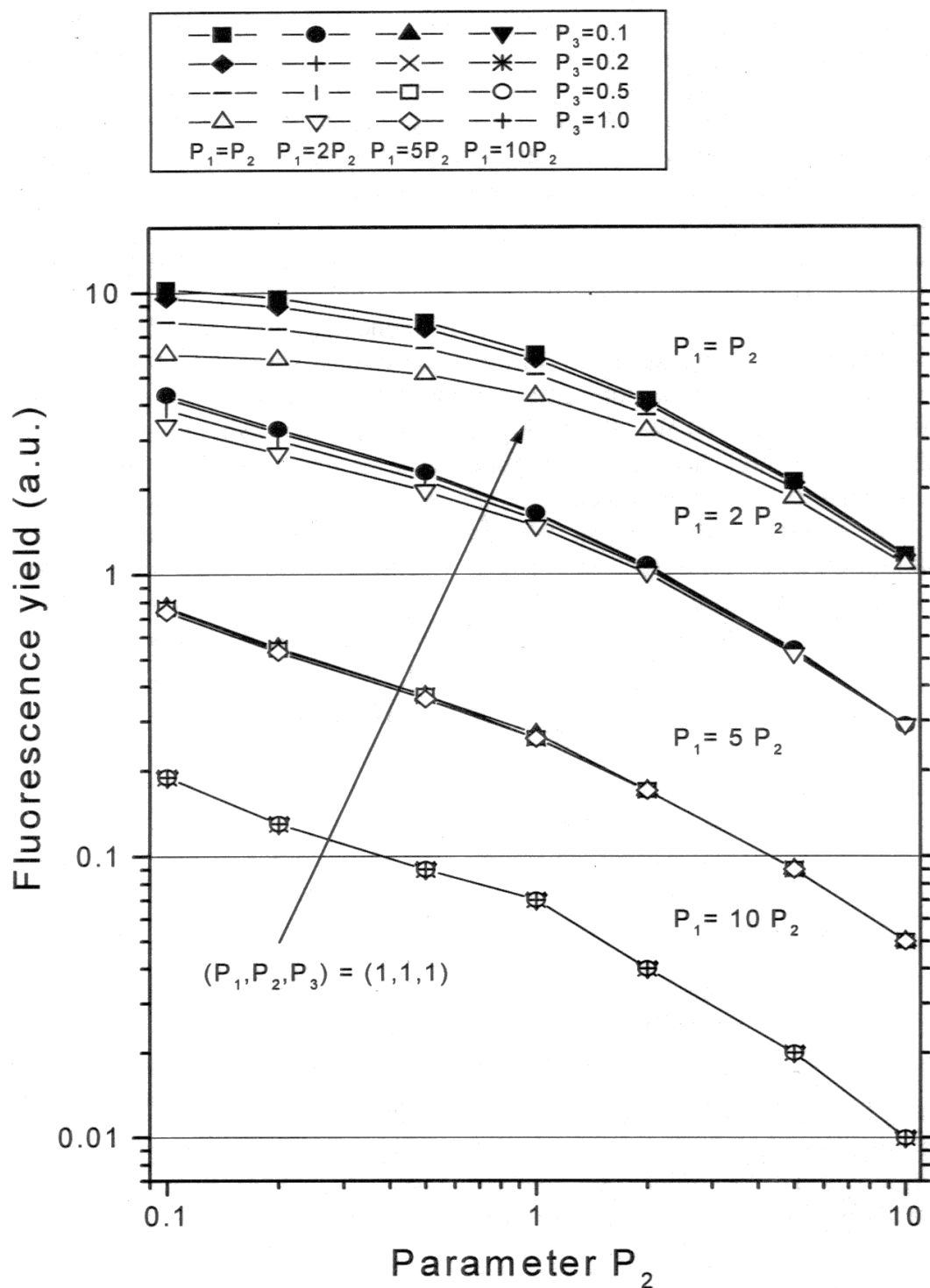


Figure 1.4 *Time-integrated LIF yield as predicted by the model*

Clearly, P_1 relating the excited state bath interaction rate to the pump rate determines the LIF yield to a large extent irrespective of the value of P_3 . This seems to suggest a limited influence of RET processes in the excited state on the resulting LIF signal. As expected,

the largest signals are obtained for lower values of P_1 and P_2 (i.e., in the high laser power regime). Finally, it should be noted that in both laser power regimes the LIF signal remains linearly dependent on the molecular number density in the probed ground state (i.e., N_2^{eq}) giving reason to the development of proper calibration procedures.

1.3.3 Imaging

Essentially, LIF is an incoherent detection technique and the fluorescing molecules emit their fluorescence in all directions on a nanosecond timescale. Typical laser pulses last up to 20 ns whereas the fluorescence lifetimes of the A and the D state of NO are about 250 ns [43] and 18 ns [52], respectively. Consequently, the LIF signal can be observed by means of time-gated detection. In addition, in imaging studies of minority species the highly sensitive LIF technique can only be fully explored by means of adequately operating image intensifiers. Both requirements are generally met in combination, i.e., a timing device only activates the image intensifier during the selected detection time therewith eliminating the need for unrealistically fast mechanical shutter systems. Nowadays, a wide variety of computer-based ICCD (Intensified Charge Coupled Device) imaging systems with gating times as short as 5 ns is commercially available.

The typical setup of an image intensifier consists of a photocathode, one or more Multi-Channel Plates (MCP) and a phosphor screen. The photocathode converts incident photons into photo-electrons with a given efficiency (about 8-10% on average in the UV range). These photo-electrons are amplified up to 10^6 times in the MCP and finally, the phosphor screen converts the photo-electrons back into photons again. The image intensifier is gateable by reversing the potential between the photocathode and the MCP. Typical phosphorescence lifetimes are in the order of 25 ms and, thus, the short-lived (UV) fluorescence is converted into relatively long-lived (green) phosphorescence. The image on the phosphor screen may be focused onto the photo-sensitive CCD array by means of a lens. However, since this may also introduce disturbing optical aberrations, the phosphor screen image alternatively may be directly mapped onto the CCD array by a so-called fiber-optic taper typically consisting of more than 10^5 individual fibers.

Video rate ICCDs only use half of the photo-sensitive array for image acquisition while the other half is permanently masked and serves as a buffer area for a copy of the image acquired at the exposed half of the array. The frame transfer from the exposed area to the buffer area typically takes a few milliseconds and this buffer area is continuously digitized to produce the 50 Hz (Europe) or 60 Hz (US) analogue video signal. As a consequence, most free-running video rate ICCDs have no provisions for external triggering, i.e., cannot be made to respond to a given event. In steady combustion research this continuous feature does not pose a problem, obviously, since the video rate ICCD can be made to trigger the experiment. However, in the study of unsteady combustion any given event will randomly coincide with a particular frame of the 50 Hz video signal and this may lead to considerable signal losses. On the other hand, the video output may conveniently be recorded on video tape for later processing and in this way large amounts of visual data may easily be averaged off-line which, in turn, improves the reliability of a given qualitative result of the imaging experiment.

ICCDs not operating in video mode are commonly referred to as Slow Scan ICCDs. With proper triggering the frame output rate may now be synchronized to the events of

interest. By digitizing the image only every given number of events direct averaging on the CCD array is possible with minimum signal losses. The lower frame output rate of these ICCDs provides a longer readout time and this, in turn, allows for the digitization of the images in a larger dynamic range and with lower readout noise when compared with video rate ICCDs. Acquired images are usually stored to hard disk for later evaluation.

Fluorescence is emitted as a result of molecular transitions from a given rovibrational level in the electronically-excited state to many other different rovibrational levels of the electronic ground state of the molecule under investigation. As a consequence, selective spectral filtering of the fluorescence often provides a way to get rid of the laser radiation itself as well as interfering emissions from other molecules. Usually, the spectrally filtered LIF signal is monitored in a direction perpendicular to the plane of the laser light-sheet and a quartz objective in front of the ICCD permits the sharp focusing of the filtered (UV) fluorescence image onto the photocathode of the image intensifier. Often, CCD arrays are thermo-electrically cooled as to further reduce the already relatively low electronic noise levels. In the course of the research of this work both video rate and Slow Scan ICCDs were employed for the imaging.

1.4 Outline

Following the general introduction of this chapter, in chapter 2 the principal components of the regular experimental setup are described in greater detail with respect to the concise descriptions given in the experimental sections of the other chapters. The results of the first NO 2D-LIF measurements in the idling engine are reported in chapter 3. Two NO excitation scans recorded at atmospheric in-cylinder pressure clearly demonstrate the feasibility of non-intrusive spectroscopic measurements in a steadily running diesel engine. However, the initial in-cylinder NO fluorescence distributions as presented in chapter 3 also show the effects of window fouling by almost inevitable soot deposits on the windows. This window fouling problem is effectively tackled in chapter 4 where image-processing procedures are introduced allowing correction of the fluorescence distributions for window fouling as well as for in-cylinder laser extinction. Of course, the underlying assumptions were extensively tested and the results of these tests are also reported in this chapter. The NO distributions presented in chapter 5 have been submitted to the post-processing outlined in chapter 4 and, in addition, the overall 2D-LIF signal strengths contained in these images are corrected for collisional quenching, Boltzmann fraction, number density and in-cylinder laser intensity losses outside the imaged area. Due to the lack of data on D-state NO molecules in the correction for collisional quenching the effective thermally-averaged collision cross section necessarily is treated as a constant, however, a first attempt to determine this effective cross section is described in the last chapter of this thesis. Included in chapter 5 are two more NO excitation scans recorded from the loaded engine at in-cylinder pressures of 0.1 and 0.5 MPa. Finally, chapter 6 describes the assessment of the effective thermally-averaged collisional cross section of N₂ and air (80% N₂, 20% O₂) on the basis of calibration measurements in a high-pressure high-temperature cell.

Chapter 2

Relevant Experimental Topics

This chapter focuses on those features of the principal components of the regular experimental setup that are not or only side-ways discussed elsewhere in this work. The configuration of these key components is schematically depicted in figure 2.1. Some of the experimental details described in the next sections have turned out to be crucial for the success of the experiments reported in subsequent chapters.

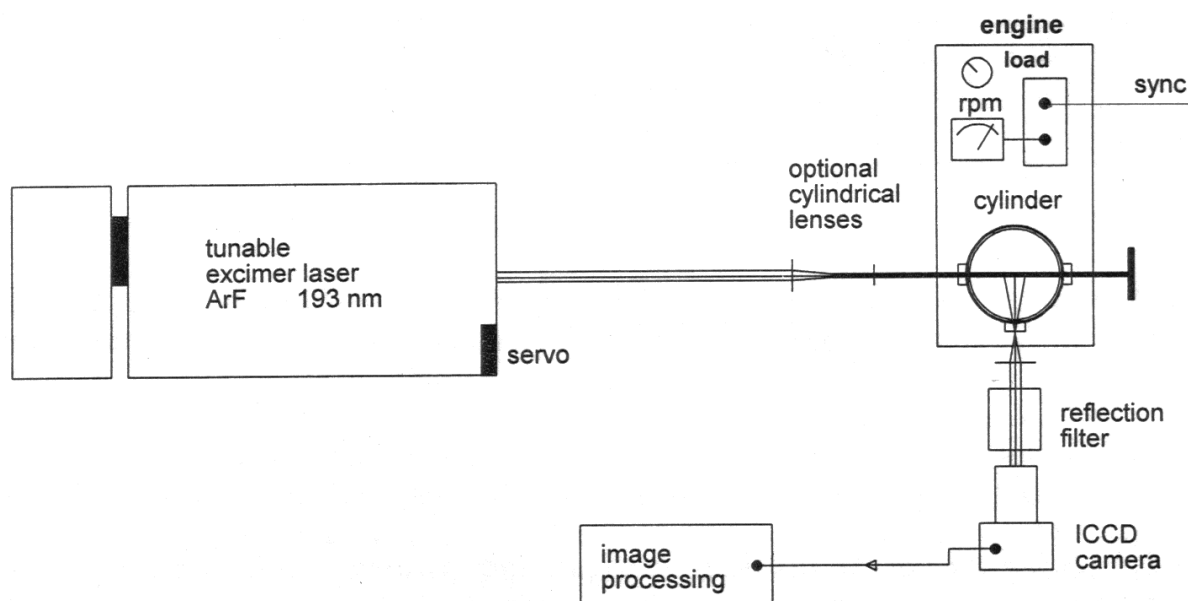


Figure 2.1 Schematic of the regular imaging setup. The laser output beam is made to traverse the interior top section of the cylinder and the fluorescence is monitored in a perpendicular direction by the ICCD camera. The reflection filter in front of the camera and the lens by means of which the fluorescence is coupled out from the cylinder are indicated as well. The laser frequency calibration section is not shown

2.1 The ArF excimer laser

The tunable ArF excimer laser producing radiation around 193 nm actually consists of two discharge cavities of which one is equipped with adjustable resonator optics (the oscillator) whereas the use of resonator optics in the other cavity (the amplifier) is optional. As both laser configurations are used in this work, they are schematically depicted in figure 2.2. The oscillator resonator is set up by the partly reflective mirror M1 and the grating G. Two prisms expand the oscillator beam as to fully utilize the grating area. The angle of incidence on the grating may be varied by tilting the grating with a millimetre screw. The two mirrors M2 and M3 direct the oscillator beam through

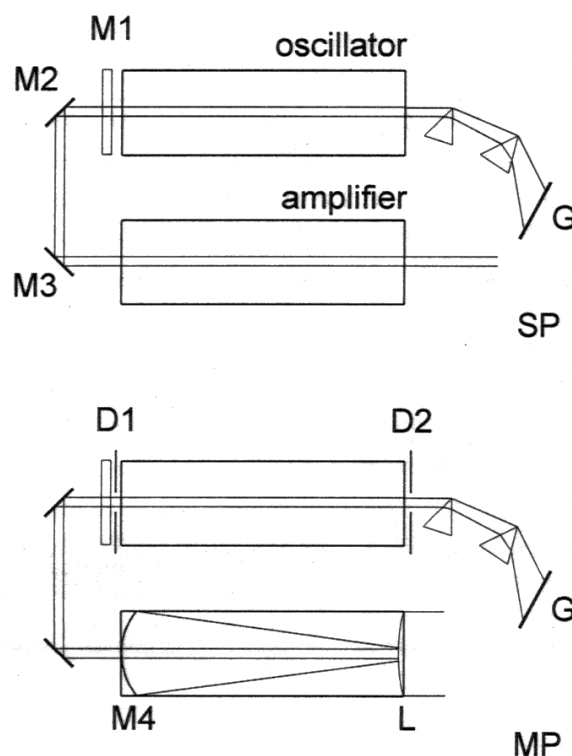


Figure 2.2 Schematics of the two laser configurations as used in this work. For clarity, in the bottom MP configuration the amplifier cavity is drawn in side-view showing the expansion of the narrow vertically oriented laser beam more explicitly

the amplifier cavity either in a Single Pass (SP) mode (without amplifier optics; upper configuration in the figure) or in a Multiple Pass (MP) mode (with the unstable resonator optics L and M4 mounted; bottom configuration). By means of the two diaphragms D1 and D2 the central part of the oscillator beam is injected to the amplifier cavity through a small hole at the centre of the fully reflective concave mirror M4. At the end of the amplifier cavity the oscillator beam is reflected by the central part of a quartz plano-convex lens L and since this lens is positioned in the focus of M4, the laser output beam is made parallel again. Compared with the former (SP) mode, this latter (MP) mode provides about twice as much pulse energy some of which, however, in the form of broadband (≈ 1 nm) background radiation.

In figure 2.3 a typical NO D–X excitation scan measured in an oxy-acetylene flame with MP mode laser operation is shown. This spectrum clearly reveals the amplifier-induced fluorescence at the ends of the about 225 cm^{-1} wide oscillator tuning range. On the evidence of a similar excitation scan recorded with the (same) laser operating in SP mode, as presented by Versluis *et al.* [44], these wings are completely eliminated by the removal of the unstable resonator optics. For this reason, the first imaging experiments as reported in the next chapter of this work were performed with the SP configuration of the laser. However, in these experiments the laser output power from

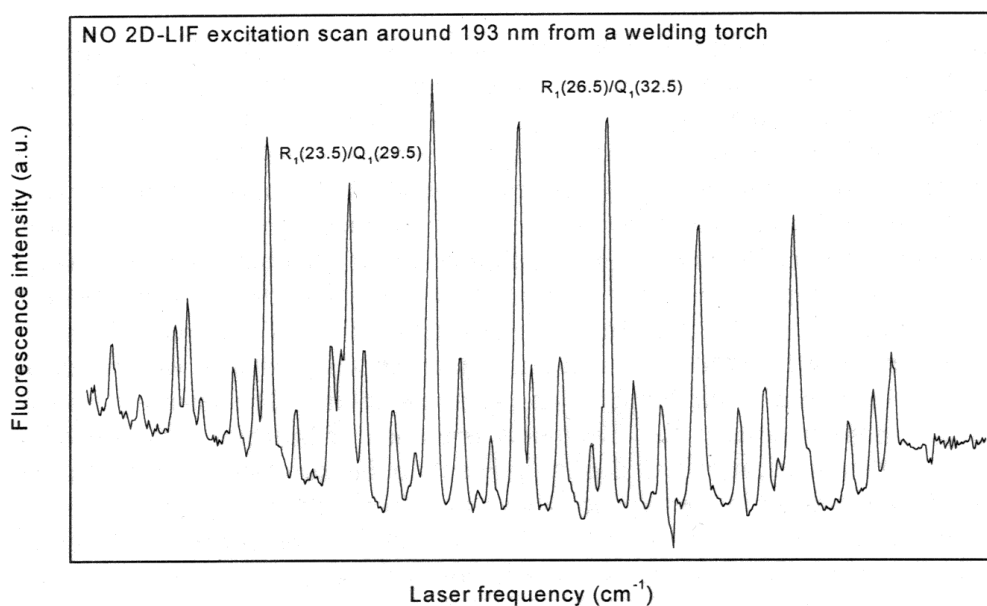


Figure 2.3 An arbitrarily chosen NO excitation scan from the flame of a welding torch demonstrating the broad band radiation-induced wings on either side of the laser tuning range

SP mode operation was observed to be only about 40% of the output power generated by the MP configuration. In view of the in-cylinder extinction displayed by the first fluorescence distributions the laser was used at maximum output power (MP mode) in all other experiments. It should be noted that the resonances selected for imaging are located near the centre of the laser tuning range where the broad band radiation-induced fluorescence resulting from MP mode operation is the least disturbing.

The use of unstable resonator optics leads to an inhomogeneous distribution of the laser intensity over the cross sectional area of the laser beam as a consequence of the hole in the centre of M4. However, by introducing a very small misalignment of M3, the (darker) hole in M4 may be projected just outside the beam cross section when viewed at the position of L. This considerably improves the homogeneity of the intensity distribution at the larger more practical distances from the laser output window.

2.2 The engine

Except for its single cast iron cylinder the 4-stroke diesel engine (HATZ-Samofa) was intentionally left in its original state as produced in the mid-fifties by a joint-venture of Dutch engine manufacturers. Because the engine was built for a long operating life without much ado the design is very straight-forward. The combustion chamber in the cylinder head may be pre-heated by a fuse. After a while the engine can be started by means of a starting crank and once running speed control is provided by a lever mounted on the crank case. Finally, the one other lever of the engine controls the valve action in the cylinder head therewith serving as a (safety) break. Of course, a minor adjustment regarding the start procedure of the engine had to be made. The rather primitive starting

crank was replaced by an electric motor driving the flywheel of the engine by means of a belt and the required pre-heating of the combustion chamber is now easily achieved by engaging the valves of the motored engine. After a while by simply pulling the speed control lever (i.e., by engaging the fuel pump) the engine is started.

By means of a ram tappet the movements of the fuel pump plunger are controlled by the fuel cam of the cam shaft and fine adjustments with respect to the injection timing (as to accommodate the combustion of different fuels) can be made by changing the effective length of the tappet. In a similar way the valve timing may easily be fine adjusted to optimum engine performance. The lubrication of all internal parts of the engine is accomplished by the movements of the crank shaft balance weights through the lubricating oil contained in the bottom part of the crank case. The resulting mist of ultra-fine lubricant droplets ensures the frictionless operation of bearings throughout the crank case. In fact, this lubrication method turned out to be so effective that traces of the lubricant oil even end up in the cylinder above the piston, passing a series of piston rings on its way up. Unfortunately, for a number of reasons, the presence of lubricant oil droplets in the measuring volume poses a serious problem in the present study of in-cylinder NO distributions. The main reason is that conventional lubricants strongly absorb UV radiation. Another problem is posed by the participation of lubricant oil in the combustion, since this may affect the observed NO distributions to an unknown extent. Finally, conventional lubricant oil and oxygen form an explosive combination when not handled carefully and in view of the oxygen-enriched combustion studied in this work, the uncontrolled presence of any additional explosive mixtures may be very disturbing.

The solution was found in the application of a perfluorinated polyether lubricating fluid (Fomblin Y-25, Montedison) as commonly used in mechanical pumps handling reactive gases. This agent is transparent for the 193 nm laser radiation in both liquid and vapour phase as well as non-flammable over a wide temperature range. In addition, its large molecular weight (3000 on average) helps to some extent to keep the lubricant in the crank case below the piston. However, in the contact of the piston rings with the cylinder bush the fluid shows poor lubricity in this rather unusual application. The resulting in-cylinder pressure reduction made the renewal of piston rings necessary after about every 20 hours of engine operation.

The in-cylinder top region was made optically accessible by mounting three 2.5 cm thick cylindrical quartz (Suprasil-I) windows in stainless steel holders in the cylinder wall as close to the cylinder head as possible. In order to make room for those holders some parts of the cooling ribs had to be removed first, whereafter the openings for the insertion of the holders were made in the cylinder wall. The body of each holder is secured in its position by means of two studs in the cylinder body as schematically depicted in figure 2.4. In combination with a groove in the latter a Viton ring provides an easy to handle and very effective pressure lock capable of surviving the high temperatures and the numerous mounts and dismounts of the holders that come with this study. The windows were made to precisely fit the holder bodies with sufficient support from all sides. Obviously, at the inner side the least support is needed and by slightly reducing the window diameter at this side the window is kept in position by a small support edge of the holder, thus leaving 2.5 cm as the effective diameter of the optical access channels. Between this support edge and the window at lower operating temperatures a teflon washer provides another flexible pressure lock, however, at higher temperatures hollow copper rings are used instead. The much stronger outward forces are compensated by

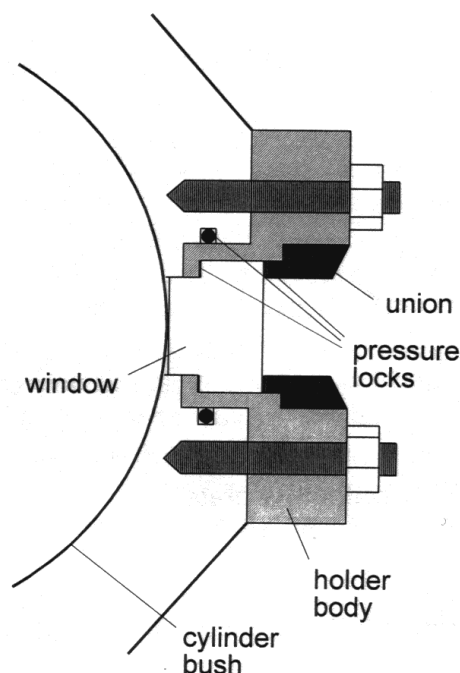


Figure 2.4 *Cross-sectional view of an optical port*

means of a union screwed in the holder body from the outside. Finally, the last pressure lock is formed by a paper washer between the window and the union.

As a consequence of the gaps between the flat inner surfaces of the windows and the curvature of the cylinder bush, however, the compression ratio easily becomes critical. In particular, the performance of the top piston ring turned out to be crucial for proper engine operation. Although it initially took some effort (and quartz) to find the right combination of materials involved, nevertheless, over the years the configuration as described here has proven its reliability.

2.3 The reflection filter

Two parallel pairs of dielectrically coated substrate plates are mounted on a pair of mechanically coupled discs as shown in figure 2.5. At each reflective surface the angle of incidence determines the wavelength of the reflected radiation and by rotating any one disc all angles involved are automatically adjusted. In the 45° position as drawn in the figure the manufacturer (Laser Optik, Garbsen, Germany) claims a peak transmission of 85% at 193 nm (i.e., the ArF excimer laser wavelength) with a bandwidth of about 10 nm (FWHM). However, by adjusting the angles of incidence the narrow filter bandwidth remains practically unaltered and as a result of the about 30 nm wide tuning range the reflection filter (occasionally also referred to as interference filter) can also be made to effectively suppress the scattered laser radiation. As a matter of fact, in calibration experiments preceding the insertion of the filter in the detection path at about 12° incidence a maximum transmission of 80% at the selected NO fluorescence wavelength of

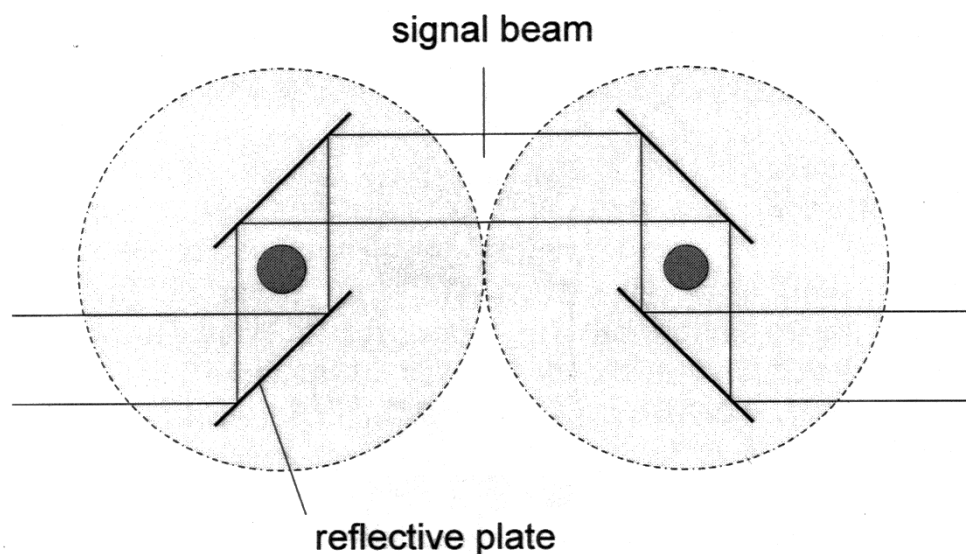


Figure 2.5 Schematic of the reflection filter setup in the case of 45° incidence

208 nm was observed. At this angle of incidence the 193 nm laser radiation turned out to be totally rejected as falling well outside the 201-220 nm wavelength region where the transmissions were found to be larger than 1%. In this configuration the filter bandwidth comes down to about 13 nm (FWHM) and the consequences for the imaging experiments reported in this thesis with respect to interfering fluorescence around 208 nm from molecular species other than NO are extensively discussed in subsequent chapters. In this respect, it should be noted that up to now the specifications of this filter configuration are beyond competition and that, consequently, the cascading of two filters (i.e., by using 8 reflective plates) leading to an even narrower bandwidth at the expense of only about 16% (peak) transmission deserves to be considered in future NO imaging studies as well.

2.4 Imaging setup

In the first experiments the video rate ICCD output was directly recorded on tape and off-line analysis was performed by means of a so-called frame grabber card (Matrox PIP-1024) installed in a 386SX personal computer. The heart of the video rate ICCD (Theta Electronic Systems) is a photo-sensitive CCD array of 395×295 $80 \mu\text{m}$ wide and $60 \mu\text{m}$ high pixels. The frame grabber transforms the acquired images to an array of 512×512 pixels allowing for the on-line visualization of the 8-bits monochrome images in several different false colour representations on a separate RGB monitor. Besides these false colour representations and frame grabber control the home-made imaging software also provides some basic numerical evaluation procedures for the frame grabber output images. For instance, by only considering the sum of pixel values contained in a selected part of the captured frames (while the laser frequency is scanned) excitation spectra may be evaluated off-line. Alternatively, by using the computer's memory the average of any given number of frames may be evaluated as well. The results of these evaluations are usually stored on the computer's hard disk for further processing. Note that this video rate

imaging system is discussed in the previous chapter also and that a more detailed description (including the imaging software) is given by Versluis in [53].

Later experiments are performed by means of a thermo-electrically cooled Slow Scan ICCD (Princeton Instruments, ICCD-576/RB-E) containing a photo-sensitive array of 576 x 384 22 μm square pixels. The accompanying software installed on a Pentium processor based personal computer provides easy on-screen control of the relevant imaging parameters (e.g. exposure time, trigger delay, dynamical resolution, number of images to average etc.) whereas most hardware settings may be directly adjusted by additional controls as well. In order to accommodate the further processing the 12-bits images of interest may be written to the computer's hard disk in a variety of (compressed or uncompressed) file formats. For completeness, it should be mentioned that in some of the experiments reported in chapter 4 of this thesis another very similar Slow Scan ICCD imaging system (FlameStar, LaVision) was involved. Finally, considering the huge technological progress on the field of scientific imaging techniques over the years of this research alone, future imaging systems reasonably may be expected to be much faster and capable of handling ever larger amounts of digital information. In view of this and in respect to the research of this work, the developments of new camera techniques may be expected to include the possibility of supplementing each recorded image (fluorescence distribution) with data on its spectral content (vital to the identification of the molecular source(s) at higher pressures) within only a few years from now.

Chapter 3

Laser-Induced Fluorescence Imaging of NO in a n-Heptane- and Diesel-Fuel-Driven Diesel Engine²

Abstract

Continuous on-line imaging by 2D-LIF techniques of in-cylinder NO distributions in a steadily running diesel engine is explored using an ArF excimer laser at 193 nm in low power mode. For the first time NO excitation spectra could be measured as a result of high optical transparencies during measurements over longer periods of time. The averaged distributions show different combustion behaviour of both fuels proving the potential of the 2D-LIF technique in application to non-intrusive steady state combustion diagnostics in a running diesel engine.

3.1 Introduction

The study of the combustion process inside the combustion chamber of a diesel engine is of utmost importance for the reduction of toxic emission components like NO and soot particles. Although modelling of the combustion process continues to progress, we are still far from a profound understanding of the physics and chemistry inside the engine. At the moment the design of diesel engines is still mainly based on empirically obtained knowledge. In view of the complexity of the diesel fuel combustion process, any information about where and when NO or soot is produced, is extremely valuable. This information can, in principle, be obtained by using non-intrusive diagnostic laser techniques.

During the last decade the Laser-Induced Fluorescence (LIF) method has proven its powerful value as a sensitive and molecule selective detection technique in application to both stationary as well as turbulent combustion processes, as indicated by numerous publications on this topic. The LIF method has been applied successfully to spark ignition car engines [6] and recently also to the observation of molecular distributions inside a running diesel engine. Arnold *et al.* [7] were the first to demonstrate that two-dimensional distributions of NO and OH can be recorded by LIF using a tunable excimer laser at 193 and 248 nm, respectively. Recently also Alatas *et al.* [8] have visualised the NO distribution by LIF applying a frequency-doubled tunable dye laser at 226 nm. They concluded that the NO formation starts early during combustion and stops no later than 30 to 40 degrees ATDC (After Top Dead Centre).

In both investigations a diesel engine was used running on a substitute fuel, n-heptane [7] or a 50/50 mixture of iso-octane and tetradecane [8] (chosen for its combustion properties resembling those of real diesel fuel). The main reason for not using diesel fuel is the presence of numerous absorbing and fluorescing components causing a low

² This chapter is based on the following publication: Th.M. Brugman, R. Klein-Douwel, G. Huigen, E. van Walwijk, J.J. ter Meulen, Appl. Phys. B **57**, 405-410 (1993)

transmission of the laser beam and a strong combustion background radiation in a large wavelength region. Another very serious problem in the case of diesel fuel is the high soot production causing a blackening of the windows and reflection of the laser light by the soot particles. However, the soot problem is not eliminated by combusting substitute fuels. In the two experiments mentioned above, the windows could be kept clean for one or two minutes. This is too short to record excitation spectra to characterize the measured species. Furthermore, any study of the NO distributions as a function of selectable combustion conditions (e.g. engine load, rotational speed and operating temperature) will be difficult since the engine has to be stopped and opened after each measurement in order to clean the windows. Restarting the engine almost certainly leads to slightly different combustion conditions during the measurements since there will be too little time to reach steady equilibrium conditions.

The objective of the present investigation is the study of the possibility of LIF diagnostics on NO inside a diesel engine running on both n-heptane as well as diesel fuel. In contrast to the experiments of Arnold *et al.* and Alatas *et al.*, an indirectly injected diesel engine is used. The optical access also differs from the transparent engine set-up used by these authors. The results make clear that the LIF technique using a tunable excimer laser offers very promising perspectives for the observation of NO, even in the combustion of diesel fuel. Excitation spectra are obtained which undoubtedly belong to NO. The measurements are performed at specific crank angles as a function of engine load. As may be expected, the NO distributions in n-heptane and diesel fuel combustion show some clear differences. Essential for all these 2D-LIF measurements is the avoidance of window blackening, thereby extending the measurements to a nearly unlimited period of time.

3.2 Experimental

A schematic overview of the experimental setup is depicted in figure 3.1. The measurements are performed in a 4-stroke air-cooled single cylinder indirectly injected diesel engine (HATZ-Samofa) with a swept volume of 581 cc (bore 86 mm, stroke 100 mm). The internal timing is performed by unadjustable cams on the cam-shaft, leaving the amount of fuel supplied each full cycle as the only controllable variable of the engine. An adjustable water-cooled electric brake (Zollner & Co.) is mounted on the engine by means of a flexible shaft attached directly to the flywheel, thus providing the various load conditions. The engine is lubricated by a minimized amount of a UV-transparent and chemically inert lubricant in order to prevent engine damage during the measurements. The synchronization of the laser pulses to the running engine is performed by an optoelectronic device which continuously monitors the rotation of the cam-shaft. This device triggers the delay generator (SRS DG 535) which synchronizes the laser and the detection system. The rotational resolution is about 0.6° and since in a 4-stroke engine the crank rotates at twice the speed of the cam-shaft, the error made in any selected crank angle is found to be 1.2° . The rotational speed of the crank is determined by an on-line display of the angular frequency. The influence of oxygen enriched combustion on the NO and soot formation, as reported by Alatas *et al.* [8] and others, is verified by means of an adjustable oxygen supply to the air-inlet of the engine.

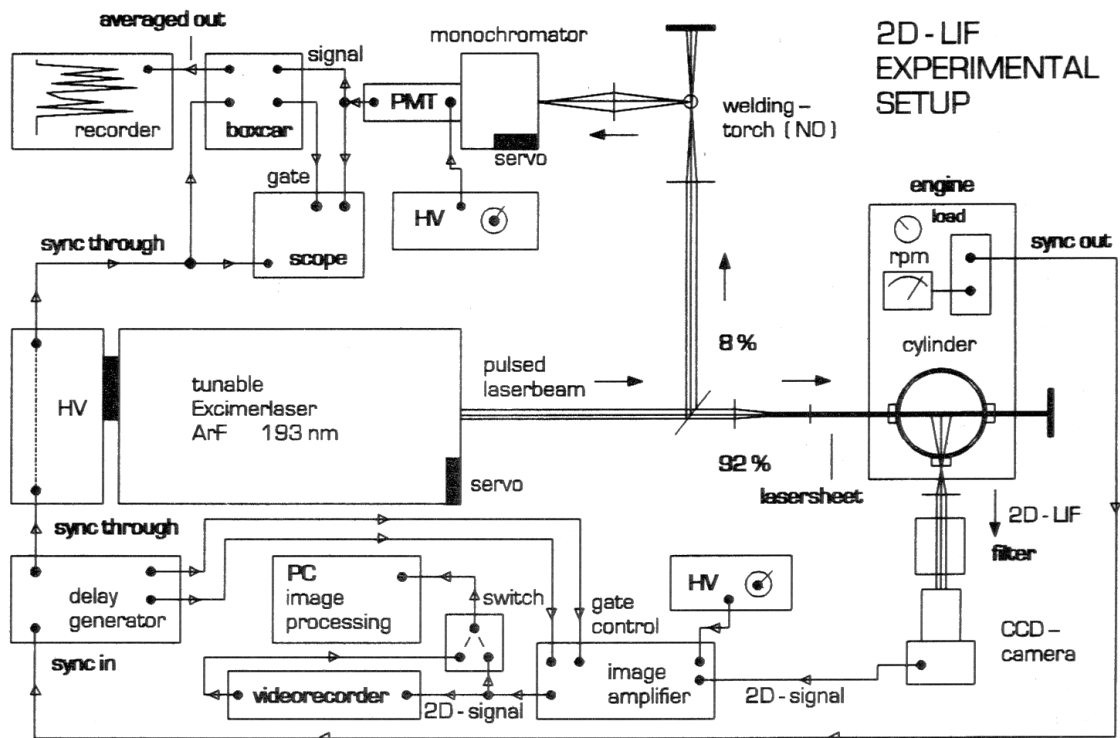


Figure 3.1 Schematic overview of the experimental setup. The image intensifier actually is integrated between the photocathode and the phosphor-screen in the ICCD camera

The interior of the cylinder is made optically accessible by mounting three cylindrical quartz windows in the cylinder wall as close to the cylinder head as possible. A sketch of the modified cylinder is depicted in figure 3.2. Due to the discrepancy of the flat inner surface of each window (diameter 25 mm) and the curvature of the cylinder wall, a part of the compressed fuel-air mixture will leak away during each compression stroke resulting in an effectively larger compression volume. Since this leakage is time-dependent, the actual compression ratio increases with the rotational speed of the crank. Based on a previous measurement of the characteristics of the modified engine running on diesel fuel at 240 rpm, the compression ratio is roughly derived to be about 1:9, assuming a simple adiabatic compression stroke. This is small in comparison with the standard values near 1:16 and most likely caused by the modifications providing the optical accessibility of the cylinder. Due to the movement of the piston the windows in the cylinder wall are optically blocked for crank angles between 70° BTDC (Before Top Dead Centre) and 70° ATDC, thereby limiting the 2D-LIF measurements in the expansion stroke to crank angles greater than 70° ATDC after combustion. The maximum delivered power of the engine was measured using the adjustable brake to increase the load until the engine ceased running. In the case of n-heptane this turned out to be almost 1.8 kW, whereas in the case of diesel fuel this limit dropped to about 0.9 kW. In both cases the piston was overheated and got slightly stuck near BDC. The large difference in maximum power is already indicating the different combustion behaviours of both fuels. The highest measured power (1.8 kW using n-heptane) forms the reference value (100% load).

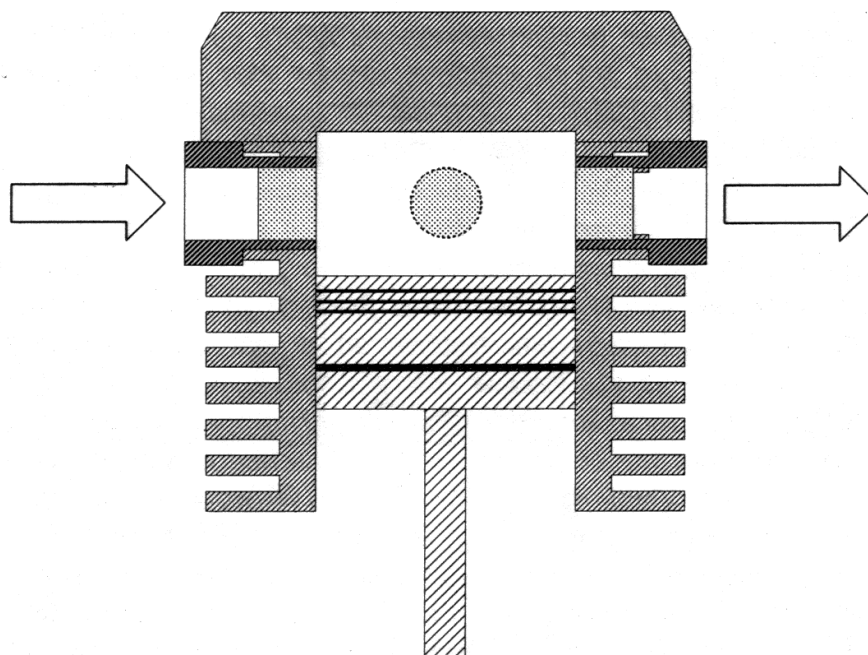


Figure 3.2 *The optical accessibility of the cylinder. The laser travels from left to right and the 2D-LIF signal is detected in the perpendicular direction. The cross section of the swirl chamber in the cylinder head is not drawn*

The tunable ArF excimer laser (Lambda Physik EMG 150 MSCT) depicted in fig. 3.1 actually consists of two laser tubes, one serving as a tunable oscillator and the other as an amplifier for the oscillator radiation. This amplifier may be used in either Single-Pass (SP) mode (typically 40 mJ/pulse) or Multiple-Pass (MP) mode, the latter mode resulting in more power (typically 100 mJ/pulse) at the expense of the spectral purity of the laser output [44]. To increase the S/N-ratio of the imaging in this work the amplifier is set to operate in SP mode delivering narrow-band tunable laser pulses with a spectral intensity of about 5.1 MW/cm^2 if tuned near the centre of the 300 cm^{-1} wide tuning range. The bandwidth of the laser is about 0.6 cm^{-1} (FWHM) as derived from measurements on NO in an oxy-acetylene flame used for on-line calibration of the laser frequency.

By means of two 45° mirrors the laser beam is vertically adjusted to the position of the windows in the cylinder wall. About 8% of the laser energy is directed into the calibration section of the setup, using a MgF_2 beamsplitter. Without the optional insertion of the two cylindrical lenses (depicted in fig. 3.1) the pulse energy measured at the entrance window of the engine is approximately 30 mJ. During operation the laser beam is attenuated by a factor of 2 due to a thin layer of soot on the entrance window and the resulting intensity inside the cylinder is about 1.9 MW/cm^2 on a 20 mm high and 3 mm wide rectangular cross section. Inserting the two lenses and keeping the cross section unaltered yields about 20 mJ/pulse at the entrance window and an operational in-cylinder intensity around 1.3 MW/cm^2 , which turns out to be too low to produce the same signal strength compared to the case in which the laser beam is not modified. Focusing the laser beam into thinner sheets leads to slightly stronger signals, which is an indication that the invoked transition is not saturated at these pulse energies.

Within the tuning range of the laser NO can be efficiently excited through many rotational channels of the vibronic transition: $D^2\Sigma^+(v'=0) \leftarrow X^2\Pi(v''=1)$. Due to collisional quenching, however, the slightly lower lying $C^2\Pi(v'=0)$ level will be populated as well and the resulting fluorescence consequently displays two distinguishable sequences: $D^2\Sigma^+(v'=0) \rightarrow X^2\Pi(v''=2,3,4,5,6)$ and $C^2\Pi(v'=0) \rightarrow X^2\Pi(v''=1,2,3,4,5,6)$, the strongest one originating from the primary excited level. The fluorescence resulting from the $D^2\Sigma^+(v'=0) \rightarrow X^2\Pi(v''=3)$ transition of NO at 208 nm is selected for performing the 2D-LIF measurements as well as for the on-line calibration. The 2D-LIF signal is slightly magnified by a spherical lens ($f=10$ cm) and subsequently transmitted through a band-pass interference filter consisting of four dielectric coated mirrors. The filter is adjusted to a maximum transmission of 80% at 208 nm with a bandwidth of 13 nm FWHM. This filtered 2D-LIF signal (imaging an in-cylinder area with a diameter of about 2 cm) is then fed to a 50 ns gated image intensifier and either directly processed or recorded on videotape for later processing. The calibration is achieved by measuring the time averaged intensity of the LIF signal (gate 100 ns) resulting from the same transition of NO in an oxy-acetylene welding torch by means of a 25 cm focal-length monochromator (Jobin Yvon M25, 610 g/mm) set to 208 nm and a photomultiplier (EMI 9635 QB), using the calibration data produced by Versluis *et al.* [44].

The imaging software is written for use with a specific image processing board (Matrox PIP-1024 A/D converter) installed in a 80386 AT personal computer. This board has an 8 bits dynamical range (256 grey values) and produces pictures of 512x512 pixels on the screen of a separate RGB monitor (Sony Trinitron). The software provides the possibility of false colour representations using different selectable pixelvalue-to-colour conversions. In addition to all basic picture modifying functions provided by the software, this system is also capable of taking its input from a VHS video recorder. This turned out to be a very convenient option at the expense of a hardly noticeable decrease of the S/N-ratio and consequently all 2D-LIF measurements in this work are processed afterwards from videotape. Another relevant feature of the software is the option to add all pixel values within a selectable rectangle of continuously grabbed images, thereby calculating the total intensity of each grabbed area. Each calculated value is plotted on the computer screen before the next picture is grabbed, creating an excitation spectrum if the laser is scanned simultaneously over its tuning range. All excitation spectra presented in this work are produced using this procedure and the recording time for each of the two excitation spectra obtained from the running engine was about 15 minutes. In a similar way the software is capable of adding any number of grabbed images and dividing the obtained array of total pixel values by the number of grabbed images to produce an averaged picture. A sophisticated re-scaling by fractional factors of this array to the full dynamical range is another option of the software which was used to obtain the averaged NO distributions under varying combustion conditions at specific crank angles. In this case the laser is tuned to a specific resonance and all other variables are kept constant during at least 2 minutes for each presented averaged NO distribution.

3.3 Results and discussion

All 2D-LIF measurements were performed for oxygen enriched combustion. The calibration signal was recorded on a strip-chart recorder while the 2D-LIF signals were

simultaneously recorded on video tape using the maximum gain of the image intensifier. The intake air was buffered to achieve a more efficient and continuous oxygen supply for all rotational speeds and as a result of this buffering precise oxygen volume fractions could not be determined. Volume fractions ranging from 10% to 15% seem reasonable estimates for most of the presented measurements.

For each fuel an excitation spectrum was recorded by scanning the laser frequency, whereafter several averaged NO distributions (at specific crank angles and specific loads) were measured at one of the strongest resonant rotational transitions. Data of Lee *et al.* [54] concerning interfering absorptions of the laser beam by molecular oxygen (around 193 nm), show that rather strong and temperature dependent absorptions may occur within the whole scanning range of the laser. These authors found, however, that one specific ro-vibronic transition of NO is undisturbed by absorption even at very high temperatures of the oxygen in the combustion. Although these strong absorptions were not observed in the engine this transition ($R_1(26.5)/Q_1(32.5)$ at 193.377 nm) [44] was selected to image the averaged NO distributions.

The measured 2D-LIF excitation spectra are compared to a significant part of the complete excitation spectrum as it is measured by Versluis *et al.* [44]. For a fair comparison, that particular part of the spectrum was re-measured in a welding torch, applying the same 2D-LIF technique as used for all measurements in this work. This spectrum is given in figure 3.3a where the relevant rotational transitions are indicated by bars on top of the spectrum. The strongest progression in all excitation spectra actually consists of two nearly coinciding sequences of transitions starting from different rotational levels in the ground state [44]. The R_1 progression departs from lower rotational levels, whereas the Q_1 transitions occur from higher rotational levels. Because of collisional quenching one must be careful in drawing conclusions from the intensity differences of the lines of this progression. The significantly lower intensity of the $R_1(27.5)/Q_1(33.5)$ transition, however, might be due to the stronger absorption by molecular oxygen at that wavelength [54].

The excitation spectra from the engine are presented in the figures 3.3b and 3.3c, using n-heptane and diesel fuel, respectively. Both spectra were recorded at BDC after combustion and as the exhaust valve is opened at that time, the pressure is expected to be slightly higher than atmospheric pressure. The engine delivered the same power (25% load) during these recordings resulting in different rotational speeds: 1000 rpm combusting n-heptane and 720 rpm running on diesel fuel. The S/N-ratio of both spectra is sufficiently high to characterize the recorded images as being produced by hot NO ($v''=1$). A comparison with the flame spectrum shows that the Q_2 progression originating from high rotational states is weaker, which must be the result of a lower temperature in the engine. Another difference between the flame and engine spectra is given by the linewidths. In particular for n-heptane broad lines are observed with a width of about 1.5 cm^{-1} . A possible explanation might be given by different contributions of the R_1 and Q_1 transitions to the lineshape. At the high flame temperature the Q_1 lines will be stronger than the R_1 transitions whereas at the lower engine temperatures both the R_1 and Q_1 transitions may give comparable contributions to the total line intensity. Since the frequencies of the R_1 and Q_1 transitions are slightly different (about 0.5 cm^{-1}) a line broadening may result. In contrast to the spectrum from the welding torch (fig. 3.3a) a small background signal is observed in the spectra from the engine. This is assumed to originate from fuel fragments radiating, either spontaneously or laser induced, within the

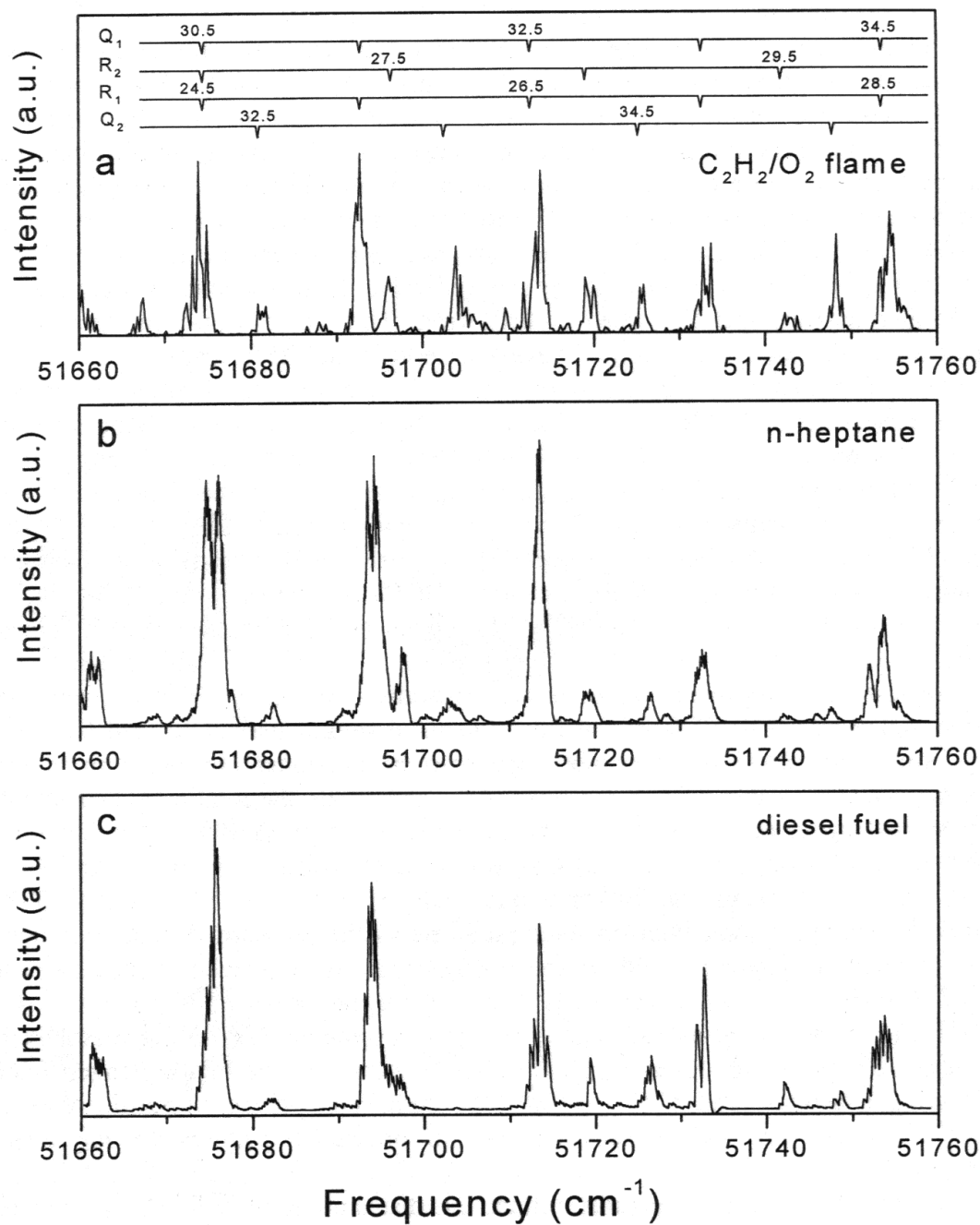


Figure 3.3a $D^2\Sigma^+(v'=0) - X^2\Pi(v''=1)$ excitation spectrum of NO, as obtained from an oxy-acetylene welding torch using 2D-LIF techniques. The rotational transitions are indicated by the horizontal bars on top of the spectrum

Figure 3.3b Excitation spectrum of NO, as obtained from the n-heptane driven diesel engine (1000 rpm, 25% load, BDC after combustion)

Figure 3.3c Excitation spectrum of NO in the case the engine is driven by diesel fuel (720 rpm, 25% load, BDC after combustion)

bandwidth of the 2D-LIF filter (201-214 nm).

Some of the measured two-dimensional NO distributions at specific crank angles as a function of the engine load are depicted in the figures 3.4.1, 3.4.2 and 3.4.3, respectively. The laser beam travels from left to right in all pictures and the same vertical plane in the cylinder is imaged by these measurements. All averaged distributions are obtained by grabbing more than 100 frames and re-scaling the result to the full dynamical range of the image processing system. The top row (a-c) in fig. 3.4.1 was measured at 120° ATDC, 135° ATDC and at BDC, respectively, using n-heptane and no load at 1300 rpm. The bottom row (d-f) of this figure resulted from measurements at the same crank angles, using n-heptane and 52% load at 1100 rpm. The top row (g-i) in fig. 3.4.2 also was measured at the same crank angles, using n-heptane and 25% load at 1200 rpm. The bottom row (j-l) displays the results at the same crank angles as all previous rows, but now using diesel fuel and 25% load at 700 rpm. The column at the left hand side in fig. 3.4.3 (m,p) shows arbitrary single snapshots at BDC after combustion, using n-heptane and 50% load at 1100 rpm. The column at the right hand side of this figure (o,r) depicts arbitrary single BDC snapshots as well, however, now using diesel fuel and 25% load at 700 rpm. Finally, the distributions shown in the central column (n,q) were measured in the exhaust stroke at 30° ABDC (n) and 60° ABDC (q), respectively, under the same circumstances as the bottom row of fig. 3.4.1, i.e., using n-heptane and 52% load at 1100 rpm.

The highest occurring pixel values in all snapshots is typically about 64, indicating a reasonable signal strength (25% of the full dynamical range) mainly limited by the laser intensity, since the transition does not appear to be saturated. In order to study the intensity dependence of the 2D-LIF signal on the crank angle the total averaged intensities of the unscaled signal are compared to the averaged intensity at BDC. For n-heptane at 52% load and 1100 rpm this yields: (d) 4%, (e) 20%, (f) 100%, (n) 240%, (q) 200% and for diesel fuel at 25% load and 700 rpm one finds: (j) 6%, (k) 13% and (l) 100%. In both cases the averaged total intensity increases fast as the pressure decreases which is a result of the higher quantum yield of the transition at lower pressures due to reduced collisional quenching. A similar pattern is displayed by the top rows of the figs. 3.4.1 (a-c) and 3.4.2 (g-i). The total averaged intensity as measured at BDC using diesel fuel and 25% load at 700 rpm turns out to be about twice as strong as the total averaged intensity at BDC using n-heptane and 52% load at 1100 rpm. Due to the re-scaling these total intensity differences are hardly reflected in the presented pictures of the averaged distributions.

In principle the measured pictures reflect the distribution of hot NO ($v''=1$) in the plane of the laser sheet. The exhaust valve in the cylinder head happens to be mounted at the side of the laser entrance window (left), while the inlet valve is mounted on the right. Moreover, the right hand side of the cylinder is more efficiently cooled because the cooling-fan is positioned there. This may explain the mostly stronger intensity observed at the left hand side of the pictures. However, the observed intensity distribution may be influenced by absorption of the laser beam along its path in the combustion chamber. If this were the case a stronger signal intensity from the left side of the viewed area should always be observed. Although most times the signal from the left hand side is the strongest indeed, this is not always the case as can be seen in the snapshots (m) and (o) as well as in the averaged distribution (l). So absorption along the length of the viewing area does not seem to play an important role and the observed inhomogeneous distributions are

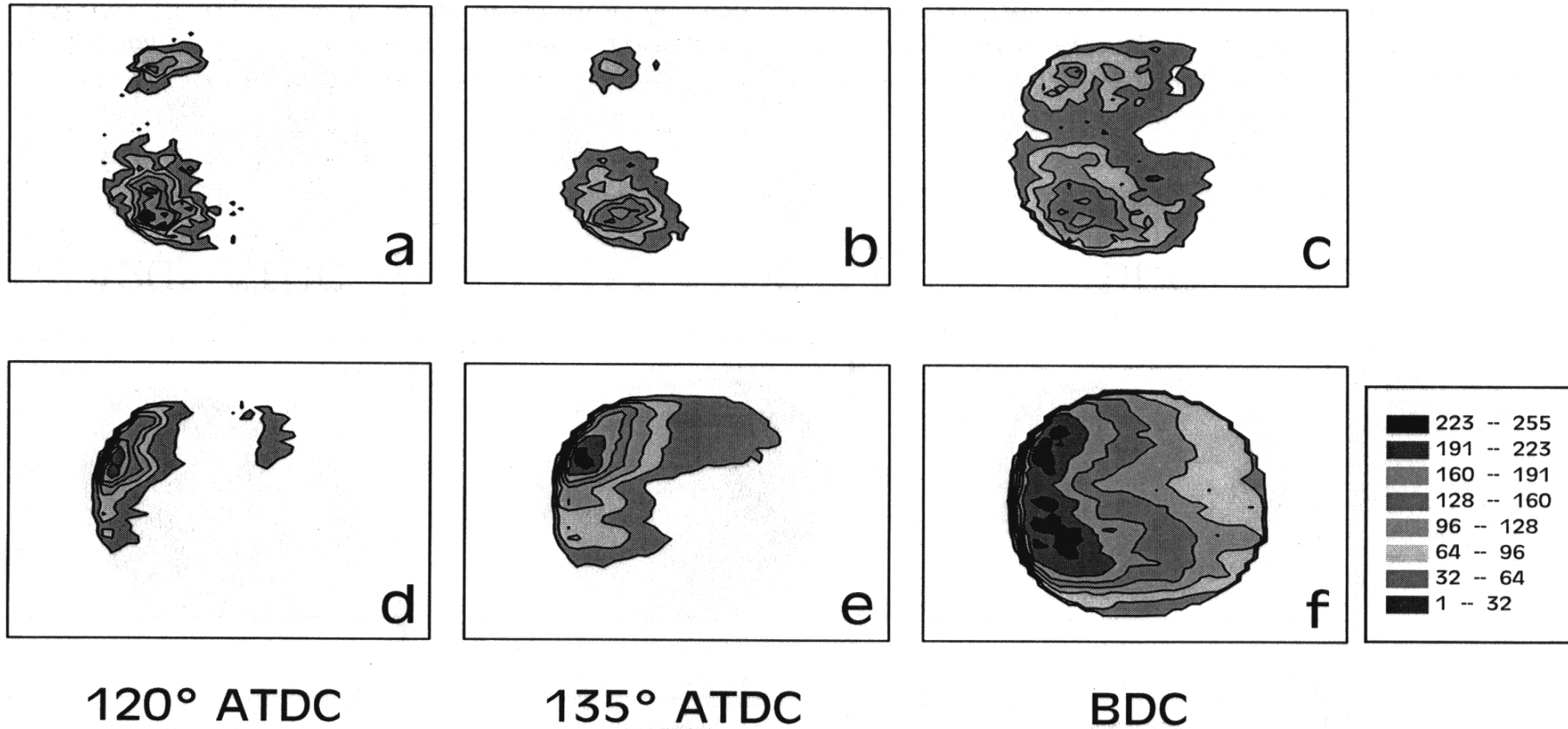


Figure 3.4.1 Averaged NO distributions measured as a function of crank angle and engine load using n-heptane. (a)-(c): distributions measured at 120° ATDC, 135° ATDC and at BDC after combustion, respectively, without load at 1300 rpm. (d)-(f): similar to (a)-(c) but with 52% load at 1100 rpm

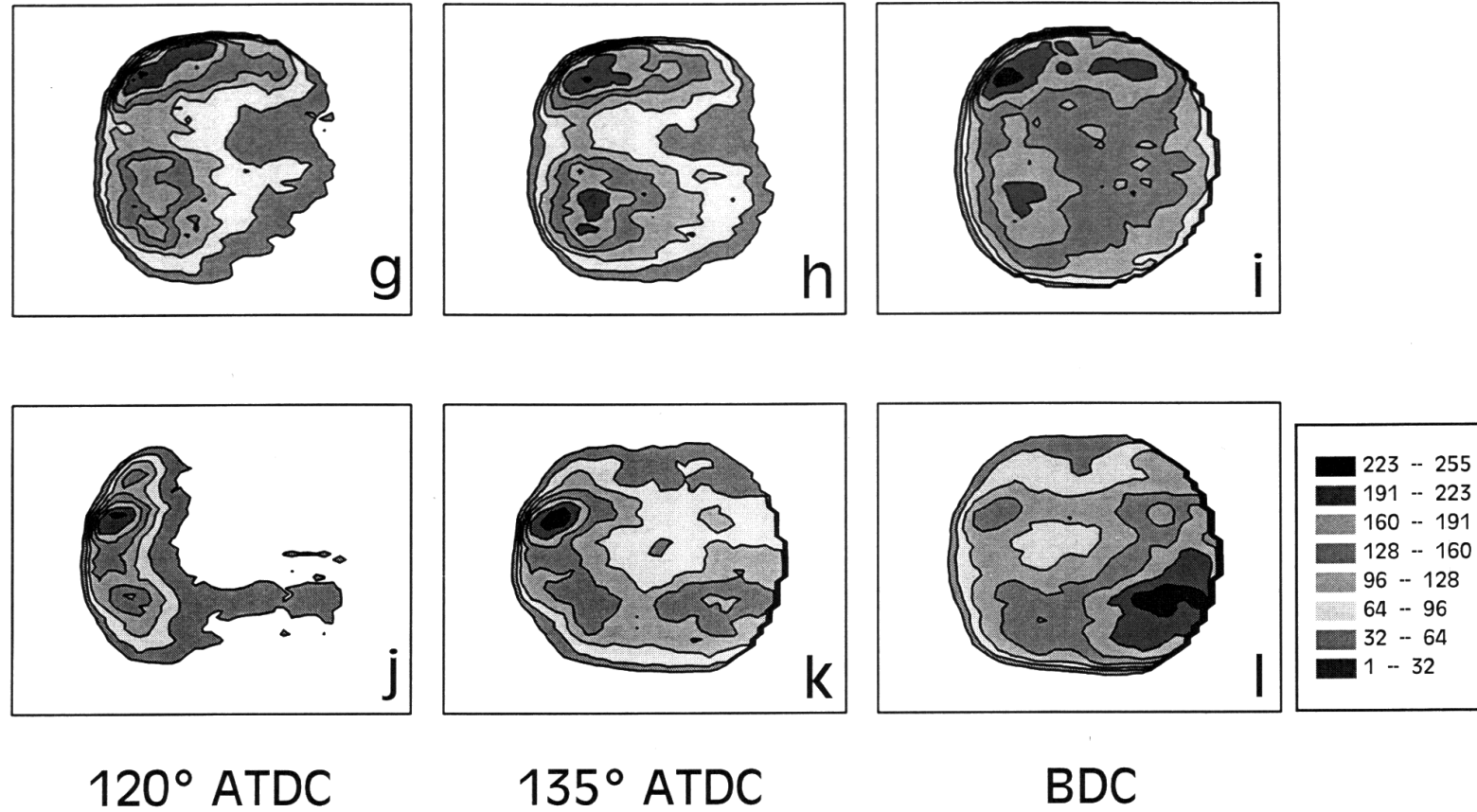


Figure 3.4.2 Averaged NO distributions measured as a function of crank angle and engine load using n-heptane and diesel fuel. (g)-(i): distributions in n-heptane combustion at 120° ATDC, 135° ATDC and at BDC after combustion, respectively, with 25% load at 1200 rpm. (j)-(l): similar to (g)-(i), using diesel fuel and 25% load at 700 rpm

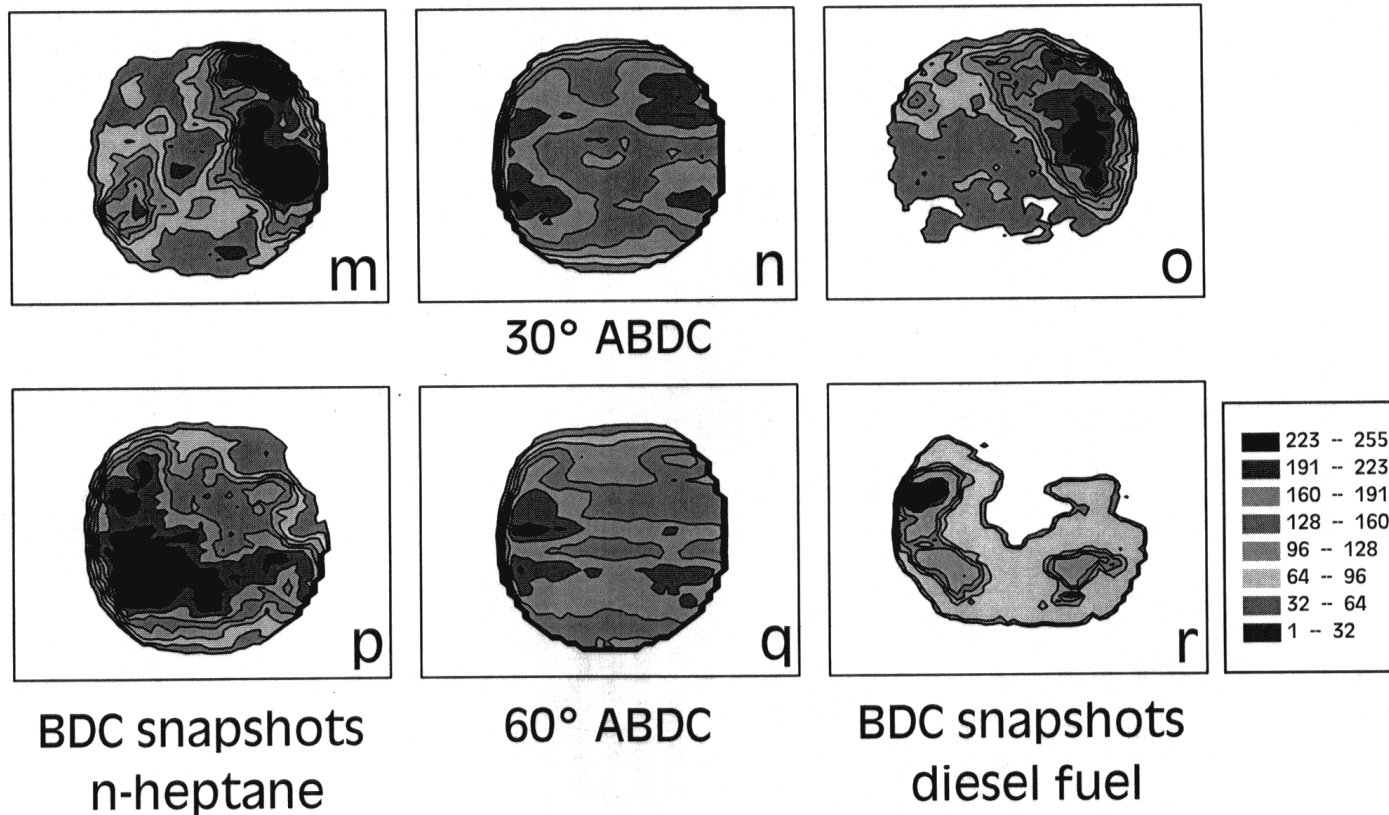


Figure 3.4.3 Averaged NO distributions and typical single snapshots measured as a function of crank angle, engine load and fuel. (m) and (p): single snapshots of the NO distribution at BDC in n-heptane combustion with 50% load at 1100 rpm. (n) and (q): averaged NO distributions in n-heptane combustion at 30° ABDC (n) and 60° ABDC (q) in the exhaust stroke, with 52% load at 1100 rpm. (o) and (r): single snapshots of the BDC NO distribution in diesel fuel combustion with 25% load at 700 rpm

most probably due to asymmetries in the NO distribution. In order to prove this argument the direction of the laser beam will be reversed in future experiments. In some pictures of averaged distributions, areas of lower total intensity (like g, h and i) are probably due to a non-homogeneous distribution of the pulse energy over the cross section of the laser sheet once the sheet has entered the cylinder. The different combustive behaviour of both fuels is reflected in the clearly different pictures of averaged NO distributions (f) and (l). In the case of diesel combustion (l) the NO distribution is more intense at the right hand side. Experiments are in progress to find the origin of this phenomenon.

3.4 Summary

The imaging of NO distributions in a running diesel engine by 2D-LIF measurements extended to longer periods of time offers the opportunity to investigate different steady state combustion processes as they result from selected fuels and operating conditions. In this work it is shown for the first time that NO produced in the combustion of diesel fuel can be observed. This is of great importance for future laser diagnostics in diesel engines as well as in other diesel combustion processes. The use of substitute fuels like n-heptane does not result in improved NO images, as was expected in view of increased absorption of laser radiation and emissions by many different components in the diesel fuel. The different combustive behaviour of n-heptane and diesel fuel in the same engine was observed in the total averaged intensities of the 2D-LIF signals as well as in the averaged spatial NO distributions at BDC.

The total observed 2D-LIF signal intensity appears to be limited mainly by the low laser power which was used to enhance the spectral purity of the measurements. Future experiments will be performed using increased laser power since the loss of spectral purity is balanced by much stronger 2D-LIF signals once the molecular source of the imaged radiation is identified. In addition, the load will be increased by modifying the engine, which will result in more realistic (i.e., larger) NO concentrations. This will allow the study of the NO formation in an earlier stage of the combustion process. In future experiments the tailpipe NO_x concentration will be measured as well in order to estimate the in-cylinder NO concentration resulting from selected steady operating conditions.

Chapter 4

Imaging and Post-Processing of Laser-Induced Fluorescence from NO in a Diesel Engine³

Abstract

The imaging of in-cylinder NO distributions in a steadily running optically accessible diesel engine operated on standard diesel fuel is performed by means of the 2D-LIF technique and a tunable ArF excimer laser at 193 nm. Simultaneous excitation at 226 nm showed that no sizable photo-chemical effects are induced by the excimer laser. In order to account for the gradually decreasing transparency of the windows due to soot deposits and for the in-cylinder attenuation of the laser intensity, signal processing procedures for the imaged distributions are presented. In addition to the more realistic depictions of NO distributions at selected crank angles and loads resulting from these procedures, the latter are an essential step towards a quantitative interpretation of the corresponding in-cylinder NO concentrations.

4.1 Introduction

Diesel engines are becoming increasingly popular because of their highly efficient combustion in comparison to spark ignited engines. This high efficiency generally leads to a lower emission of CO₂ and as a consequence diesel-fuel-driven engines tend to contribute less to the greenhouse-effect. The high temperature that results from the high pressure in the combustion chamber of a diesel engine causes the auto-ignition of the fuel/air mixture but also gives rise to the subsequent formation of NO and NO₂. Furthermore, the largest of the organic molecules making up the complex chemical composition of diesel fuel are easily transformed into carcinogenic coatings on the soot particles that are produced during the combustion as well. For environmental reasons the emissions of NO_x and soot must be reduced drastically in order to meet the ever more stringent emission standards. However, in spite of the progress made in the modelling of the physics and the chemistry in the combustion chamber [55] the diesel combustion process is still too complex to be fully understood. In recent years the applicability of several non-intrusive laser diagnostic techniques such as LIF (Laser-Induced Fluorescence) and Mie scattering to the study of the combustion processes inside diesel engines has been widely recognized. When the fuel is doped with fluorescing tracers, 2D-LIF can be successfully applied in the study of the fuel distribution in a spark-ignition engine [20] and in the combustion chamber of a directly injected diesel engine [17]. In-cylinder soot distributions may be studied by a combination of the 2D-LII (Laser-Induced Incandescence) technique and resonant (Mie) scattering [25]. In-cylinder NO distributions have been visualized by means of 2D-LIF by Arnold *et al.* [7], Alataş *et al.* [8] and

³ This chapter is based on the following publication: Th.M. Brugman, G.G.M. Stoffels, N. Dam, W.L. Meerts, J.J. ter Meulen, *Appl. Phys. B* **64**, 717-724 (1997)

Brugman *et al.* [9]. Alataş *et al.*, using a 50/50 mixture of iso-octane and tetradecane in a square combustion chamber, found evidence that the NO formation ceases at 30° to 40° ATDC (After Top Dead Centre). In these experiments it was assumed that the LIF detection method is non-intrusive. The high excimer laser intensities used, however, may give rise to photo-chemical processes by which NO is produced or destroyed. This might result in erroneously measured NO distributions. In this work a two-colour experiment was performed on NO in a running diesel engine in order to check for the occurrence of these photo-chemical effects.

In most of the above mentioned studies the test engines were driven by low-sooting substitute fuels and operated in skip-fired mode (i.e., the combustion in the motored engine takes place only every selectable number of cycles) in order to prolong the optical transparency of the windows of the combustion chamber. However, if the measurements are to be performed in a standard diesel-fuel-driven engine under steady operating conditions, the decreasing window transparency as a result of soot deposition should be taken into account. Also, the in-cylinder attenuation of the laser sheet intensity needs to be accounted for. The objective of this study was to investigate the extent to which the applied 2D-LIF in-cylinder imaging technique in itself is capable of producing reliable and accurate results. Therefore, methods are explored by which the imaged NO fluorescence distributions can be adjusted for the gradually decreasing transparency of the windows and the in-cylinder attenuation of the laser intensity, in order to obtain more realistic NO distributions. In addition, as a check of the reliability of the obtained NO LIF images, measurements were performed in which the laser beam direction was reversed. When corrected for window transmission losses and laser beam extinction, the obtained NO images should be independent of the laser beam direction.

4.2 Experimental

The laser, the engine and the intensified CCD camera are the principal elements of the experimental setup as depicted in figure 4.1. The tunable ArF excimer laser (Lambda Physik EMG 150 MSCT) delivers 193 nm radiation with an average pulse energy of 90 mJ in 13 ns over a rectangular cross-sectional area of 75 mm² (25 mm x 3 mm). Within the 300 cm⁻¹ wide tuning range of the laser, NO can effectively be excited through a series of rotational lines of the vibronic band D²Σ⁺(v'=0) ← X²Π(v''=1). In a previous publication on this topic [9] excitation scans of NO in the running engine are presented. Since in the same paper the experimental setup is described in detail as well, the following is focused on the essentials and some alterations.

4.2.1 The essentials

The 2D-LIF measurements are performed at a fixed laser wavelength (193.588 nm) corresponding to the coinciding R₁(23.5)/Q₁(29.5) rotational transitions of NO in the above-mentioned band. It turns out that slightly stronger signals are obtained on these lines in comparison to the R₁(26.5)/Q₁(32.5) transitions selected for imaging in [9]. Absorption of laser radiation by molecular oxygen in the Schumann-Runge band is not observed for either transition [9]. During the measurements the laser is manually kept on

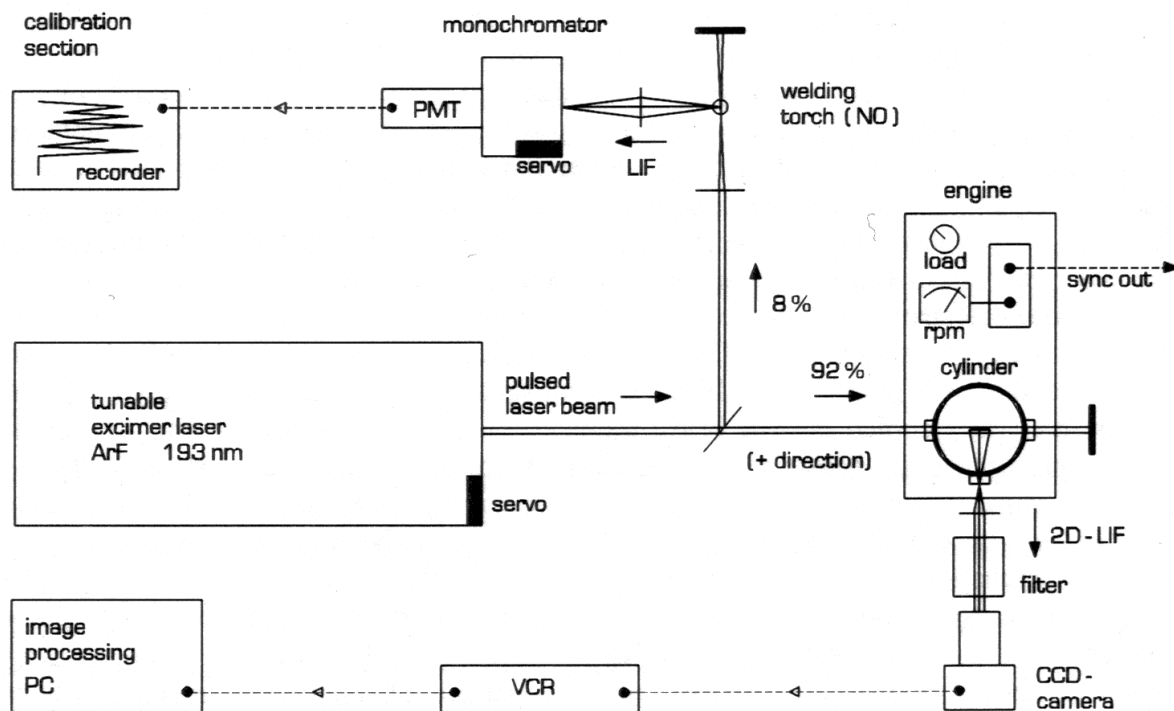


Figure 4.1 Schematic overview of the regular experimental setup

resonance by monitoring the simultaneously induced fluorescence from NO in an oxy-acetylene flame. In order to produce this calibration signal, about 8% of the pulse energy is focused in the flame of a welding torch by means of a beam splitter and a cylindrical lens. The LIF signal from the flame is detected by a photomultiplier attached to a monochromator set to 208 nm. This wavelength corresponds to the NO vibronic transition $D^2\Sigma^+(v'=0) \rightarrow X^2\Pi(v''=3)$. By means of two mirrors the remaining pulse energy is sent through the cylinder. This yields about 60 mJ/pulse at the location of the laser entrance window (this propagation direction is denoted by +). In order to verify the correction procedures the propagation direction of the laser beam through the cylinder may be reversed (this direction is denoted by -) by applying two more mirrors at the cost of 30 mJ/pulse, i.e., leaving 30 mJ/pulse at the opposite laser entrance window.

The cylinder of an air-cooled indirectly injected 4-stroke diesel engine (HATZ-Samofa) with a swept volume of about 580 cc (bore 86 mm, stroke 100 mm) is modified by mounting three cylindrical quartz windows (diameter 25 mm) in the cylinder wall as close to the cylinder head as possible. This construction provides optical access to the interior of the cylinder as long as the moving piston does not block the windows, i.e., for crank angles greater than 70° ATDC in the expansion stroke. Two of these three windows serve the purpose of transmitting the vertically oriented 25 mm high and 3 mm thick laser sheet, and the induced fluorescence is imaged through the third window in a direction perpendicular to the laser sheet. A spherical lens ($f=5.5$ cm) placed directly in front of this third window increases the field of view of the imaging system. The 2D-LIF signal is separated from the resonantly scattered laser radiation by means of a 13 nm bandwidth interference filter (Laser Optik, Garbsen, Germany) adjusted to maximum transmission ($\approx 80\%$) at 208 nm. The 2D-LIF signal is then fed into the 50 ns gated image intensifier in

front of the CCD-camera to be recorded on video tape for later processing. The background signal proved to be negligible with this setup [9]. The spherical lens in the detection path causes all images to suffer from spherical aberrations. Furthermore, growing transmission losses towards the edge of the imaged area are observed as a result of the decreasing collection efficiency of the detection system. However, the transmission in the central part of the detection path was measured to be higher than 75% within 90% of the radius of the imaged area. In this work the position of the spherical lens is fixed as to monitor an about 5 cm wide in-cylinder area.

An opto-electronic device continuously measures the crank position of the engine with an accuracy of about 1.2° . This device triggers a delay generator which in turn synchronizes the laser pulses, the LIF calibration section and the 2D-LIF imaging system. An adjustable water-cooled electric brake mounted on the flywheel of the engine provides various load conditions. Most of the NO imaging presented in this work is performed while the engine is running steadily (about 1000 rpm) on standard diesel fuel. A fixed amount of oxygen (circa 12%) is added to the inlet air of the running engine in order to raise the combustion temperature, resulting in an increased population of the probed ($v''=1$) state of NO. The increased combustion temperature also leads to decreased soot formation, and, as a consequence, a sufficiently high optical transparency of the quartz windows can be maintained over almost unlimited periods of time. The temperature of the exhaust gases is measured using a thermocouple mounted in the exhaust pipe approximately 5 cm from the cylinder. If the engine idles (no load) this temperature is typically 250°C and it gradually rises up to 400°C if the load is increased to 0.8 kW. Increasing the load any further eventually leads to critical temperatures in respect of the sealings for the windows in the cylinder wall. The pressure in the cylinder of the running engine is measured by replacing one of the quartz windows by a water-cooled pressure transducer (AVL QC 32) designed for pressures up to 20 MPa at high combustion temperatures. The output of this transducer is fed into a charge amplifier, the output of which is averaged over 50 cycles by a digital oscilloscope. This setup permits the in-cylinder pressure to be precisely monitored during the optically accessible parts of the combustion cycle.

The imaging hardware consists of an image processing board (Matrox PIP-1024 A/D converter) installed in a 486DX4 100 MHz personal computer. This board produces images with an 8 bits dynamic range consisting of 512 pixels x 512 pixels. The software provides the possibility to grab these images continuously and to display each grabbed frame in a number of different false colour representations on the screen of a separate RGB monitor. In contrast to many other image processing systems this system accepts input from a standard VHS video recorder as well, thus allowing for the off-line analysis of recorded 2D-LIF signals. Another relevant software option offers the possibility to add any number of grabbed frames in order to produce an averaged image. This is achieved by dividing the 512 pixels x 512 pixels array of added intensities by the number of frames grabbed and a subsequent re-scaling of the result to the full dynamic range.

4.2.2 The measuring sequence

Before each 2D-LIF measurement the intensity distribution of the laser sheet in the motored engine is averaged over about 300 Mie-scattered images by bypassing the

interference filter in front of the CCD camera (resonant scattering by residual particles). This measurement takes about two minutes. Next, the interference filter is re-installed and a 2D-LIF measurement in the running engine is performed over the next two minutes. Immediately after the 2D-LIF measurement the engine is motored again and the averaged intensity distribution of the laser sheet is measured in the same way as before. Any locally decreased transmissions caused by the gradual build-up of local soot deposits on the windows while the engine is running is spotted by a comparison of the two averaged intensity distributions of the laser sheet before and after the 2D-LIF measurement.

4.2.3 The double resonance setup

For the excimer laser induced fluorescence to be a reliable technique for NO detection, the excimer laser should not produce or destroy any NO by itself. In order to check that no such photo-chemical effects occur, a four-level double resonance experiment is performed, in which the NO fluorescence induced by a probe laser is monitored as a function of the presence or absence of the excimer laser. The experimental setup is schematically depicted in figure 4.2. A frequency-doubled pulsed dye laser, operated on Coumarin 47, is used as the probe laser, providing about 0.5 mJ/pulse at 226 nm (estimated pulse energy in the combustion chamber). This laser is used to excite rotational

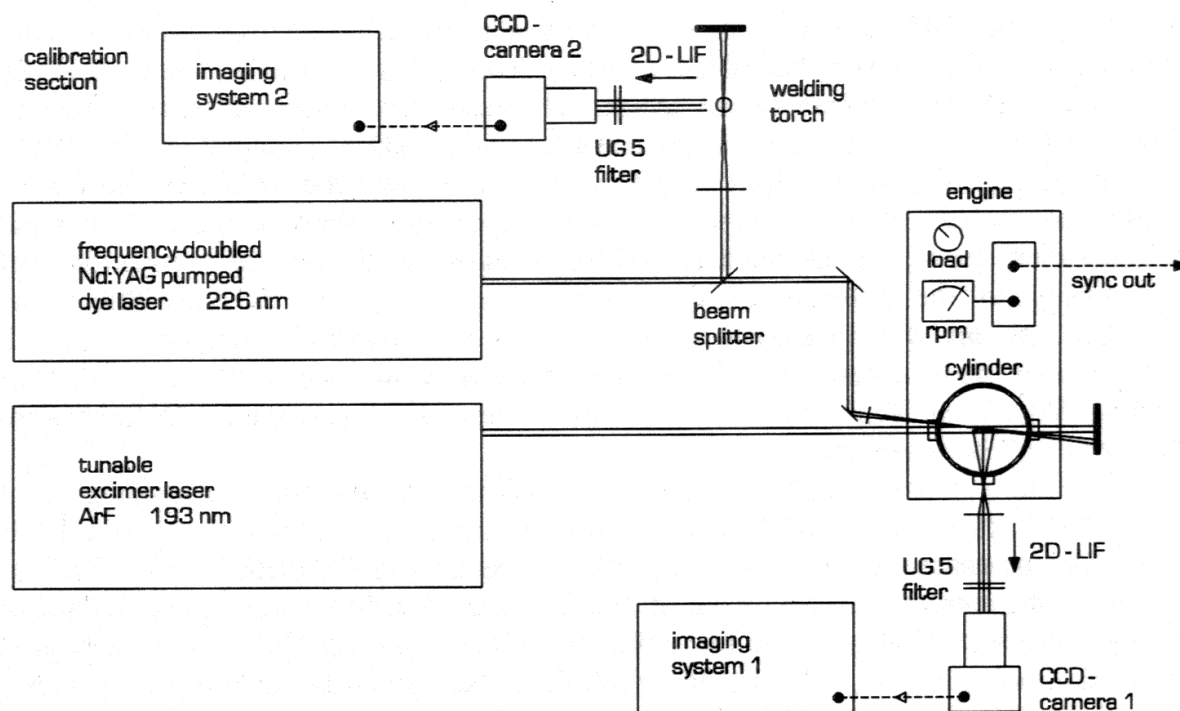


Figure 4.2 Schematic overview of the modified experimental setup

transitions in the $A^2\Sigma^+(v'=0) \leftarrow X^2\Pi(v''=0)$ band. The resulting fluorescence in the $A^2\Sigma^+(v'=0) \rightarrow X^2\Pi(v''=4)$ band at 272 nm is monitored by a gated intensified slow-scan CCD camera system (LaVision, FlameStar) through a 3 mm thick UG 5 filter. A spherical lens ($f=30$ cm) focuses the probe laser beam at the axis of the cylinder in such a way that

both laser pulses have maximum spatial overlap. When the excimer laser and the dye laser are applied together, the dye laser is delayed by 40 ns with respect to the excimer laser. This delay serves two purposes. On the one hand the excimer laser itself produces strong fluorescence at 272 nm, which, however, has decayed to a manageable level after 40 ns. Furthermore, the delay allows for equilibration of the NO population distribution following the excimer pulse, so that any photo-chemically induced change in the NO population might communicate itself to the level probed by the dye laser.

4.3 Signal processing

In spite of the high combustion temperature the running engine still produces enough soot to locally reduce the transmission of the quartz windows. These soot particles tend to mix with the lubricant of the engine and as a result sticky UV-absorbing deposits on the inner surfaces of the quartz windows may occur over longer periods of time. Although the initial locations of the deposits are rather unpredictable, changes in these locations during the measurements in the running engine are not observed. In fact, it turns out that after each session (taking about 45 minutes in which the engine is alternately fired and motored) the deposits can be thoroughly removed only by means of copper polish. If the laser entrance window happens to become locally blocked by these deposits the measured averaged NO fluorescence distribution displays corresponding horizontal areas of apparently lower NO concentrations as a result of the inhomogeneous intensity distribution in the laser sheet [9]. Whenever such deposits are formed on the inner surface of the window facing the camera the imaged NO distribution might also be misleading because of the locally decreased transmission of the 2D-LIF signal. However, by measuring the intensity distributions of the laser sheet in the cylinder immediately before and after each 2D-LIF measurement the corresponding averaged NO fluorescence distributions may easily be corrected for this effect. On top of that, the attenuation of the laser intensity in the cylinder of the running engine, means the NO fluorescence distributions, as initially measured, always display the largest NO signal on the side where the laser sheet enters the cylinder. In the following, two correction procedures accounting for all the above-mentioned effects on the initially imaged NO fluorescence distributions will be presented.

It is not yet possible to correct for the effects of collisional quenching on the measured NO fluorescence distributions. Due to inelastic collisions, a considerable decrease in the number of fluorescing NO molecules is brought about and as a consequence the intensity of the induced fluorescence is reduced (quenched). This will affect the total signal strength of the observed NO LIF distributions, thus making the determination of absolute NO densities difficult. Nevertheless, a reliable qualitative picture of the NO distribution may be obtained as a function of the in-cylinder pressure and the load of the engine, as will be shown in the next section. Experiments to study the dependence of the quenching rates of the induced fluorescence on the temperature, the pressure and the gas composition are in progress.

The correction procedures discussed below are based on the assumption that the sampled 2D-LIF signal strength depends linearly on both the laser pulse energy and the NO population density in the imaged area. The pulse energy of the ArF excimer laser is high enough to possibly cause saturation effects and/or photo-chemical processes (creating or dissociating NO) which, in turn, would adversely affect the required linearity of the

above-mentioned dependencies. For this reason, a number of experiments have been performed to investigate the extent to which the conditions for the signal processing procedures are met in the actual experimental circumstances. The results of these tests will be given in the next section. On the basis of these results the following assumptions are justified:

- The measurements at 193 nm excitation are non-intrusive, i.e., the observed 2D-LIF signal from the probed NO molecules is not influenced by photo-chemistry.
- The 2D-LIF intensity from NO in the running engine at 193 nm excitation and steady operating conditions depends linearly on the local laser intensity.

These assumptions form the basis for the following image processing procedures.

In general, the attenuation of both the laser intensity and the induced fluorescence inside the cylinder of the running engine may result from absorption and scattering by the multitude of different molecules and particles produced during combustion. It turns out that the attenuation due to photon absorption by NO molecules is negligible since the transmission of the laser sheet through the cylinder of the running engine is observed to be independent of the laser wavelength. Although probably not negligible, the in-cylinder attenuation of the NO LIF signal itself is expected to be more or less uniform over the imaged area. The dominant laser attenuation mechanism turns out to result from absorption and Mie scattering by particles. The resonantly scattered 2D signal will be a measure for the laser intensity distribution in the imaged in-cylinder area, provided the differently sized scattering particles are more or less uniformly distributed within the imaged area. This condition is thought to be met on the basis of the experimental results presented in the next section. It will be shown that even in the motored engine, due to the presence of many residual soot particles, the in-cylinder laser intensity distribution can be measured this way.

The scattered intensity $S(x,y)$ from any point (x,y) in the imaged area is proportional to the local laser intensity $I(x,y)$ and to the local density $n_s(x,y)$ and the cross-section $\sigma_s(x,y)$ of the scattering particles:

$$S(x,y) \sim n_s(x,y) \sigma_s(x,y) I(x,y) . \quad (4.1)$$

The laser intensity distributions $I_B(x,y)$ and $I_A(x,y)$ in the motored engine before and after the 2D-LIF measurement are reflected by the imaged Mie-scattered intensities $S_B(x,y)$ and $S_A(x,y)$, respectively. Assuming that both the 2D-LIF signal and the scattered signals are attenuated in the same way, the evaluation of the fraction $S_B(x,y)/S_A(x,y)$ over the imaged area provides a numerical measure to correct the imaged NO fluorescence distribution for any locally decreased window transparency caused by soot deposits during combustion. This correction is performed by multiplying the intensity of the initially measured NO fluorescence distribution $S_{NO}^0(x,y)$ by the value of $S_B(x,y)/S_A(x,y) = I_B(x,y)/I_A(x,y)$. The result of this correction is re-scaled by a known factor, α , to the full dynamic range of the imaging system. The resulting image then represents the NO fluorescence distribution as would be observed in the running engine if the windows were to stay perfectly clean during the measurements.

However, in order to reconstruct more realistic NO LIF distributions a correction for the attenuation of the intensity of the laser sheet in the cylinder of the running engine has to be performed as well. Theoretically, the decay of the intensity I of a laser beam along its propagation direction (x) in a scattering and absorbing medium is described by:

$$I(x,y) = I(x_0,y) \exp\left(-\int_{x'=x_0}^{x'=x} [n(x',y)\sigma(x',y)] dx'\right), \quad (4.2)$$

where $n(x,y)$ and $\sigma(x,y)$ represent the average density and the average cross-section of the absorbing and scattering particles in the medium, respectively. Evaluating the distance x in terms of camera pixel units, one may write:

$$I(x+1,y) = I(x,y) \exp[-n\sigma]_{\text{eff}}(x,y), \quad (4.3)$$

expressing the decay of the laser intensity per unit distance in the propagation direction. Inserting eq. (4.1) and rearranging eq. (4.3) yields the decay of the in-cylinder laser intensity per unit distance in terms of the Mie-scattered signal $S_R(x,y)$ as measured in the running engine:

$$\exp[-n\sigma]_{\text{eff}}(x+1,y) = \frac{[n\sigma]_{\text{eff}}(x,y)}{[n\sigma]_{\text{eff}}(x+1,y)} \frac{S_R(x+1,y)}{S_R(x,y)}. \quad (4.4)$$

Assuming the distribution of the scattering particles to be more or less homogeneous in the imaged area, it follows that the decay per unit distance at any location (x,y) may be approximated by $S_R(x+1,y)/S_R(x,y)$. Along the path of the laser sheet, the integrated decay is evaluated by multiplying the product of all previous fractions (varying around values slightly below unity) by the fraction found at the location (x,y) . The actual correction for the attenuation of the laser intensity is performed by multiplying the local intensities of the input distribution (i.e., the result of the first correction procedure) by the inverted integrated decay factor found at the corresponding points in the Mie-scattered images. Again, the result of this second correction is re-scaled by a known factor, β , to the full dynamic range of the imaging system.

Summarizing, the fully corrected result $S_{\text{NO}}(x,y)$ is calculated by the evaluation of the following expression:

$$S_{\text{NO}}(x,y) = \beta \frac{S_R(x_0,y)}{S_R(x,y)} \alpha \frac{S_B(x,y)}{S_A(x,y)} S_{\text{NO}}^0(x,y). \quad (4.5)$$

Demonstrations of both correction procedures applied to two typical NO fluorescence distributions recorded in the same session with opposite propagation directions of the laser sheet in the running engine (135° ATDC, 1000 rpm, no load) are given in figure 4.3 (+ direction) and figure 4.4 (- direction). Both figures consist of a set of eight three-dimensional representations of all images involved in the signal processing. The plots labelled A display the Mie-scattered laser intensity distributions in the motored engine with cleaned windows ($S_B(x,y)$ in eq. (4.5)). The plots labelled B are depictions of

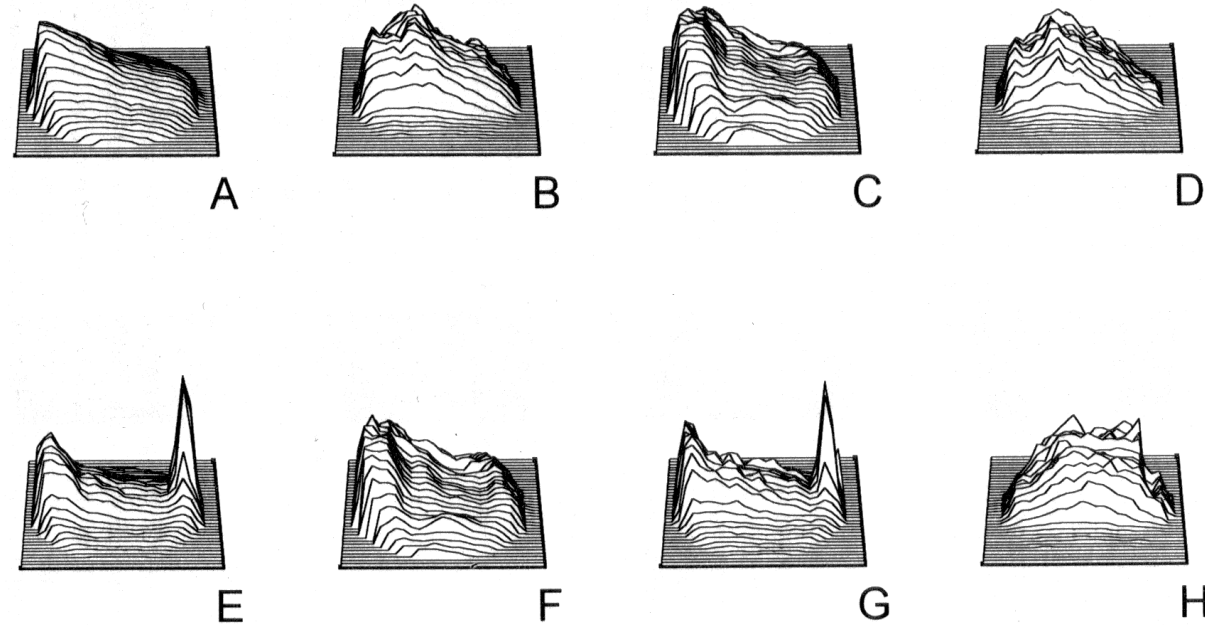


Figure 4.3 Stages in the post-processing of NO fluorescence images (135° ATDC). In these 3D representations the vertical axis represents the intensity over the imaged area (xy -plane). The laser sheet travels from left to right (+ direction). See the text for the measurement sequence and the processing details. The symbols between $[\]$ are the ones used in eq. (4.5). A: In-cylinder laser intensity distribution (derived from Mie- scattering intensities) in the motored engine directly before the LIF measurement $[S_B(x,y)]$; B: NO LIF distribution $[S_{NO}^0(x,y)]$; C: As A, immediately after the LIF measurement $[S_A(x,y)]$; D: NO LIF distribution (from B) after correction for window fouling (using A and C) $[(S_B/S_A) \cdot S_{NO}^0]$; E: In-cylinder laser intensity distribution in the running engine $[S_R^0(x,y)]$. The spike on the right hand side is due to a spurious reflection; F: As A, directly after the Mie measurement of E $[S_A(x,y)]$; G: In-cylinder laser intensity distribution (from E) after correction for window fouling (using A and F) $[S_B/S_A \cdot S_R^0]$; H: NO distribution (from D) after correction for laser attenuation (using G) $[S_{NO}(x,y)]$

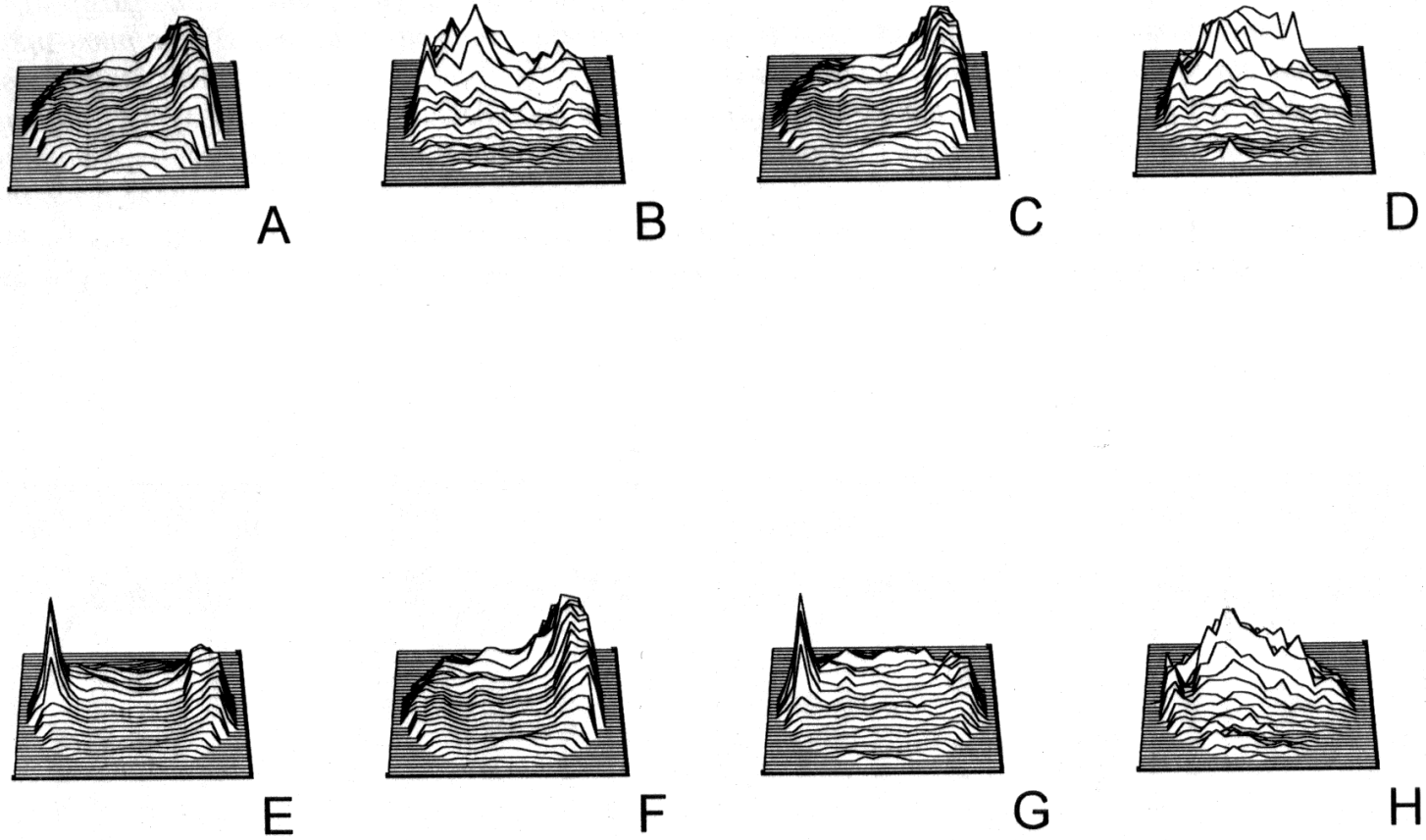


Figure 4.4 *As fig. 4.3, but with the laser beam reversed (- direction)*

the measured NO fluorescence distributions ($S_{\text{NO}}^0(x,y)$ in eq. (4.5)). The plots labelled C show the in-cylinder laser intensity distributions measured in the motored engine immediately after the NO measurements ($S_A(x,y)$ in eq. (4.5)). The plots labelled D in the figs. 4.3 and 4.4 display the results of the correction procedure for locally decreased transmissions of the windows as a result of soot deposits. Comparing plot B in fig. 4.4 with plot D in fig. 4.4 one observes a shift in the corrected NO distribution towards the centre of the imaged area, whereas in the other direction (with apparently little window fouling) this first correction hardly affects the initially imaged NO fluorescence distribution (plot B in fig. 4.3). The plots labelled E show the Mie-scattered intensity distributions in the cylinder of the running engine. The high intensities at the laser exit sides as displayed by plots E in the figs. 4.3 and 4.4 are artifacts, most probably caused by reflections of the laser sheet at the inner surface of the laser exit window. It turns out that the overall transmission of the laser through the cylinder is about two times higher if the engine is running ($\approx 20\%$) instead of being motored ($\approx 10\%$). An explanation is most likely to be found in the higher in-cylinder temperature of the running engine, causing the vaporization of lubricant droplets. This may be expected to reduce the scattering losses in the cylinder of the running engine and as a result the reflections at the laser exit window are stronger than those in the motored engine. The plots labelled F are Mie-scattered images from the motored engine measured immediately after the Mie-scattering measurements in the running engine (plots E). The plots A and F are used to perform the first correction procedure on the plots E and the results are shown in plots G in the figs. 4.3 and 4.4. The latter form, in combination with the corrected NO fluorescence distributions (plots D), the ingredients of the second correction procedure, which accounts for the decreasing laser intensity over the field of view. Finally, the plots labelled H are depictions of the fully corrected NO fluorescence distributions. It should be noted here that the fully processed NO distributions, like plots H in the figs. 4.3 and 4.4, typically show more centralized NO distributions in comparison to the original, uncorrected, fluorescence distributions (plots B). The effect of the 50% lower laser pulse energy in the - direction is reflected by the noise recorded from locations below and above the laser sheet (fig. 4.4, plot B). Nevertheless, after two corrections, similar in-cylinder NO fluorescence distributions are found, independent of the propagation direction of the laser sheet. This is a strong indication for the reliability of the signal processing procedures and the resulting in-cylinder NO distributions.

4.4 Results and discussion

4.4.1 Validation of the detection method

4.4.1.1 Two-colour excitation

In figure 4.5 two NO excitation scans of the 226 nm region measured with the frequency-doubled dye laser in the running engine and in the welding torch, respectively, are presented. A simulated spectrum, calculated for $T=1800$ K by using data from Reisel *et al.* [31] is given in the row in the middle. The three spectra show very good agreement. Evidently, the spectrum obtained from the engine is much weaker than the flame spectrum. The strongest rotational resonance ($P_2(22.5)$ at 226.364 nm [31]) was selected

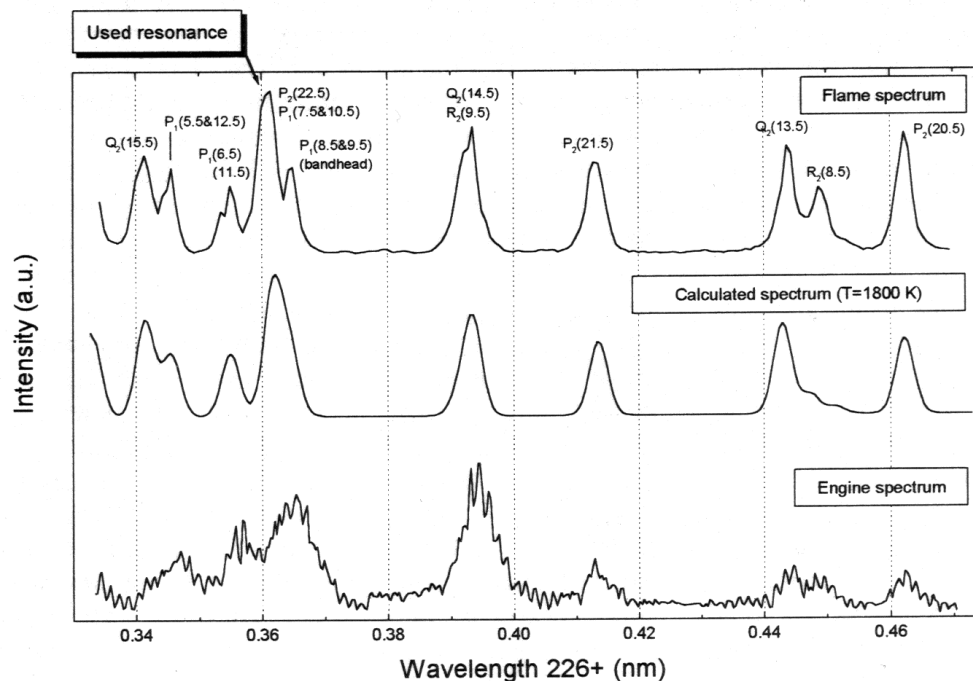


Figure 4.5 Three NO excitation scans around 226 nm. The top scan is measured with the LaVision imaging system in the welding torch and serves as a reference scan. The $P_2(22.5)$ rotational resonance selected for the two-colour experiments in the running engine is indicated in this scan as well. The scan in the middle is simulated for $T=1800$ K on the basis of data of Reisel et al. [31]. The bottom scan is measured in the running engine with the LaVision imaging system

to check for any photo-chemical effects induced by the excimer laser radiation. The effect of the presence of the excimer laser radiation on the dye-laser-induced fluorescence signal strength from the running engine (BDC, 1000 rpm, no load) is depicted in figure 4.6. As can be clearly deduced from this figure, the observed influence of the excimer laser radiation does not exceed the experimental accuracy in view of the contribution of the excimer laser alone (sequence 5). On the evidence of fig. 4.6, it is concluded that excimer-laser-induced photo-chemical processes, if they occur at all, have no observable influence on the population of the $X^2\Pi(v''=0)$ state under the present experimental circumstances. In view of the fast vibrational relaxation of NO [41] this most probably holds for the $X^2\Pi(v''=1)$ state (probed by the excitation at 193 nm) as well.

4.4.1.2 Dependence of the LIF signal on laser power

The linearity of the LIF signal strength in the running engine (BDC, 1100 rpm, 0.4 kW load) with the excimer laser pulse energy was tested in the experimental setup of fig. 4.1 using the $R_1(23.5)/Q_1(29.5)$ resonance. The result is given in figure 4.7. The data points

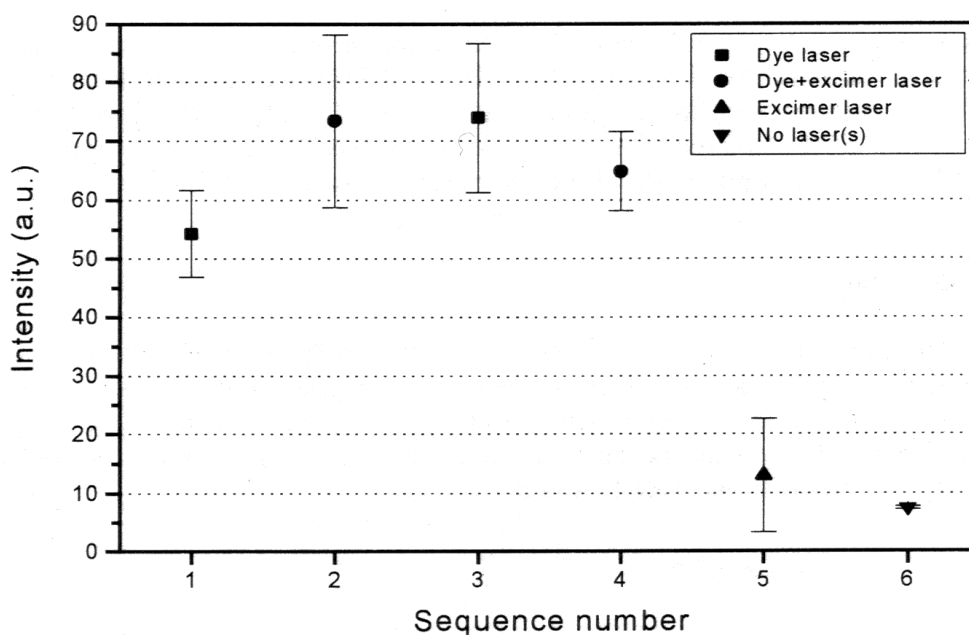


Figure 4.6 Averaged NO 2D-LIF signal strengths at 226.364 nm dye laser excitation in the presence and the absence of 193.558 nm excimer laser excitation as measured in the running engine (BDC, 1000 rpm, no load) with the LaVision imaging system

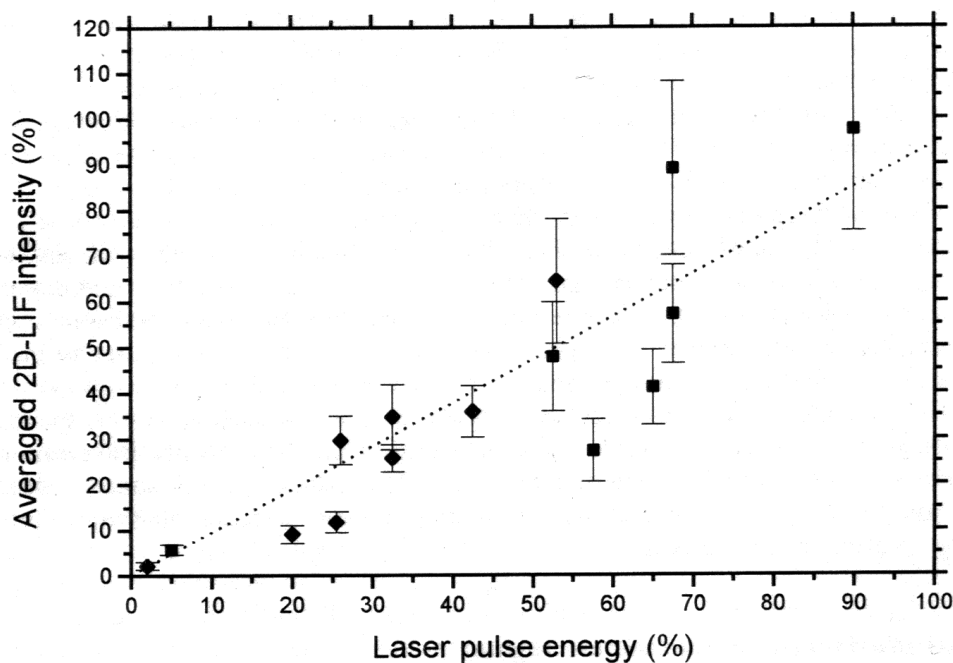


Figure 4.7 Normalized dependence of the NO 2D-LIF intensity from the running engine (BDC, 1100 rpm, 0.4 kW load) on the excimer laser pulse energy. The dotted line represents a best linear fit through the data, with a slope of 0.94(8)

represent averages over 50-100 laser shots and were recorded in different sessions on different days (indicated by different symbols in fig. 4.7). Although there is considerable scatter, there is no evidence for a non-linear behaviour of the LIF yield with laser pulse energy. In view of the irreproducible nature of the combustion itself, we believe this is a sufficient basis for the applicability of the correction methods outlined above.

4.4.1.3 Saturation

The mere linearity of the LIF signal strength with the excitation laser pulse energy does not necessarily imply that saturation is absent. An estimate of the degree to which saturation plays a role in the experiments described here, can be obtained by comparing the actual laser intensity with the saturation intensity. Assuming dominant homogeneous broadening, the saturation intensity I_s is defined as [56]

$$I_s = \frac{c R_{av} \Delta\nu}{B_{12}} , \quad (4.6)$$

with c the velocity of light, R_{av} the average relaxation rate of upper and lower level, B_{12} the Einstein coefficient for (stimulated) absorption and $\Delta\nu$ the laser bandwidth. Although R_{av} and B_{12} are not known for the $D \leftarrow X$ transition, they can be estimated. B_{12} is related to the Einstein coefficient A_{21} through

$$B_{12} = \frac{\lambda^3}{4h} A_{21} . \quad (4.7)$$

For the $D^2\Sigma^+(v'=0)$ state, the electronic lifetime $\tau_{el} = 0.018 \mu\text{s}$ [52], which poses an upper limit to A_{21} of $5.6 \times 10^7 \text{ s}^{-1}$. If the experimentally observed linewidth of 2 cm^{-1} (at 1 bar) [9] is attributed solely to homogeneous broadening, this yields $R_{av} \approx 6 \times 10^{10} \text{ s}^{-1}$ and this value will rapidly increase with increasing pressure. This results in $I_s \geq 2 \times 10^9 \text{ W/m}^2$ for $\Delta\nu = 0.5 \text{ cm}^{-1}$, which is about five times smaller than our most optimistic estimate of the in-cylinder laser intensity. Empirical direct information on the degree of saturation may be obtained from V-type three-level double resonance experiments, which are planned for the near future. It should be noted that even in case of saturation the LIF signal strength is still linearly proportional to the local NO density.

The conditions for the correction procedures are reasonably met in the actual experimental setup. Photo-chemical reactions affecting the NO density by creation or destruction of NO molecules were not observed. The 2D-LIF signal strength depends linearly on the laser pulse energy and saturation effects affecting that linearity will probably be of minor importance.

4.4.2 NO distributions in the running engine

Figure 4.8 shows the numerical effects of the first correction procedure (for window pollution) on a number of averaged NO fluorescence intensities measured for both directions of the laser beam and at selected loads of the engine. These data are produced

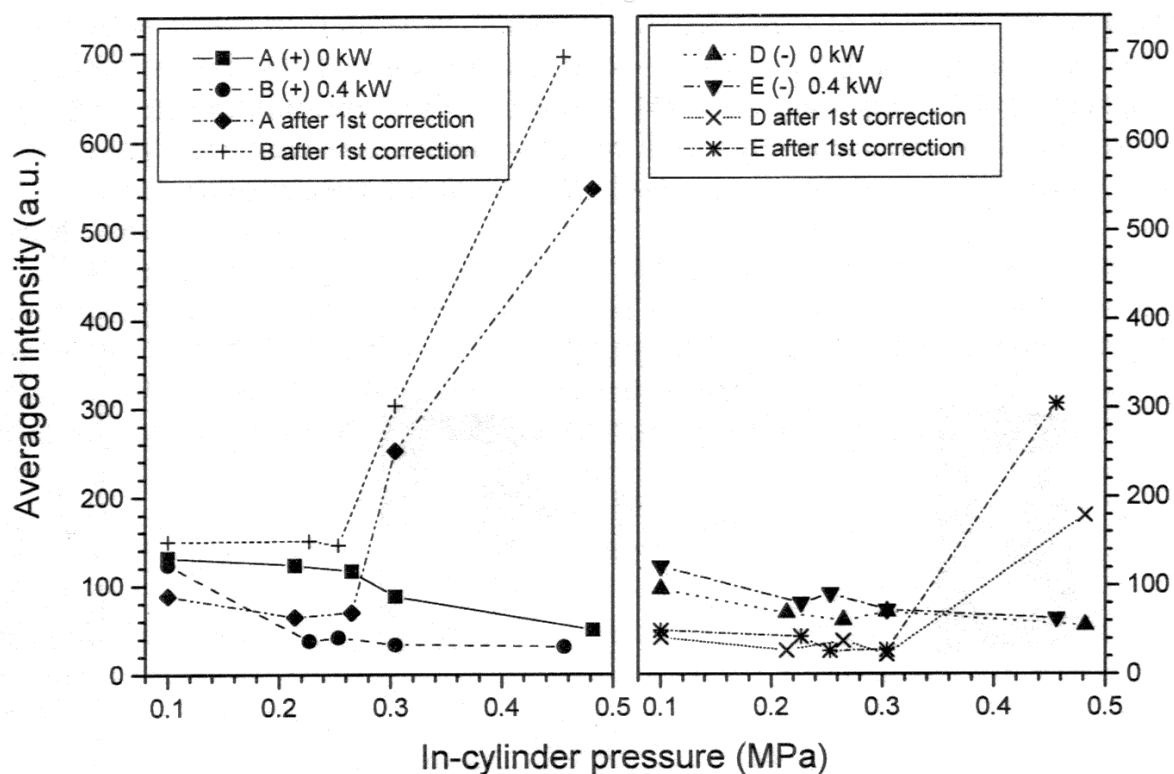


Figure 4.8 Initially measured averaged NO fluorescence intensities per pixel for four series of measurements at the selected crank angles in both laser directions with and without a 0.4 kW load. The actual laser directions and loads are indicated in the legend. The corresponding values after the correction for soot deposits on the windows are plotted in this figure as well

by bypassing the re-scalings to the full dynamic range of the imaging software (factor α in eq. (4.5)). Although the (second) correction for the attenuation of the laser beam remains to be performed, instead of the initially observed decay of the averaged fluorescence intensities towards higher pressures, one already observes an increase in the 2D-LIF signal strength after the first correction procedure in all four series. This is in line with the expectation that there exist higher NO densities at higher pressures. In the + direction the increase starts at 120° ATDC whereas in the - direction the corrected signal starts increasing at 105° ATDC (irrespective of the load in both cases). This difference is most probably an artefact caused by the about two times lower pulse energy of the laser in the - direction, leading to proportionally weaker 2D-LIF signals. However, as expected, in both directions the signals at 80° ATDC (around 0.47 MPa) are significantly stronger in case the engine is loaded.

In figure 4.9 four initially measured NO fluorescence distributions are given in the top row and the corresponding results after both corrections are depicted in the bottom row. From left to right these distributions were measured in the + direction in the same session (lasting 30 minutes at least) at: 135° ATDC, 120° ATDC, 105° ATDC and 80° ATDC in the expansion stroke (1000 rpm, no load), respectively. The shift in the initially measured NO fluorescence distributions (top row) at higher in-cylinder pressures towards

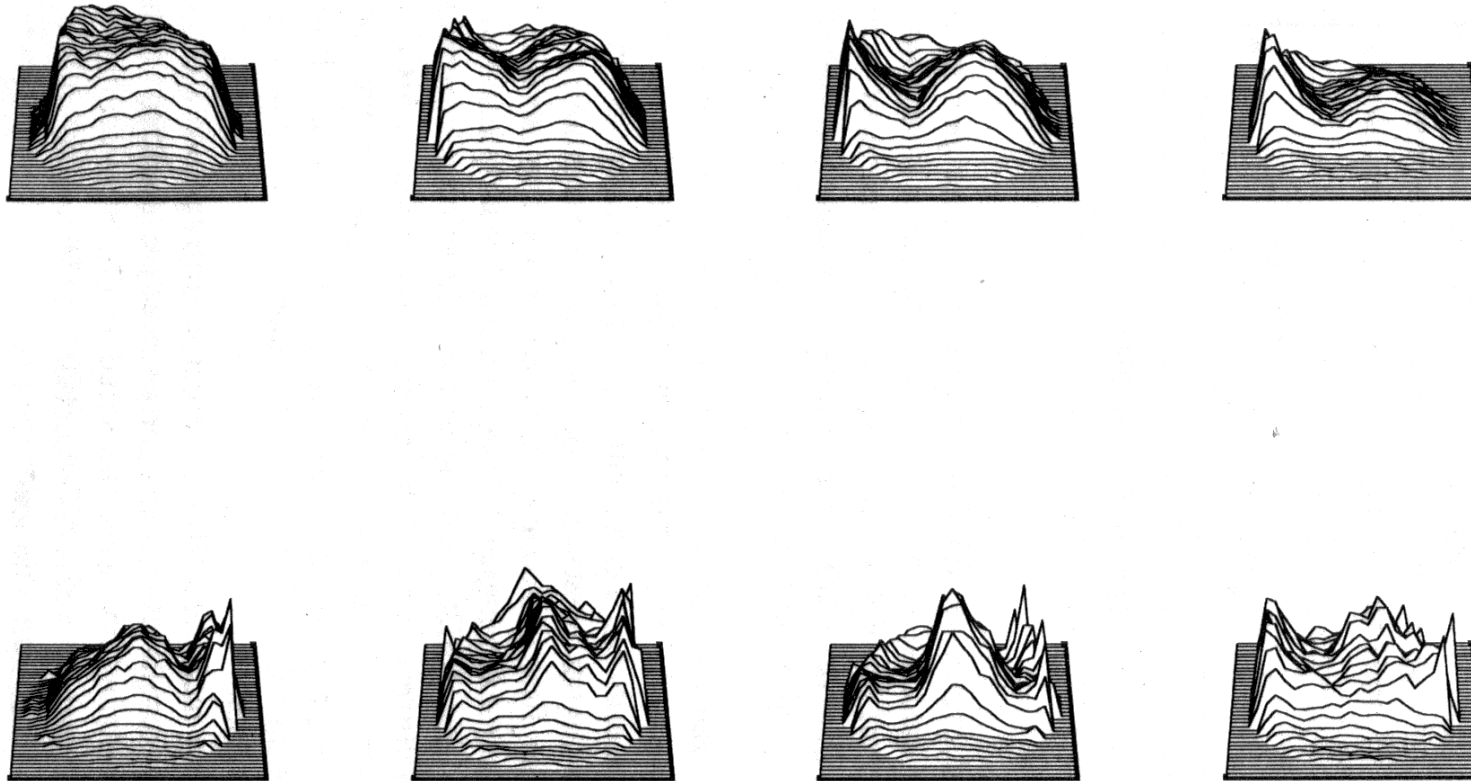


Figure 4.9 Four representations of initially measured NO fluorescence distributions in the + direction of the laser sheet are depicted in the top row. From left to right these distributions were measured at: 135° ATDC, 120° ATDC, 105° ATDC and 80° ATDC (1000 rpm, no load), respectively. The bottom row shows the corresponding results if the distributions of the top row are corrected for both the soot deposits and the in-cylinder laser intensity attenuation

the side of the laser entrance window is considered to be the result of the increasing in-cylinder attenuation of the laser intensity. After both corrections the resulting NO distributions tend to shift towards the centre of the imaged area (i.e., the part of the image which suffers the least from spherical aberrations) in spite of the gradual build-up of soot deposits on the observation window. The high intensities at the borders of the fully corrected distributions result mainly from inaccuracies in the second correction procedure near the image edges.

The laser intensity distributions as measured by Mie-scattering in the running engine ($S_R(x,y)$ in eq. (4.5)) corresponding to the session depicted in fig. 4.9, are given in figure 4.10. The evaluation of the fractions $S_R(x,y)/S_R(x+1,y)$ contained in these images provides a way to estimate the values of the product $[n\sigma]_{\text{eff}}(x,y)$ of eq. (4.3) in the running engine. This can be seen by rearranging eq. (4.4) in order to obtain:

$$\frac{S_R(x,y)}{S_R(x+1,y)} = \frac{[n\sigma]_{\text{eff}}(x,y)}{[n\sigma]_{\text{eff}}(x+1,y)} \exp[+n\sigma]_{\text{eff}}(x+1,y) . \quad (4.8)$$

Expanding the exponential term at the right hand side and neglecting quadratic and higher order terms yields:

$$\frac{S_R(x,y)}{S_R(x+1,y)} = \frac{[n\sigma]_{\text{eff}}(x,y)}{[n\sigma]_{\text{eff}}(x+1,y)} + [n\sigma]_{\text{eff}}(x,y) . \quad (4.9)$$

Since the scattering particles are assumed to be more or less homogeneously distributed, the first term on the right hand side reduces to unity. The values for $[n\sigma]_{\text{eff}}(x,y)$ are then found to typically vary around ≈ 0.005 . On the evidence of this evaluation of the laser intensity distributions, the scattering particles in the running engine seem to be more or less homogeneously distributed within the imaged area indeed. Similar distributions and values are obtained for scattering along the - direction.

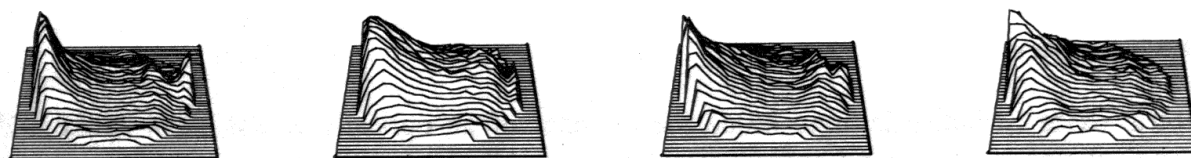


Figure 4.10 From left to right, four representations of in-cylinder laser intensity distributions in the running engine after the correction for soot deposits on the windows, are shown. The (scattered) distributions were initially imaged in the + direction at: 135° ATDC, 120° ATDC, 105° ATDC and 80° ATDC in the expansion stroke (1000 rpm, no load), respectively. These intensity distributions are actually involved in the correction for the in-cylinder laser attenuation of the NO fluorescence distributions given in the top row of fig. 4.9

Finally, the results of the numerical analysis performed on the averaged 2D-LIF signal strength of the initially measured NO fluorescence distributions given in fig. 4.9 before and after both corrections (involving both scale factors α and β in eq. (4.5)) are plotted in figure 4.11. The corrected signal at 80° ATDC is about 23 times stronger than the measured 2D-LIF signal. Since the effect of collisional quenching on the signal strength is not yet known, one must be very careful in drawing conclusions about the absolute amount of NO from this figure.

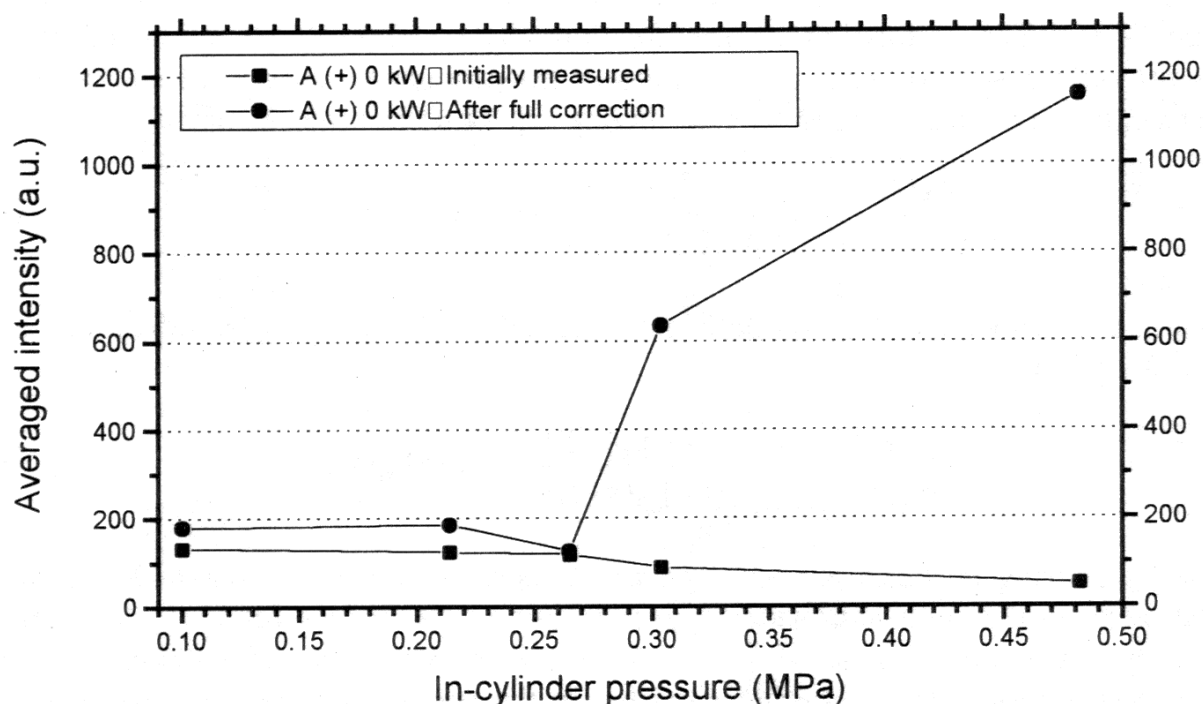


Figure 4.11 The results of the numerical analysis performed on the averaged intensities of the initially measured NO fluorescence distributions given in fig. 4.9 before and after correction for soot deposits on the windows as well as for the in-cylinder laser attenuation

4.5 Summary

Nitric oxide LIF distributions inside the cylinder of an optically accessible 4-stroke IDI diesel engine running on standard diesel fuel are presented. These NO distributions are obtained by using 2D fluorescence imaging induced by an ArF excimer laser ($\lambda \approx 193$ nm). Correction procedures were developed to take into account the effects of window fouling and in-cylinder laser attenuation due to scattering by a uniform field of soot particles. The correction procedure for window fouling is efficient enough for measurement sessions to last up to ca. 45 minutes. These numerical image processing procedures are an essential step towards the quantitative interpretation of the fluorescence distributions. In contrast to the measured NO fluorescence distributions (the "raw data"), the processed distributions are shown to be hardly dependent on the direction in which the excitation laser traverses the engine. This is good evidence to justify the interpretation of the corrected images as relative NO density distributions.

The excimer laser itself is found not to induce observable photo-chemical effects. The LIF signal is shown to depend linearly on the laser intensity. Also, saturation is expected to play a minor role in this work.

In the range of 80° - 180° ATDC, NO is found to be located in the central part of the cylinder. Its density is found to increase with increasing load and with decreasing crank angle. The latter trend is born out of the processing of the raw data. At the current state of knowledge, a quantitative interpretation of the NO LIF signal is hampered by the lack of data on the collisional quenching of the $D \rightarrow X$ fluorescence under the conditions prevailing in a diesel engine.

Chapter 5

Approaches to the Quantitative Interpretation of Laser-Induced Fluorescence from NO in an IDI Diesel Engine

Abstract

By means of a tunable ArF excimer laser, producing radiation around 193 nm, laser-induced fluorescence distributions of NO in the optically accessible cylinder of a standard diesel fuel driven diesel engine are imaged at selected crank angles and loads. Excitation scans of in-cylinder NO from the steadily running engine are presented. The imaged NO fluorescence distributions are subsequently corrected for locally decreased transmissions due to soot deposits on the windows as well as for the in-cylinder attenuation of the laser intensity. To study the correlation between reconstructed LIF signals at the end of the expansion stroke and typical exhaust gas concentrations as measured as a function of the engine load, the pixel-averaged 2D-LIF signal strength contained in the image-processed distributions is numerically corrected for the effects of collisional quenching and overall temperature effects on the basis of a simplified fluorescence model.

5.1 Introduction

Driven by an ever growing environmental awareness, the study of the very complex combustion processes in diesel engines by means of the (combined) application of a variety of laser-based imaging techniques, like Laser-Induced Fluorescence (LIF) and Laser-Induced Incandescence (LII), has made great progress in recent years. Yet, the chemistry and the physics of the actual combustion processes are still far from being fully understood. Because of this, most manufacturers still have to rely on empirical solutions in order to achieve further reductions of the toxic emissions of their engines. In view of the development of new approaches any information on where and when in the combustion process the most polluting chemicals are produced or transformed, is extremely valuable.

It should be noted that the in-cylinder environment is rather inhospitable for laser spectroscopy due to the high pressures and the soot which is inevitably produced during diesel fuel combustion. For the latter reason most of the research reported is performed in optically accessible research engines using low-sooting substitute fuels while the engines are usually running in a so-called skip-fired mode, i.e., the combustion is only initiated after any selected number of cycles. Although these precautions may allow for a high transparency of the access channel to be maintained over longer periods of time, for obvious reasons, the actual circumstances in the cylinder of a realistic steadily running diesel engine driven by standard diesel fuel will certainly differ from these simulated circumstances. In a previous publication on this topic [9] excitation scans recorded at BDC in a 4-stroke IDI diesel engine using diesel fuel and n-heptane are presented. Here, excitation scans from the loaded engine recorded at different crank angles (i.e., different pressures and temperatures) using standard diesel fuel are presented.

In another previous publication [13] a method is introduced by which the initially observed NO fluorescence distributions are corrected for the effects of the gradual build-up of soot deposits on the inner surfaces of the windows as well as for the in-cylinder extinction of the laser radiation. This procedure has been used for the present work also. The quantitative determination of NO concentrations from these corrected LIF distributions is hampered by unknown collisional quenching of the fluorescence as well as rotational energy transfer (RET) in the electronic ground state and in-cylinder temperature gradients affecting the Boltzmann distributions, respectively. Due to collisional quenching a considerable reduction of the fluorescence signal is brought about at rising pressures and temperatures. Whereas the quenching of the NO fluorescence at 226 nm excitation has been widely studied (e.g. [31,32,35,38,39,42,46-50]) relevant experimental data on the quenching at 193 nm excitation or the ground state RET rates are not yet found in literature. In this work a simplified fluorescence model, adapted from the above mentioned 226 nm excitation studies and as such neglecting ground state RET, is applied to the 2D-LIF signal strength observed in the image-processed NO distributions. As will be shown the NO fluorescence yield at 193 nm excitation is sensitive to in-cylinder temperature gradients, although not very strongly. Nevertheless, in the interpretation of the obtained NO distributions these temperature gradients over the imaged area have to be taken into account.

5.2 Experimental

The experimental setup is described in detail in the previous publications [9] and [13] and therefore only a brief description will be given in this section. Three quartz windows (25 mm diameter) are mounted as high as possible in the cylinder wall of the single-cylinder (bore 86 mm, stroke 100 mm) air-cooled 4-stroke IDI diesel engine (HATZ-Samofa). The distance of the top edges of the windows to the cylinder head is about 15 mm, allowing optical access to the interior events for crank angles larger than about 40° ATDC. Full access (i.e., the top of the piston reaches the bottom edges of the windows) is obtained for crank angles larger than about 70° ATDC. The inlet valve opens at 1.5° BTDC and it closes at 18° ABDC, whereas the exhaust valve opens at 23° BBDC to be closed again at 1.5° BTDC. The injection of the fuel is adjusted to start at 15° BTDC. Due to the modification of the cylinder the compression ratio of 1:8 is somewhat lower than usual. Loads are provided by an adjustable water-cooled electric brake (Zollner & Co) mounted on the flywheel of the engine and the resulting exhaust gas NO_x concentrations are on-line recorded by means of an AEG 4000 NO_x monitor. An opto-electronic device allows for the synchronization of both the laser and the detection equipment to the position of the crank with an accuracy of about 1.2°. The engine is operated at 1000 rpm on standard diesel fuel with a minimum amount of lubricant and about 10% extra oxygen supplied to the air inlet. By means of a pressure transducer (AVL QC 32) mounted instead of one of the windows, the in-cylinder pressure may be measured whenever the piston does not block the windows (i.e., whenever the interior is optically accessible). In figure 5.1 the in-cylinder pressure measured this way at the operating conditions of the engine relevant to this work is plotted versus the crank angle.

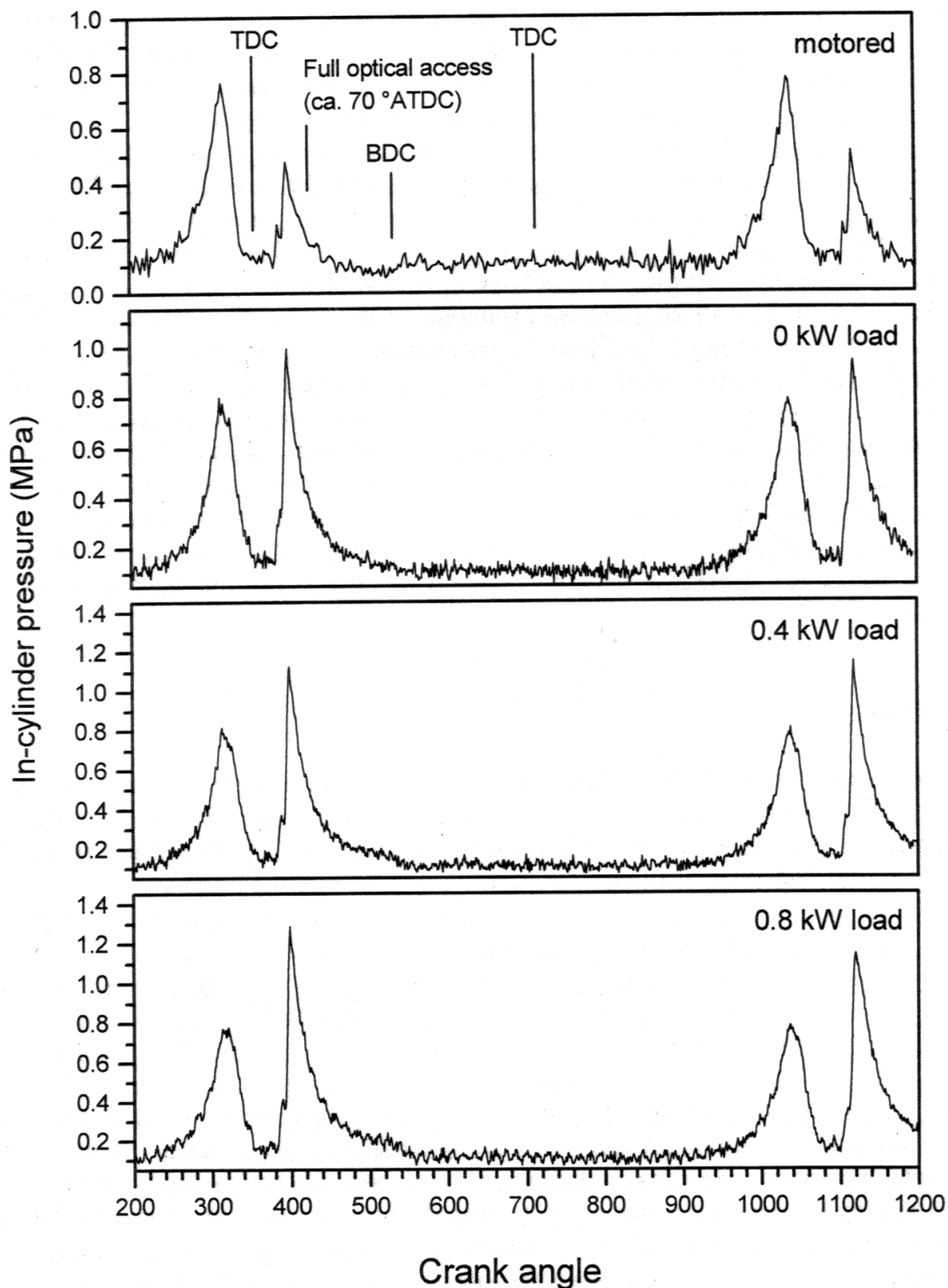


Figure 5.1 *In-cylinder pressure as a function of the crank angle as measured at selected engine loads and in the motored engine. As a consequence of its mounting position (i.e., instead of one of the windows), the pressure transducer is also temporarily blocked by the moving piston leading to erroneous signals near TDC*

The tunable ArF excimer laser (Lambda Physik EMG 150 MSCT) delivers about 100 mJ of 193 nm radiation in pulses of 13 ns duration. By means of a beam splitter and two mirrors a fraction of the vertically oriented laser sheet (2.5 cm high, 3 mm thick) is led to the flame of a welding torch for calibration purposes, whereas the remaining laser radiation is made to traverse the interior of the cylinder in a horizontal direction. Room temperature absorption of the laser radiation by molecular oxygen and intensity losses at beam splitter and mirrors lead to an overall reduction of the laser pulse energy of about 40% when measured at the position of the laser entrance window. The NO fluorescence signal at 208 nm from the calibration flame is monitored on-line. This wavelength corresponds to the vibronic transition $D^2\Sigma^+(v'=0) \rightarrow X^2\Pi(v''=3)$ of NO, which is one of many that occur within 50 ns after the excitation of the coinciding rotational resonances $R_1(23.5)/Q_1(29.5)$ at 51656.2 cm^{-1} [44] in the transition $D^2\Sigma^+(v'=0) \leftarrow X^2\Pi(v''=1)$. The in-cylinder laser-induced fluorescence is monitored in a direction perpendicular to the laser sheet through the third window by means of an interference filter (adjusted to about 80% transmission at 208 nm with less than 1% transmission for wavelengths outside the 201-220 nm region) and a 50 ns gated imaging system based on a temperature controlled intensified CCD-camera (ICCD-576/RB-E, Princeton Instruments). This system is used with a 12-bits dynamic range and the resulting images (in this work background-subtracted 100-shots averages) may be compressed and stored on hard disk for later processing.

5.3 Modelling

The fluorescence yield Y in photons/sec at any given resonance, pressure p and temperature T will depend on a number of parameters which, in turn, may also depend on the pressure and temperature. In the model employed by Battles *et al.* [46] this is expressed by the following relation

$$Y = C_{\text{ex}} (k_{12} p \chi_{\text{NO}}) g(\phi_{\text{NO}}, \phi_{\text{las}}) I \frac{A_{21}}{\frac{p}{k_B T} \sum_i \chi_i \sigma_i(T) \sqrt{\frac{8k_B T}{\pi \mu_i}}} \quad (5.1)$$

with C_{ex} as a group of experimental constants including the cross sectional area of the laser beam, the measurement volume and the collection solid angle as well as the wavelength dependent transmission efficiency. The NO absorption line strength in $\text{cm}^{-2} \text{ Pa}^{-1}$ is given by k_{12} whereas p and χ_{NO} represent the total pressure in Pa and the NO mole fraction, respectively. Note that k_{12} contains the fractional population density of the ground state $\eta_1(T)$ as well as molecular constants like the Franck-Condon and Hönl-London factors. The laser energy flux is represented by I and the last factor of the right hand side stands for the high-pressure Stern-Vollmer factor (A_{21}/Q_2) with A_{21} as the Einstein coefficient for spontaneous emission and Q_2 specified as the sum over all colliding species i of the product of the colliding species specific number densities $n_i = p\chi_i/k_B T$ (χ_i

represents the colliding species specific mole fraction), the thermally averaged⁴ collision cross sections $\sigma_i(T)$ and the relative velocity of the collision partners (with μ_i as the reduced mass of the collision partners), respectively. It should be noted here that although the thermally averaged cross sections for collisions of NO with O₂ and N₂ at 193 nm excitation are studied in more detail in the last chapter of this thesis, due to the lack of data on the gas composition and the temperature dependence of the various cross sections of NO in collisions with many other components, in the present modelling the sum (i.e., $\sum_i[\chi_i\sigma_i(T)/\sqrt{\mu_i}]$) necessarily is treated as a constant. In this respect, it should be noted that from the so-called harpoon or curve-crossing model as originally proposed by Asscher *et al.* [35] and further developed by Paul *et al.* [32] at elevated temperatures above about 1000 K the NO A-state quenching cross sections of the major combustion species like H₂O (24 Å²), O₂ (26 Å²) and CO₂ (56 Å²) are found to be independent of the temperature indeed. The A-state cross sections of NO in collision with N₂ and CO increase with temperature to values of about 1 Å² and 10 Å² around 2000 K, respectively. However, note that even if relevant data on the corresponding D-state cross sections were available, the unknown gas composition at the crank angles of interest to this study still would necessitate the treatment of the sum in eq. (5.1) as a constant. Finally, $g(\phi_{\text{NO}};\phi_{\text{las}})$ represents the spectral overlap of the laser line and the NO absorption line and, since the pressure terms cancel in this formulation (the amount of NO being expressed as a mole fraction), this also is the only pressure dependent term in the equation.

At resonant excitation the overlap integral is given by

$$g = \int_{-\infty}^{+\infty} \phi_{\text{NO}}(v, v_0, \Delta v_{\text{NO}}) \phi_{\text{las}}(v, v_0, \Delta v_{\text{las}}) dv \quad (5.2)$$

where v_0 is the central frequency and Δv is the spectral FWHM (cm⁻¹) of both the laser radiation and the NO transition. At higher pressures collision-induced broadening of the absorption lines generally is stronger than the Doppler broadening resulting in Lorentzian lineshapes, whereas at lower pressures the lineshape is best described by a Voigt profile (i.e., a convolution of Lorentzian and Gaussian lineshapes). Because even at atmospheric pressure the observed NO absorption lines are much broader (typically 2.6 cm⁻¹ FWHM, see next section) than the laser linewidth (about 0.7 cm⁻¹ FWHM [45]) the laser lineshape is ignored and the value of the overlap integral is taken to be inversely proportional to the absorption linewidth. As data on the pressure broadening of NO D-state lines are not yet to be found in literature, the collision-induced broadening of the absorption lines is assumed to be proportional to the pressure. Consequently, in this work the value of $g(\phi_{\text{NO}};\phi_{\text{las}})$ is assumed to be inversely proportional to the pressure. In the last chapter of this thesis these assumptions are verified for both NO-N₂ and NO-air mixtures using narrow-band fluorescence detection at 208 nm (as being the central wavelength of the interference filter involved in the engine experiments). Finally, it needs mentioning here

⁴ The magnitude and the temperature dependence of the thermally averaged cross sections $\sigma_i(T)$ is perturbing species specific and given by: $\langle v\sigma_i(v) \rangle / \langle v \rangle$. Here $\sigma_i(v)$ represents the relative velocity dependent cross section as found by integrating the quenching probability over the collision impact parameter. The thermal average is taken to be over a Boltzmann distribution of collision velocities v [32].

that in their validation of this A-state fluorescence model for pressures up to 1 MPa, Battles *et al.* [46] find that the applicability of the model is not restricted to well-isolated (NO) absorption lines. However, interference from other species (either in absorption or emission or both) might be difficult to account for and because of this coinciding resonances should be avoided.

Referring to a previous publication [13], an estimate of the local in-cylinder intensity I of the laser light sheet at the selected crank angles and engine loads may be obtained from images of the Mie-scattered laser intensity in the running engine. By extrapolating the experimentally observed decay per unit distance along the propagation direction a dimensionless correction term τ (accounting for the intensity loss before the imaged area is reached) is introduced in the model. Finally, in order to account for the effect of the expansion on the density of the NO molecules the overall 2D-LIF signal strength contained in the corrected distributions is also multiplied by the corresponding in-cylinder volume V .

Dropping all constants (including A_{21} and $\sum_i[\chi_i\sigma_i(T)/\sqrt{\mu_i}]$) and inserting the extra correction terms in eq. (5.1) results in the following proportionality

$$\chi_{\text{NO}} \propto \frac{p \tau V}{\eta_1(T) \sqrt{T}} Y \quad (5.3)$$

by means of which in the next section semi-quantitative concentrations are computed from the image-processed NO distributions.

5.4 Results and discussion

5.4.1 Excitation spectra

Two NO 2D-LIF excitation scans from the running engine at 68° ATDC and BDC are given in figure 5.2 along with a reference excitation scan measured at 600 °C and 0.5 MPa in a cell with 500 ppm NO in N₂ using narrow-band 208 nm fluorescence detection provided by an Optical Multi-channel Analyzer (OMA), as more extensively described in the last chapter of this thesis. These scans result directly from the integrated intensity contained in the imaged NO fluorescence distributions and have not been after-treated in any way. The engine load is 0.4 kW for both engine spectra. The frequency scale is the same for all scans and the indicated line positions are based on calibration data of Versluis *et al.* [44]. The spectra end around 51736.5 cm⁻¹ at one of the spectral regions where the excitation laser intensity is weak due to room temperature absorption by molecular oxygen in the Schumann-Runge band [54]. As for the engine scans, in the low-temperature and atmospheric pressure scan at BDC another region where the same phenomenon occurs is seen to be centred around 51682.6 cm⁻¹. Note that the maximum fluorescence signal from the engine is reduced to about 50% in going from atmospheric pressure (the BDC engine scan) to 0.5 MPa (the 68° ATDC scan). It should be mentioned here that the estimated in-cylinder temperature at 68° ATDC is about 300 °C higher than the BDC temperature of about 570 °C (see also fig. 5.6). On the one hand, a higher temperature leads to overall stronger fluorescence as a result of larger population densities of the probed levels. This probably explains the relatively strong signals at 68°

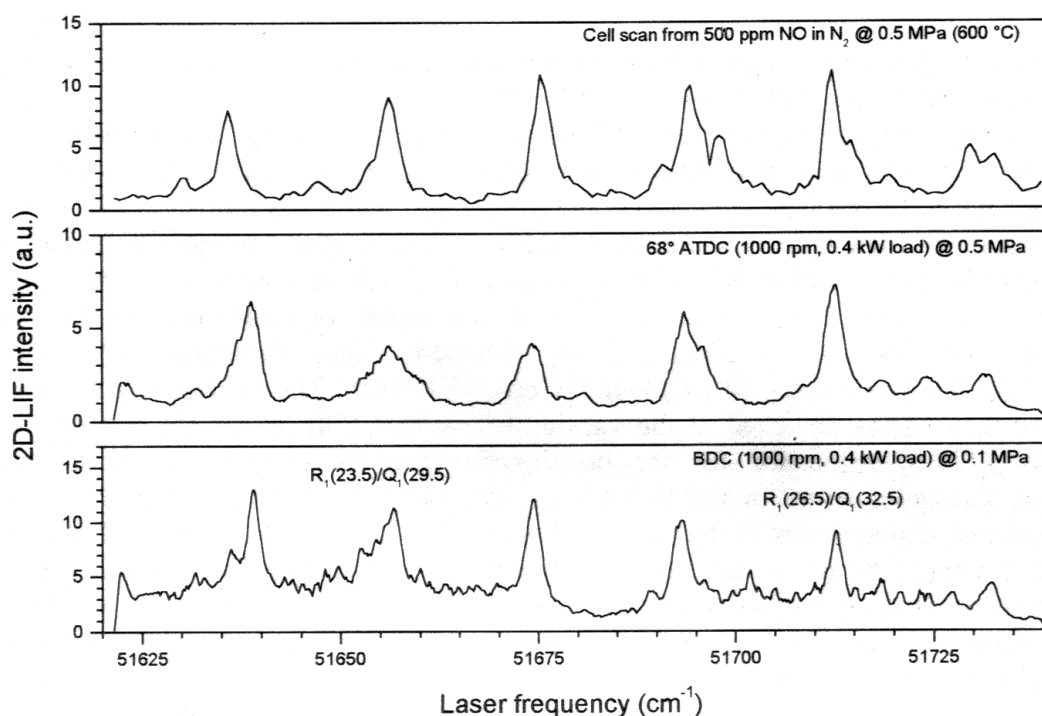


Figure 5.2 *NO excitation scans from the 0.4 kW loaded engine at 68° ATDC and BDC. For linewidth comparison an OMA (reference) excitation scan recorded at 0.5 MPa and 600 °C in a cell from 500 ppm NO in N₂ is given at the top of the figure. The assignments of two relevant resonances are indicated in the bottom figure*

ATDC and 0.5 MPa (i.e., only 50% reduction) as well as the different relative intensities of the lines of the dominant progression resulting from relatively faster growing population densities of the higher rotational sub-states in the ground electronic state. In particular, in the BDC (bottom) scan the $R_1(22.5)/Q_1(28.5)$ resonance is the strongest whereas the $R_1(26.5)/Q_1(32.5)$ resonance evidently is the strongest in the 68° ATDC spectrum. On the other hand, in the presence of O₂ at elevated temperatures there will be increased in-cylinder absorption of the excitation laser intensity as Lee *et al.* [54] find the spectral density of the O₂ absorption lines in the laser tuning range as well as the magnitude of the predicted absorption coefficients $k(O_2)$ to rapidly increase with increasing temperature. This implies that in both engine scans the observed fluorescence is expected to also reflect these temperature and wavelength dependent in-cylinder absorptions of the laser radiation. In this respect, the strong signal from the $R_1(22.5)/Q_1(28.5)$ resonance as observed in the (higher temperature) 68° ATDC spectrum most probably results from (relatively) weak O₂ absorptions for this particular wavelength region around 193.65 nm [54]. The effect of these absorptions is also demonstrated by comparing the weak $R_2(27.5)$ resonance around 51697 cm⁻¹ (at the high frequency side of the $R_1(25.5)/Q_1(31.5)$ resonance) in the engine scans to the much stronger signal observed in the (top) cell scan (i.e., without O₂ being present). It should be mentioned that both 600 °C spectra at the top and the bottom of this figure also display a number of isolated $B^2\Pi(v'=7) \leftarrow X^2\Pi(v''=0)$ features around 51650 cm⁻¹ ($P_1(30.5)$), 51689 cm⁻¹ ($P_2(27.5)$) and 51727 cm⁻¹ ($P_2(26.5)$), respectively. It follows that the apparent lack of these features in the 68° ATDC scan most probably arises from

the higher temperature as well. In retrospect, the latter two B–X resonances are also observed in the BDC excitation scans presented in a previous publication [9].

In both engine scans the lines of the coinciding R_1/Q_1 progressions clearly dominate; however, according to the calibration data of Versluis *et al.* [44] they also coincide with resonances of other progressions which complicate the accurate determination of linewidths (and frequency shifts for that matter). In view of the relatively small contribution expected from the overlapping $P_1(39.5)$ resonance [44], the linewidth of the $R_1(26.5)/Q_1(32.5)$ resonance seems to be best suited for evaluation. At atmospheric pressure (BDC) this line is about 2.6 cm^{-1} (FWHM) wide, whereas at 0.5 MPa (68° ATDC) the line has broadened to about 3.2 cm^{-1} (FWHM). The results of a study of the dispersed LIF signal observed at the various resonances [58] led to the selection of the $R_1(23.5)/Q_1(29.5)$ resonance for the imaging experiments in [13] and in this work; however, the applicability of the $R_1(26.5)/Q_1(32.5)$ resonance (as used in [9]) at higher pressures and temperatures is demonstrated once more in the scan at 68° ATDC. In this context, it should be noted that both NO resonances fall in spectral regions of little O_2 absorption at elevated temperatures [54]. As a result, at narrow bandwidth excitation of these resonances the little background O_2 fluorescence may safely be neglected [43] as, more recently, demonstrated in a 2-stroke diesel engine as well [59]. Finally, from an inspection of the top two scans the linewidths of most resonances in the engine scan are somewhat larger than the corresponding linewidths observed in the (lower temperature) cell scan. This may be explained by the presence of other colliding species in the engine (e.g. O_2 , H_2O and CO_2) having larger NO quenching cross sections than N_2 [32,35]. On the other hand, the relatively small discrepancies between the linewidths as observed at the same pressure in the engine and in the cell apparently suggest about similar gas compositions⁵ in both experiments. This is confirmed by the remark of Heywood [60] in his textbook on internal combustion engines, that at moderate engine loads the exhaust gas composition of diesel engines differs not much from that of air (80% N_2 , 20% O_2). Note that on the basis of a larger set of data this topic will also be discussed in the last chapter of this thesis.

5.4.2 In-cylinder NO distributions

The NO fluorescence distributions in this work are measured twice at seven selected crank angles during the expansion stroke: 68° , 81° , 93° , 105° , 120° , 135° ATDC and BDC as a function of the engine load: 0 kW, 0.4 kW and 0.8 kW. In figure 5.3 the pixel-averaged results of the image-processing corrections at 68° , 93° , 120° ATDC and

⁵ From eq. (5.1) the effective cross section for collisional quenching of NO in a given sample gas composition as defined by $\sum_i [\chi_i \sigma_i(T) / \sqrt{\mu_i}]$ can be shown to be proportional to $[I \chi_{NO} \eta_1(T) \sqrt{T}] / Y \gamma_{NO}$, where γ_{NO} represents the NO absorption linewidth (see section 6.3 of this thesis). The evaluation of the latter expression for the $R_1(26.5)/Q_1(32.5)$ resonance in both 0.5 MPa spectra (using data from this work and some results from chapter 6 as well) gives an about 12.4 times larger effective cross section of the in-cylinder gas than that for collisions with N_2 . To put this into perspective, in chapter 6 a similar evaluation of spectra recorded with narrow bandwidth fluorescence detection leads to an about 6.1 times larger effective NO quenching cross section of air when compared to that of N_2 . It follows that the effective NO D-state quenching cross section of the in-cylinder gas roughly is about 2 times that of air.

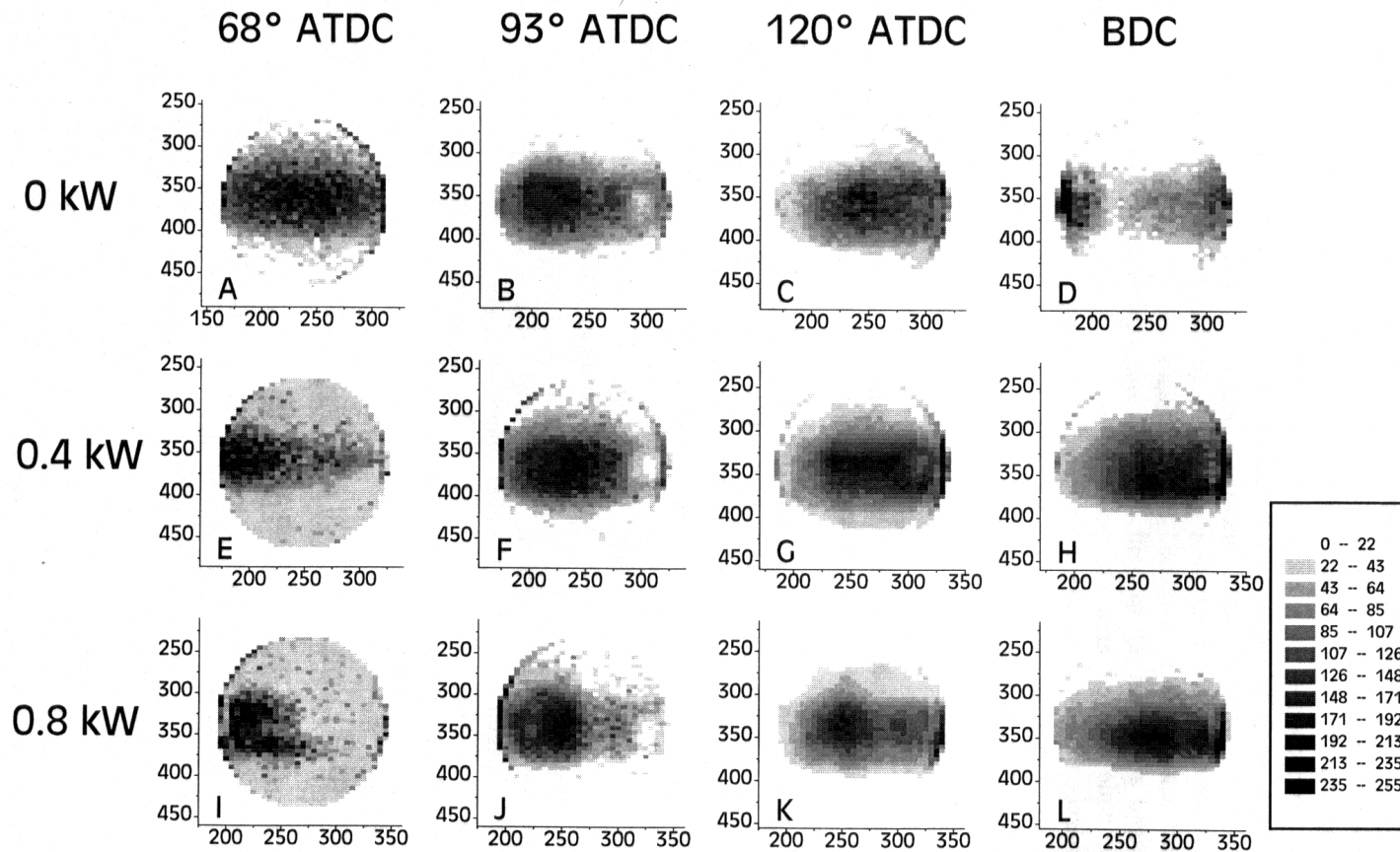


Figure 5.3 Pixel-averaged NO distributions (distribution B is measured only once) at 4 selected crank angles and 3 selected loads after the correction for window pollution and the in-cylinder attenuation of the laser intensity. The pixel-coordinates are indicated on the axes. All distributions are differently scaled as to show maximum detail

BDC at the selected loads of the engine are depicted. The one distribution that actually is measured only once is the distribution at 93° and no load. Due to internal mappings in the correction procedure the unity aspect ratio of the initially imaged distributions is not retained and as a result the spatial resolution along the horizontal and the vertical axes are about $250\ \mu\text{m}$ and $190\ \mu\text{m}$, respectively. Note that in order to reveal maximum detail, the presented distributions are differently scaled and referring to the more extensive discussion of the consequences of these dynamic scalings in [13], it needs mentioning here that no quantitative conclusions may be drawn from the direct comparison of the local intensities (or the pixel-averaged intensity contained within a specific region of interest for that matter) as observed in a given pair of distributions without properly accounting for all scale factors involved. In the images the $2.5\ \text{cm}$ wide laser sheet traverses the imaged area from left to right. The spurious signals at the circumference of the about $5\ \text{cm}$ wide imaged area are produced by the image-processing correction software as a consequence of a number of internal coordinate transformations to ensure maximum spatial overlap of all input images involved. The low intensity spots at the right hand side of the distributions B-F-J are due to strong reflections of the laser light-sheet at the inner surface of the laser exit window causing the image-processing correction procedure to locally produce erroneously weaker signals [13]. These strong reflections most probably are due to a relatively high laser beam intensity at the exit window. Presently, the question as to why the gas mixture apparently becomes optically thinner at this specific point of the cycle remains unanswered in the absence of experimental data on the complicated in-cylinder flows.

At each load (i.e., in each row) a clear shift in the signal from the left hand side to the right hand side of the imaged area is observed as the expansion progresses. On the one hand, this shift might result from the turbulent post-combustion flow patterns leading to inhomogeneous NO distributions. However, in view of the previous results reported in [13], this is not very likely to be the case. On the other hand, this shift may also be explained by the effects of in-cylinder temperature gradients on the Boltzmann distributions. The positions of the valves in the cylinder head just above the imaged area may give rise to considerable temperature gradients as a consequence of the different temperatures of the gas flows they control. The exhaust valve is situated just above the left hand side of the imaged area and its higher operating temperature might explain the stronger signals at this side at earlier times in the expansion. Typical exhaust gas temperatures measured approximately $5\ \text{cm}$ away from this valve are $250\ ^\circ\text{C}$ and $400\ ^\circ\text{C}$ at zero load and maximum load, respectively. Bearing in mind that the valve already opens at $157^\circ\ \text{ATDC}$, the weaker signals at the left hand side of the corrected distributions at BDC (D-H-L) might very well result from cooling of NO molecules below the open exhaust valve.

To illustrate the sensitivity of the 2D-LIF signal for (in-cylinder) temperature gradients, a measure for this sensitivity is calculated using data from [57] and Boltzmann statistics on the spin-rotation split electronic ground state of NO. In figure 5.4 the absolute values of the normalized differential population number density: $|dN(T)/dT| \cdot N(T)^{-1}$ are plotted as a function of the temperature for a given rotational level ($J''=23.5$) in the three lowest vibrational states of the ${}^2\Pi_{1/2}$ ground state probed by excitation at $226\ \text{nm}$ ($v''=0$), $193\ \text{nm}$ ($v''=1$) and $248\ \text{nm}$ ($v''=2$), respectively. Clearly, the LIF signal from excitation of NO in $v''=0$ is the least sensitive to temperature gradients within the plotted temperature range. However, for temperatures above $1200\ \text{K}$

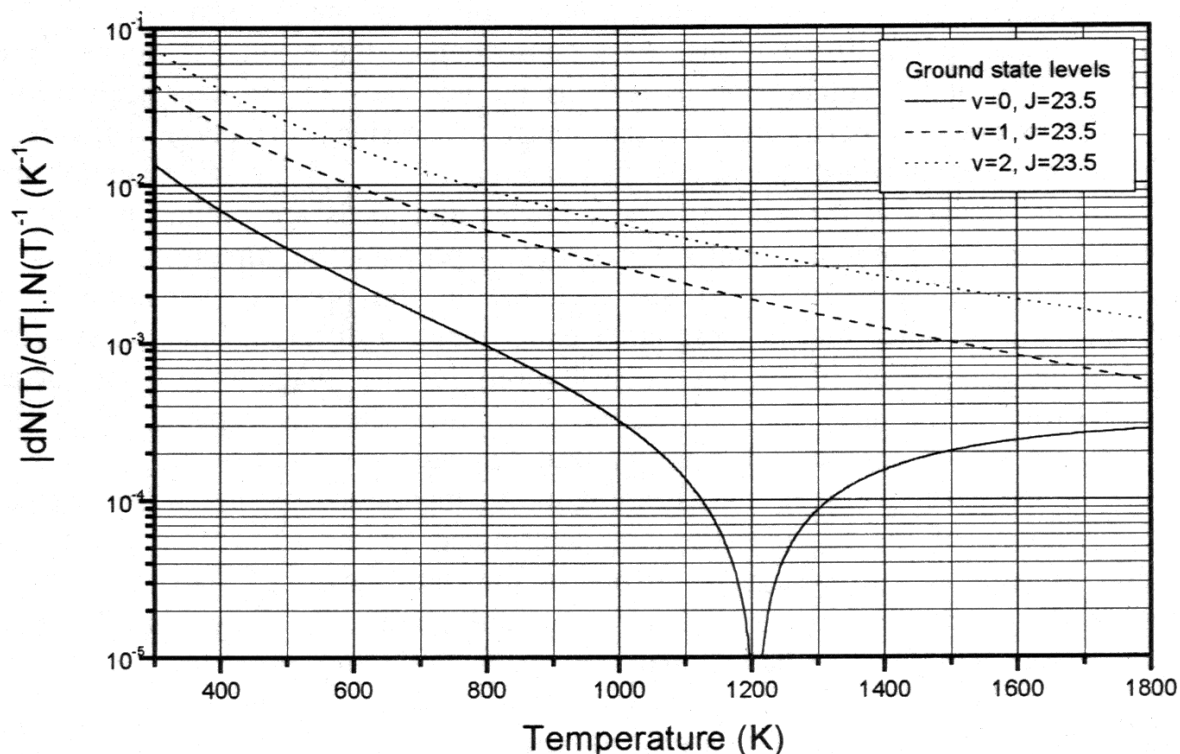


Figure 5.4 Calculated normalized differential fractional population number density as a function of the gas temperature for the $J''=23.5$ rotational state in the three lowest vibrational levels of the $X^2\Pi_{1/2}$ ground state of NO

the fractional population density of the $v''=0$ level decreases and as a result $dN(T)/dT.N(T)^{-1}$ changes sign. As the temperature increases the fluorescence from excitation of NO in $v''=1$ becomes less sensitive for temperature variations as well. Nevertheless, the value of 0.0033 K^{-1} at 1000 K indicates that the LIF signal strength at 950 K would increase by a third if the gas temperature were to be increased by 100 K to 1050 K. Presently, the gas flows during the expansion and the resulting in-cylinder temperature distributions are not known. However, by considering that the estimated overall engine temperature ranges from 700 K to about 1500 K and by assuming a more or less homogeneous distribution of NO molecules, the non-uniformities in the distributions of fig. 5.3 might very well result from similar temperature-induced population differences of the probed ground state as given by the above example. Because of this lack of data on the in-cylinder temperature distributions, the pixel-averaged 2D-LIF signal strength contained in the image-processed distributions is used in the (later) evaluation of eq. (5.3) instead.

In a previous publication [13] the reliability of the image-processing correction procedure is extensively tested in the idling engine with opposite propagation directions of the laser light-sheet. Both the reproducibility of the combustion and the experimental accuracy may be assessed by evaluating the normalized standard deviations of the mean pixel value (i.e., $\sigma(s)/s$, with $\sigma(s)=\sqrt{(\sum_{x,y}[S(x,y)-s]^2/n)}$, $s=\sum_{x,y}[S(x,y)]/n$ and $S(x,y)$ and n representing the pixel value at location (x,y) and the total number of pixels making up the image, respectively) for image ratios of given pairs of corrected distributions obtained

from different sessions with similar engine conditions. Irrespective of the dynamic scaling of the input images, the normalized standard deviation of an image ratio only equals zero in case of identical spatial distributions. As a consequence, the evaluated values represent the reproducibility of the combustion as well as the accuracy of the data acquisition and all pixel-wise operations performed by the image-processing correction software. The computed normalized standard deviations encountered in the 2.5 cm wide central area of the ratios of the images at the selected crank angles and loads are plotted in figure 5.5. For completeness the previous results for opposite propagation directions of the laser light-sheet in the idling engine [13] are included in the present evaluation as well, although it should be noted that in these latter experiments a different imaging system was employed in the acquisition of the input distributions for the image-processing correction procedure. From the figure, the image-processing procedure is capable of producing results from the loaded engine with a normalized standard deviation of the image ratio of about 40% of the pixel-averaged signal strength. As mentioned before, these normalized standard deviations of the image ratios are determined by the (ir)reproducibility of the combustion as well as any systematic errors in the data handling. Assuming the latter systematic errors to be the same for all selected crank angles, it follows that the resulting systematic error actually is smaller than the 40% minimum observed in the figure. Nevertheless, in the following the systematic error is taken to be 40% just to be on the safe side of this. Consequently, the largest values of the normalized standard deviation as observed in the ratio of the images from the idling engine most probably are indicative for a less reproducible character of the combustion in these circumstances.

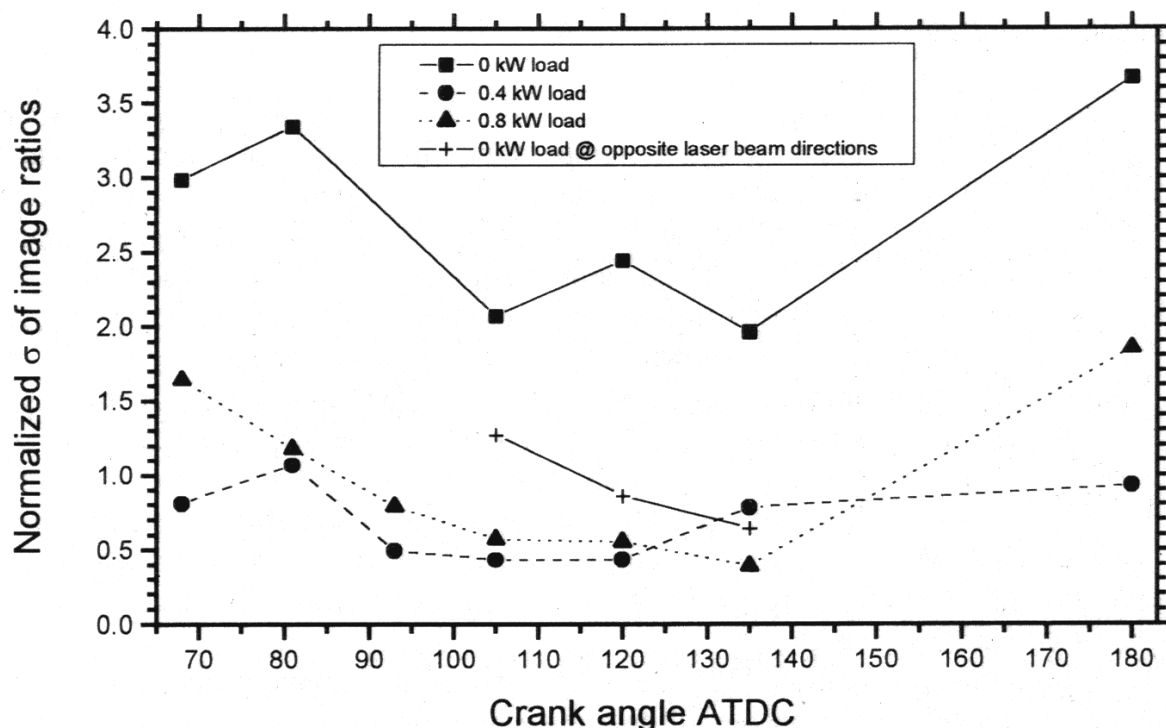


Figure 5.5 Normalized standard deviations of the mean pixel value contained in the ratio of the corrected images, plotted for the selected crank angles as a function of the engine load. The results from a previous experiment in the idling engine in which the propagation direction of the laser light-sheet was reversed are also shown

5.4.3 NO density versus crank angle

Figure 5.6 provides an overview of the relevant data with respect to the application of the model described in the previous section. The top two plots depict the in-cylinder volume and the pressure as a function of the engine load at the selected crank angles, respectively. The following plot shows the in-cylinder temperature for the selected engine loads as estimated by the application of Carnot-cycle thermodynamics to the measured exhaust gas temperatures. As for the optically accessible part of the expansion stroke pertinent to this work, usually two Carnot-cycle stages are distinguished: an adiabatic expansion followed by a pressure drop as soon as the exhaust valve opens (157° ATDC). By applying the ideal gas law, the overall in-cylinder gas temperature before the pressure drop may be reconstructed from the measured exhaust gas temperature and the in-cylinder pressure, whereas for crank angles smaller than 157° ATDC the ideal gas law may be combined with the adiabatic law in order to describe the overall gas temperature in terms of the in-cylinder volume V . The fractional population density in the probed state $\eta_1(T)$ is calculated from Boltzmann statistics and the correction factors (equalling the inverted normalized population densities) are given in the fourth plot. Finally, for each selected engine load the averaged correction factors τ (accounting for the decay of the in-cylinder laser intensity over the first part of the path outside the imaged region as obtained by extrapolating the exponential decay of the Mie-scattered laser intensity; see section 5.3) are given in the bottom plot of the figure. On the basis of the evaluated values of τ at BDC in the quiescent engine and the measured transmissions of the laser entrance and exit windows, the transmission of the laser radiation is found to be about 2.6% which is in good agreement with the directly measured transmission at these operating conditions of about 2%. However, at higher pressures the applied correction factors τ may be systematically underestimated to a presently unknown extent since the directly measured transmission tends to decrease more rapidly with decreasing crank angle than the transmission calculated from the intensity decays observed in the images. Furthermore, at increasing in-cylinder pressures the Mie-scattered laser intensity decays to levels below the detection limit of the imaging system over ever shorter distances. This complicates the accurate evaluation of the correction factors τ ; however, in future experiments the accuracy of this correction may be easily improved by zooming in on the imaged area (i.e., by enlarging the magnification) or by using more powerful lasers. Finally, by taking into account the various dynamic scalings performed by the image-processing correction procedure, the mean pixel value contained in the corrected distributions serves as a measure for the total fluorescence yield Y in the current modelling.

The averaged signal strengths produced by the image-processing procedure and the subsequent numerical corrections are plotted versus the crank angle for the selected loads in figure 5.7 where the 40% systematic error is only indicated for the series at 0.4 kW engine load. In spite of the scatter a steadily decaying signal at increasing crank angles is clearly recognized irrespective of the engine load. Although in this particular engine the combustion itself is not accessible for 2D-LIF measurements, the observed differences in behaviour of the NO density curves at earlier times in the expansion stroke are strong indications that the in-cylinder NO concentration largely depends on the actual engine operating conditions. With respect to these observed decays of the NO density, it should be noted that similar decays resulting from the oxidation of NO are also reported by Pitsch *et al.* [61] in their evaluation at various EGR rates of a model for the formation of

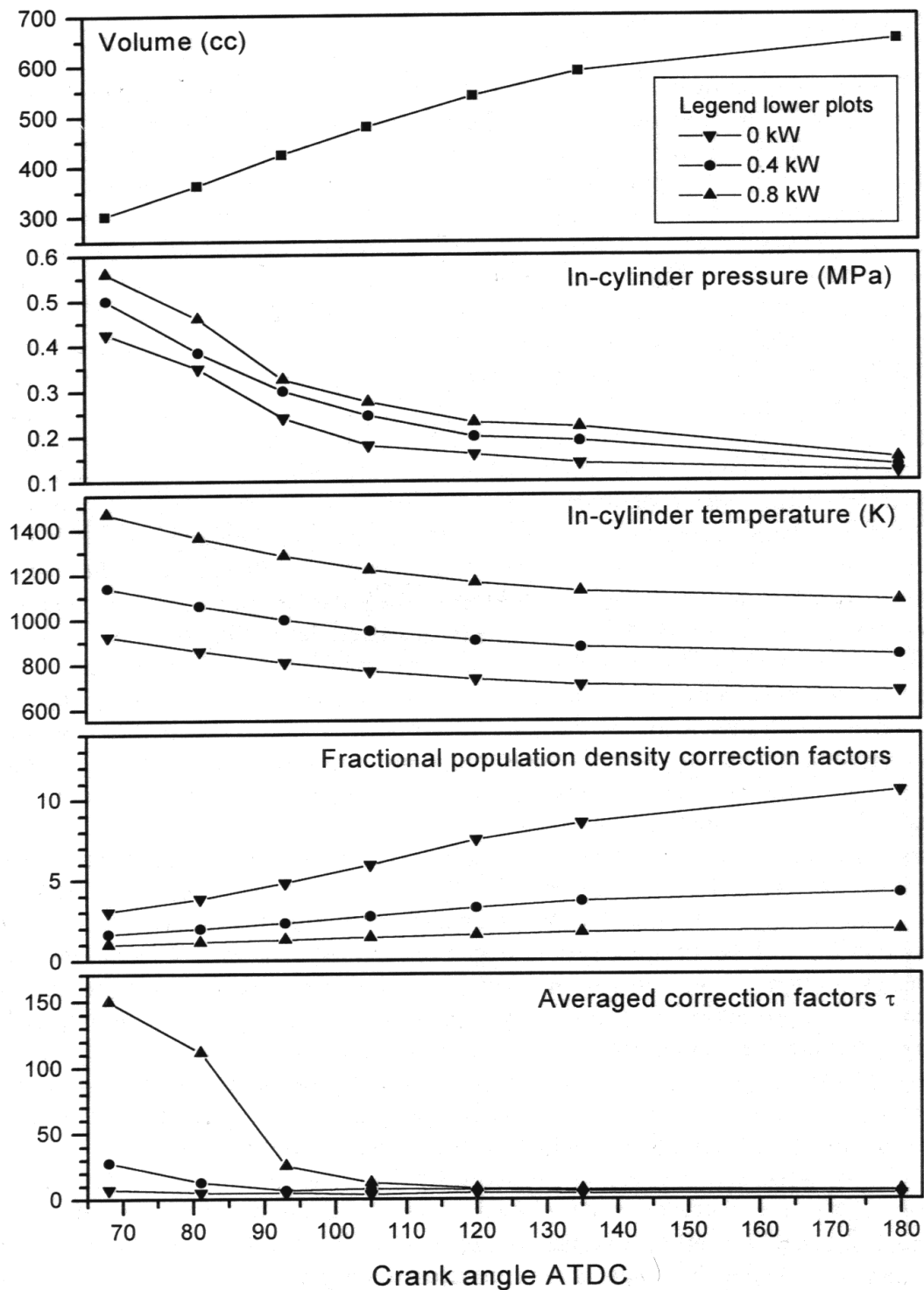


Figure 5.6 From top to bottom, respectively, the volume, the measured in-cylinder pressure, the estimated overall gas temperature, the fractional population density correction factors and the averaged correction factors τ (accounting for the in-cylinder laser intensity decay over the first part of the path before the imaged area is reached) plotted versus the crank angle as a function of the engine load

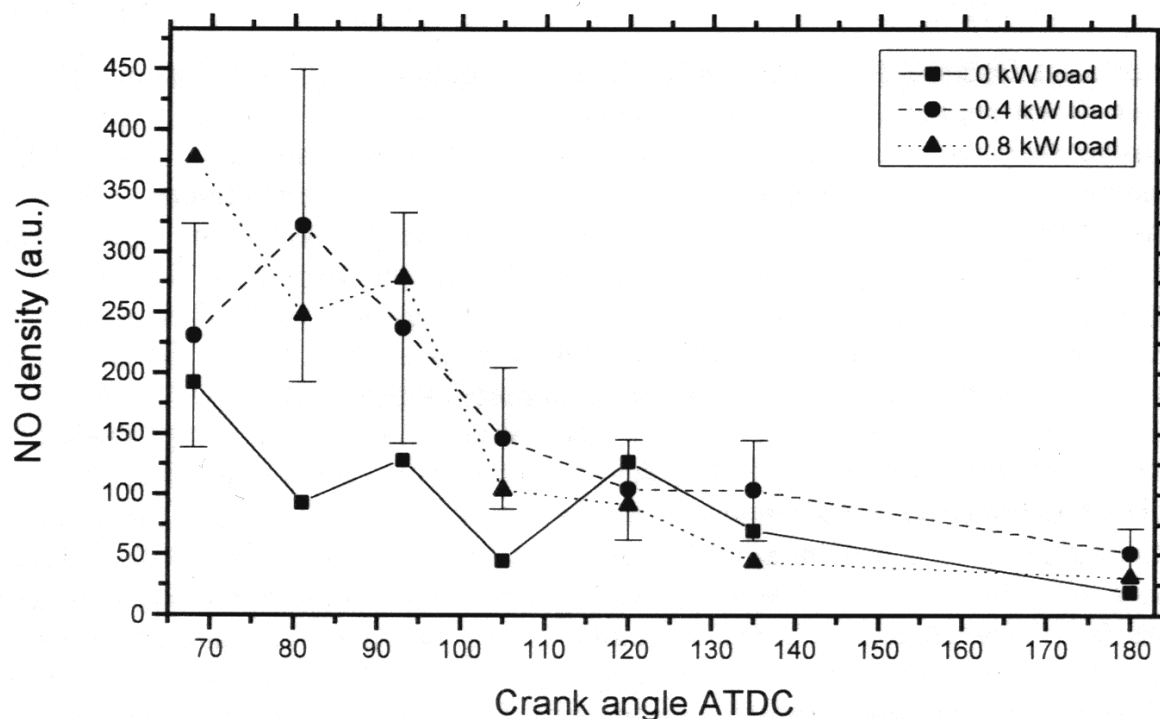


Figure 5.7 Corrected signal strength as a function of the engine load versus the selected crank angles: 68°, 81°, 93°, 105°, 120°, 135° and BDC, respectively. All values (except at 93° ATDC and 0 kW load) are averaged results. For clarity, the 40% error bars are only indicated for the series at 0.4 kW load

pollutants in diesel engines. In their DI test engine they observe that the decay of the NO density strongly varies with the selected EGR rates. Similar decays for DI and IDI diesel engines are also reported in the textbook by Heywood [60], where the in-cylinder NO concentration is determined as a function of the crank angle by means of various rapid-acting gas sampling valves. The observed decay rates are found to be very sensitive to the injection timing as well as to the engine loads and the amount of fuel injected (i.e., the equivalence ratio). However, these results are in contrast with the findings of Donahue *et al.* [15] in their gas sampling experiments in a turbo-charged diesel engine as these authors observe a nearly constant NO density for crank angles beyond 23° ATDC. This most probably indicates once more that the observed decays may largely vary with the actual engine operating conditions indeed. Finally, within the present experimental accuracy, the observed BDC NO densities at the various engine loads seem to be in reasonable agreement with the recorded exhaust gas NO_x levels (the NO_x measuring device primarily being sensitive to the electrochemistry of NO as so specified by its manufacturer) varying from 2450 ppm for the idling engine to about 3800 ppm on average for either engine load (i.e., 3700 ppm and 3900 ppm at 0.4 kW and 0.8 kW load, respectively).

5.5 Summary and conclusions

The imaging of laser-induced NO fluorescence distributions in a steadily running diesel fuel driven diesel engine at selected crank angles and loads forms a powerful quantitative, non-intrusive diagnostic tool, provided the initially measured distributions are corrected for window fouling, in-cylinder laser extinction, overall temperature effects and collisional quenching, respectively. If these corrections are performed the signal strength tends to decrease with increasing crank angle during the expansion stroke. This is believed to be indicative for the oxidation of NO molecules. At earlier times in the expansion the corrected signals from the loaded engine turn out to be significantly stronger than the signals found in the quiescent engine, as expected.

In both engine excitation spectra the lines of the coinciding D–X R₁/Q₁ progressions dominate and this indicates that, in spite of the temperature and wavelength dependent in-cylinder O₂ absorptions of the excitation laser radiation, for (moderate) engine pressures up to 0.5 MPa any of these resonances may be used for the imaging of in-cylinder NO distributions. Confirmation for the similar linewidths observed in the presented 0.5 MPa excitation scans is found in the literature on internal combustion engines.

The NO fluorescence model accounting for the overall effects of pressure and temperature on the observed LIF signals provides a method to correlate the latter with tail-pipe concentrations within reasonable accuracy. Although the key problems in the current modelling seem to be posed by the lack of data on the in-cylinder temperature distributions and the interference from other species, for obvious reasons, the extent as to which the accuracy of the current (one-dimensional) fluorescence model may be further improved by the inclusions of ground state RET rates, gas composition data and relevant D-state quenching cross sections, respectively, remains to be investigated in future experiments.

Chapter 6

Laser-Induced Fluorescence Yield from $D^2\Sigma^+$ NO in N_2 and Air at Elevated Temperatures and Pressures

Abstract

Laser-induced fluorescence from NO in N_2 and air is studied at 193 nm excitation in a closed cell at pressures ranging from 0.1 MPa to 5 MPa and at temperatures ranging from 600 °C to 1000 °C. Excitation scans recorded with a broadband imaging setup are compared to the results obtained in case of narrow band fluorescence detection as provided by an OMA system. From the recorded $D^2\Sigma^+(v'=0) \leftarrow X^2\Pi(v''=1)$ excitation scans the fluorescence yield at a dominant rotational resonance of this system is evaluated as a function of the conditions in the cell. Finally, the consistency of a simplified fluorescence model as adapted from high-pressure 226 nm NO combustion studies is tested by comparing the observed effective cross section ratios for the different sample gases to the ratios derived from data found in the literature.

6.1 Introduction

Over the last two decades the application of non-intrusive laser-based diagnostics like laser-induced fluorescence imaging has proved to be of great value in combustion research. However, due to usually unknown collisional quenching rates the quantitative interpretation of the LIF signals is seriously hampered. The collisional quenching of the fluorescence at a transition from an excited state (2) to a rovibrational state (1) in the ground electronic state causes a decrease of the quantum yield by a factor $A_{21}/(A_{21}+Q_2)$, called the Stern-Vollmer factor, with A_{21} as the Einstein coefficient for spontaneous emission and Q_2 as the collisional quenching rate. At atmospheric and higher pressures Q_2 generally is very much larger than A_{21} and the Stern-Vollmer ratio effectively reduces to A_{21}/Q_2 . Whereas the Stern-Vollmer factors for the NO fluorescence following 226 nm excitation of the $A^2\Sigma^+(v'=0) \leftarrow X^2\Pi(v''=0)$ band have been extensively studied [32,38,42,46-49], the fluorescence following excitation in the $D^2\Sigma^+(v'=0) \leftarrow X^2\Pi(v''=1)$ system ($\lambda \approx 193$ nm) has to the best of our knowledge only been studied at sub-atmospheric pressures by Asscher *et al.* [35] and Scheingraber *et al.* [36] whereas Wodtke *et al.* [43] studied the $D \rightarrow X$ fluorescence from an atmospheric flame. As for the latter transition, it should be noted that Electronic Energy Transfer (EET) out of the excited $D^2\Sigma^+(v'=0)$ state is an additional fluorescence loss channel as compared to A state excitation. Due to the lack of experimental data on the fluorescence yield of NO $D^2\Sigma^+(v'=0)$ molecules at elevated pressures and temperatures, a quantitative interpretation of the NO laser-induced fluorescence signals acquired under conditions typical for high pressure combustion is still very difficult. For this reason, the fluorescence yield following excitation of one of the strongest rotational resonances around 193 nm is studied in an optically accessible heated high-pressure cell.

At sub-atmospheric pressures Asscher *et al.* [35] measured the fluorescence quenching cross sections for the NO $A^2\Sigma^+(v'=0)$, $C^2\Pi(v'=0)$ and $D^2\Sigma^+(v'=0)$ Rydberg states in the case of various colliding species. The similarity between the energy level diagram of NO and that of alkali metals led these authors to suggest a model for the quenching mechanism of the various colliding species based on ion pair intermediates on crossings between covalent and ionic molecular potential energy curves. Quenching of the $C^2\Pi(v'=0)$ and $D^2\Sigma^+(v'=0)$ fluorescence by O_2 (having a positive electron affinity) was found to proceed about 3 times more efficiently than that of the $A^2\Sigma^+(v'=0)$ state. In comparison to the quenching by O_2 the quenching of the $D^2\Sigma^+(v'=0)$ fluorescence by N_2 (having a negative electron affinity) was observed to be about 10 times less efficient, whereas the quenching of $A^2\Sigma^+(v'=0)$ fluorescence turned out to be negligibly small. The collision-induced coupling of the D and C states is fairly strong according to the observation of Wodtke *et al.* [43], that after selectively exciting ground state molecules to rotational levels of the $D^2\Sigma^+(v'=0)$ state at atmospheric pressure, the $C^2\Pi(v'=0)$ state is populated efficiently enough to produce C \rightarrow X fluorescence about 25-50% as strong as the D \rightarrow X fluorescence. As for the fluorescence from the C state, it should be mentioned that rotational states above $J'=5.5$ in the $C^2\Pi(v'=0)$ state are highly predissociative as a consequence of the crossing of the $C^2\Pi$ state energy curve with the energy curve of the $a^4\Pi_i$ state (see fig. 1.2) [35]. As a consequence, the C \rightarrow X fluorescence yield may be expected to be much less sensitive to the pressure than the induced D \rightarrow X fluorescence.

However, as far as the collisional quenching of $A^2\Sigma^+(v'=0)$ molecules is concerned, the curve crossing model as originally proposed by Asscher *et al.* [35] has in recent years been further developed by Paul *et al.* [32] with an improved treatment of the observed temperature dependence of the cross sections for various collision partners. Thoman *et al.* [38] studied NO- N_2 interactions and also extended the original model in order to account for the observed 1000-fold increase of the $A^2\Sigma^+(v'=0)$ collision cross section in the temperature range from 300 to 4500 K. As the understanding of the quenching mechanisms of $A^2\Sigma^+(v'=0)$ molecules grew to its current state many efforts were directed towards the development of semi-quantitative calibration procedures in combustion diagnostics which properly account for the (colliding species specific) collisional quenching effects on the NO fluorescence yield at 226 nm excitation [47,48,50]. Battles *et al.* [46] formulated and validated such a fluorescence model in terms of known or easily measurable parameters and the data presented in this work are analyzed in a similar manner to produce first order approximations of the effective $D^2\Sigma^+(v'=0)$ collision cross sections in N_2 and air in combustion-like circumstances.

6.2 Experimental

The cross-sectional views of the cylindrical cell ($\phi=22$ cm) are schematically depicted in figure 6.1. The actual measuring volume is heated by a coaxial ring of 10 cm long wires in such a way that full optical access is preserved. A 15 cm long and 2 mm thick quartz cylinder ($\phi=5$ cm) with slots for the laser beam and the fluorescence radiation surrounds both the heating wires and the measurement volume in order to minimize heat loss by convection at higher temperatures. Heat losses by conduction are minimized by filling the cell with thermal isolation material and this leads to an effective gas volume of about 10 litres. The output of a number of strategically placed thermocouples is digitized and

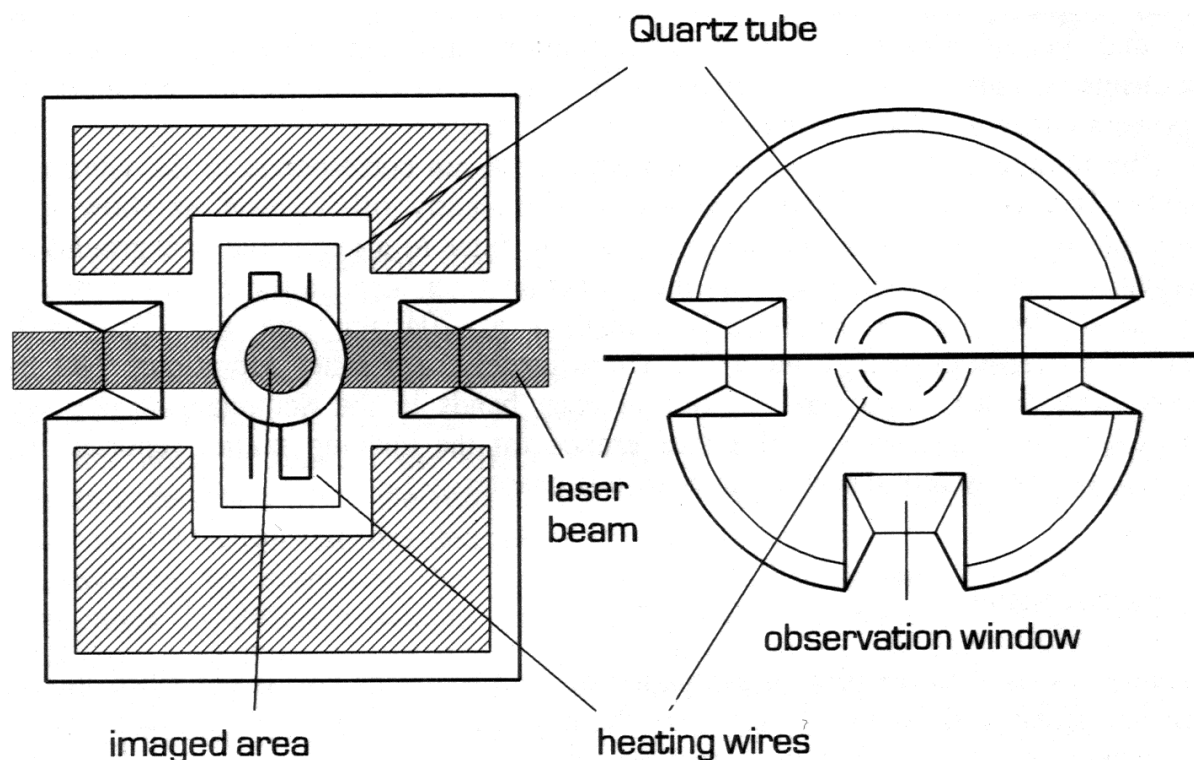


Figure 6.1 *Schematic cross sectional views of the cell along the laser light sheet. The shaded elements represent the thermal isolation material*

monitored on-line on a computer screen. Two of these thermocouples are located just above and below the measurement volume and the averaged read-out is taken to be the gas temperature. The NO concentration is fixed in these experiments to about 500 ppm in N_2 or (dry) air: 80% N_2 / 20% O_2 .

The unfocused output (≈ 100 mJ/pulse, 13 ns) of a tunable ArF excimer laser (Lambda Physik EMG 150 MSCT) is a vertically oriented laser light-sheet (2.5 cm high, 3 mm thick) which traverses the interior of the cell in a horizontal plane through two 2.5 cm thick quartz (Suprasil-I) optical ports. The fluorescence from the 2.5 cm wide imaged area is monitored perpendicularly to the laser light-sheet through the third port using a 13 nm bandwidth reflection filter with about 80% transmission at its centre wavelength of 208 nm and a 50 ns gated intensified CCD-camera (ICCD-576/RB-E, Princeton Instruments). Excitation spectra are obtained by evaluating the total intensity of 10-shots averaged 2D-LIF distributions while the laser frequency is continuously varied over its about 225 cm^{-1} wide tuning range. The resulting frequency resolution is about 0.4 cm^{-1} per (10-shots averaged) datapoint, which is smaller than the estimated laser linewidth of about 0.7 cm^{-1} FWHM [45].

Later experiments were performed using another tunable ArF excimer laser (Lambda Physik Compex 350T) operated in about the same power range as the other laser, and a Chromex imaging spectrograph (Chromspec 250i) with a $250\text{ }\mu\text{m}$ slit in combination with an ICCD-camera monitoring the dispersed NO fluorescence around 208 ± 1 nm. Since in these Optical Multi-channel Analyzer (OMA) experiments the same measurement and data acquisition techniques are used, the previous remarks on the resulting frequency resolution

of the excitation scans apply here as well. It should also be noted that in the absence of on-line calibration, any non-linearities of the tuning mechanisms or temperature drifts of the laser frequencies during the measurements form additional sources of experimental error.

The monitored fluorescence wavelength of 208 nm corresponds to the vibronic NO transition $D^2\Sigma^+(v'=0) \rightarrow X^2\Pi(v''=3)$ and is sufficiently off-resonant to allow for the suppression of the laser radiation by the reflection filter to a negligible background level. However, it should be mentioned that the reflection filter also transmits NO fluorescence from the $C^2\Pi(v'=0) \rightarrow X^2\Pi(v''=2)$ transition at 204 nm and the $C^2\Pi(v'=0) \rightarrow X^2\Pi(v''=3)$ transition at 211 nm [43]. Unfortunately, the latter vibrational NO bands coincide with higher vibrational O_2 fluorescence bands in the Schumann-Runge system [43,63,64]. The implications of this interference for the imaging studies reported in this thesis will be extensively discussed later in this chapter.

6.3 Data reduction

The model involved in the present evaluation of the LIF yields also is described in section 5.3 of this thesis and for this reason only the essential equations will be given here. The model makes use of the following proportionality

$$Y \propto (k_{12} p \chi_{NO}) g(\phi_{NO}; \phi_{las}) I \frac{A_{21}}{\frac{p}{k_B T} \sum_i \chi_i \sigma_i(T) \sqrt{\frac{8k_B T}{\pi \mu_i}}} \quad (6.1)$$

to express the fluorescence intensity Y at any given resonance in terms of the NO mole fraction χ_{NO} , the pressure p , the temperature T , the absorption line strength k_{12} , the local laser intensity I and the high pressure Stern-Vollmer factor A_{21}/Q_2 where Q_2 is given by the product of the colliding species density, their thermally-averaged collision cross sections for NO quenching and their relative velocities (see also section 5.3). Experimental constants like the collection solid angle and the quantum efficiency of the detection system are dropped. The absorption line strength k_{12} also contains the fractional population density of the probed ground state $\eta_1(T)$ as well as the Franck-Condon and Hönl-London factors of the given (unsaturated) transition. The spectral overlap of the narrow laser line and the pressure-broadened NO absorption lines is accounted for by the overlap integral $g(\phi_{NO}; \phi_{las})$ with ϕ_{NO} and ϕ_{las} as the spectral intensity distribution of the NO absorption line and the laser, respectively. From the same reasoning as given in section 5.3 the value of the overlap integral is taken to be inversely proportional to the absorption linewidth γ_{NO} . With respect to potential interference at elevated pressures from merging (pressure-broadened) adjacent absorption lines, it needs mentioning here that in their validation of the fluorescence model (using narrow bandwidth 226 nm excitation and broad band fluorescence detection) Battles *et al.* [46] concluded that a well isolated absorption line is desirable, however, not essential.

Assuming a constant local laser intensity, it follows that at any given temperature T the fluorescence intensity Y observed from a specific gas sample will be inversely proportional to the NO absorption linewidth. This implies that at any given pressure p one

can express the resulting linewidth in terms of the fluorescence intensity observed at the same pressure and temperature. One may then write

$$\frac{\gamma_{\text{NO}}(p)}{\gamma_{\text{NO}}(p_0)} = \frac{Y(p_0)}{Y(p)} = \frac{1}{Y'(p)} \quad (6.2)$$

with $Y'(p)$ as the normalized fluorescence signal $Y(p)/Y(p_0)$ at pressure p and p_0 representing atmospheric pressure. In the following, the left hand side of eq. (6.2) will be referred to as the effective broadening factor and by its evaluation in the next section the underlying assumption of linear pressure-broadening is tested. Moreover, in order to assess the interference of fluorescence from other species than NO in the previous engine combustion imaging studies, the effective broadening factors evaluated for broadband fluorescence detection using the reflection filter are compared to the factors obtained for narrow band OMA fluorescence detection.

However, by evaluating the fluorescence intensities as recorded from equal NO concentrations in different sample gases at the same pressure and temperature, the implications of the fluorescence model may be verified in greater detail. From eq. (6.1), while abbreviating the summation in the denominator of eq. (6.1) (i.e., $\sum_i [\chi_i \sigma_i(T) / \sqrt{\mu_i}]$) to $\sigma_{\text{eff},1}$ or $\sigma_{\text{eff},2}$ for sample gas 1 and 2, respectively, one finds that for any given pressure p and temperature T the effective cross section ratio is given by

$$\frac{\sigma_{\text{eff},1}}{\sigma_{\text{eff},2}} = \frac{Y_2(p)}{Y_1(p)} \frac{\gamma_{\text{NO},2}(p)}{\gamma_{\text{NO},1}(p)} = \frac{Y_2(p_0)}{Y_1(p_0)} \frac{\gamma_{\text{NO},2}(p_0)}{\gamma_{\text{NO},1}(p_0)} \quad (6.3)$$

where the last factor at the right hand side is a constant near unity. The results of the evaluation of the atmospheric pressure fluorescence intensity ratio $Y_2(p_0)/Y_1(p_0)$ for the respective dominant resonances of interest are reported in the next section.

6.4 Results and discussions

From the large number of excitation scans recorded in these experiments a selection is shown in the next figures. A remark concerning the horizontal scale of the figures should be made here. In order to account for the absence of data on the absolute laser frequencies during the measurements, the laser frequencies at the beginnings and the ends of the spectra serve as a reference. For convenience, on the basis of the calibration data of Versluis *et al.* [44] the absolute positions of the dominant rotational R₁/Q₁ NO D–X resonances are indicated by the ticks above the bottom horizontal axis of the figures (for clarity the indicated J'' -values refer to the resonances of the R₁ progression only). As expected, at rising pressures the unambiguous identification of the NO resonances becomes very difficult as a result of pressure broadening and decreasing signal levels. When so, another reference is formed by the positions of a number of absorptions of the laser radiation by room temperature O₂ in the 4-0 vibronic band of the B³Σ_u⁻ ← X³Σ_g⁻ Schumann-Runge system [54].

6.4.1 Excitation spectra at atmospheric pressure

Figure 6.2 provides a comparison of the excitation spectra at 600 °C and atmospheric pressure as recorded with the reflection filter from the 500 ppm NO-air mixture in the cell (D) and from the diesel engine pertinent to this thesis (E) to spectra obtained from the cell with the 500 ppm NO-N₂ and NO-air mixtures using narrow band 208 nm OMA fluorescence detection (A,B). All features of the bottom scan can be assigned to NO D(v'=0) ← X(v''=1) and B(v'=7) ← X(v''=0) rotational resonances [44], the latter features being weaker as a result of smaller Franck-Condon factors. Included in the figure (C) is a simulation of the NO D–X excitation scans at 600 °C as produced by the spectroscopic simulation program LIFBASE [30]. Comparing the simulated spectrum to the bottom scans one may conclude that only the positions of the dominant R₁/Q₁ progression are correctly predicted. However, with regard to the minor D–X features the simulation apparently is deficient. Referring to the discussion of eq. (6.3) in the previous section, the about 5 times weaker peak signals in the OMA scan from the NO-air mixture (B) when compared to the peak signals from the NO-N₂ mixture (A) might indicate that the 20% O₂ in the NO-air mixture leads to an about 5 times larger effective cross section for NO quenching. It should be noted that for a number of relevant resonances these ratios are more extensively verified in section 6.4.3. In this respect, it should also be mentioned that according to various chemical textbooks at atmospheric pressure the oxidation of NO ceases at temperatures around and above 600 °C. From the different number of molecules at both sides of the oxidation reaction one may expect an increase of the oxidation rate at rising pressures; however, experimental data on the oxidation chemistry of NO in the pressure and temperature ranges of interest was not found in the literature.

The cell spectrum recorded through the reflection filter (D) shows some very strong features not observed in the OMA spectrum from the same sample gas (B), of which those around 51702 cm⁻¹, 51745 cm⁻¹ and 51755 cm⁻¹ are the most evident. From the fact that in the NO-air mixture no other sources of fluorescence than NO and O₂ are present, it follows that these features are indicative for interfering O₂ fluorescence within the reflection filter bandwidth. The weak signals at the lower laser frequencies as observed in the spectrum labelled D most probably are due to an initially reduced locking-efficiency of the laser after each refreshment of its gas filling [53]. Note that on the basis of another set of excitation scans this spectrum is discussed in more detail in the next paragraph. Although the atmospheric pressure engine scan has already been discussed in the previous chapter, this spectrum is shown here again for its much less pronounced signal around 51702 cm⁻¹, in particular. On the one hand, this obviously might result from relatively low O₂ concentrations in the engine. Although the similarity with regard to the relative intensity around 51702 cm⁻¹ of the top scan to the oxygen-free bottom OMA scan of this figure seems to confirm this explanation, in view of the oxygen-enriched combustion as pertinent to this thesis, this is not very likely to be the case. On the other hand, in view of the uncertainty with respect to the in-cylinder temperature the weaker signal around 51702 cm⁻¹ from the engine might also result from a higher temperature than estimated (about 570 °C, see chapter 5 of this thesis). This is illustrated by the set of excitation spectra shown in the next figure.

Figure 6.3 shows the temperature effects on the relative intensities at atmospheric pressure as measured through the reflection filter with 500 ppm NO in air at cell

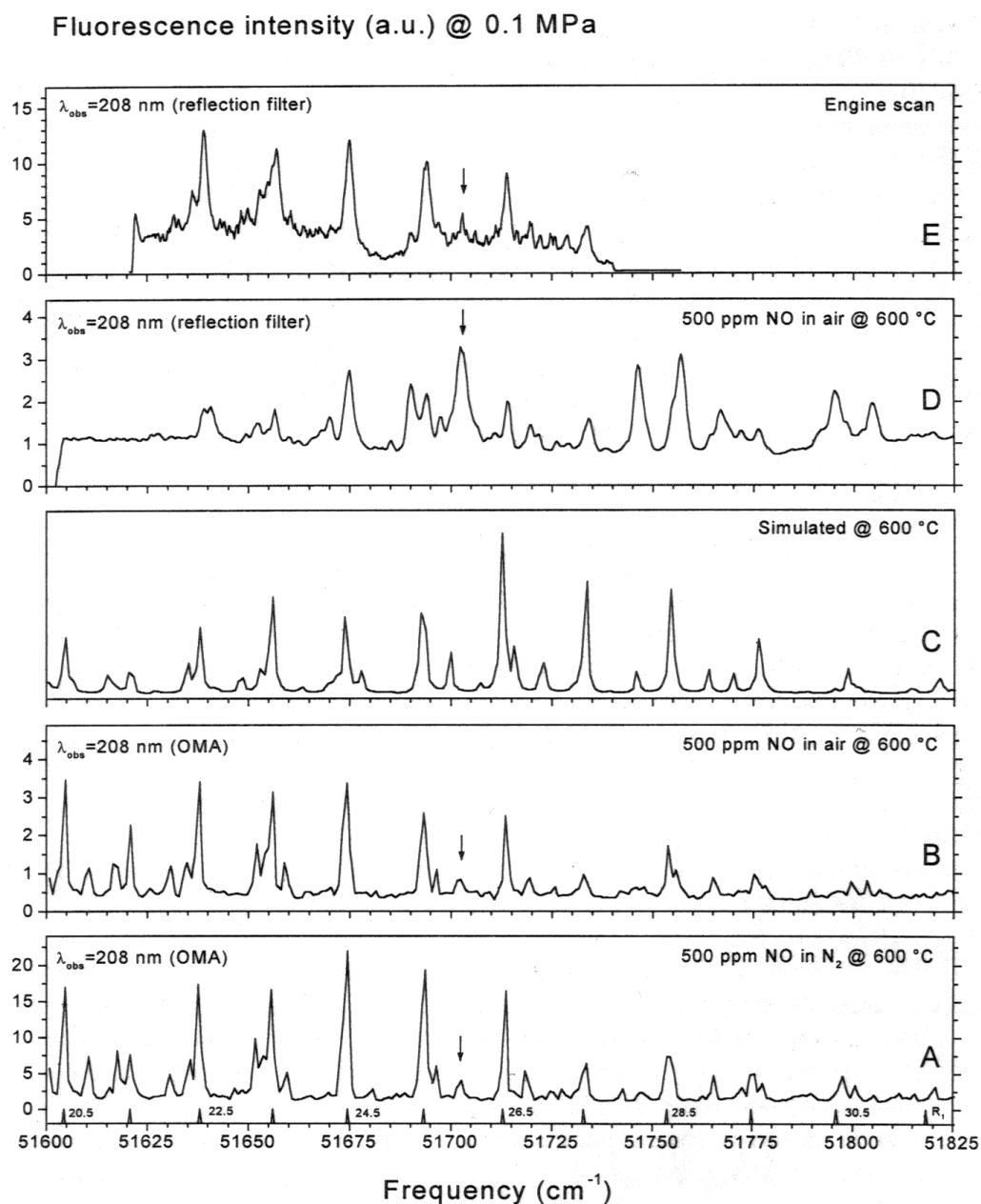


Figure 6.2 Two sets of excitation scans (500 ppm NO in air or N_2) from the cell as measured at atmospheric pressure with the OMA (bottom two scans) and through the reflection filter (top two scans). The top scan was also recorded at atmospheric pressure from the 0.4 kW loaded engine. The rotational resonances of interest in this work are indicated by the ticks above the horizontal scale of the bottom scan. From left to right the progression starts with the $R_1(20.5)/Q_1(26.5)$ resonance and it ends with the $R_1(31.5)/Q_1(37.5)$ resonance. The background in the engine experiments is shown at the end of the top spectrum where the laser beam was blocked. The spectrum in the middle is a simulated NO excitation spectrum. The arrows indicate the NO- O_2 coincidence at 51702 cm^{-1} discussed in the text

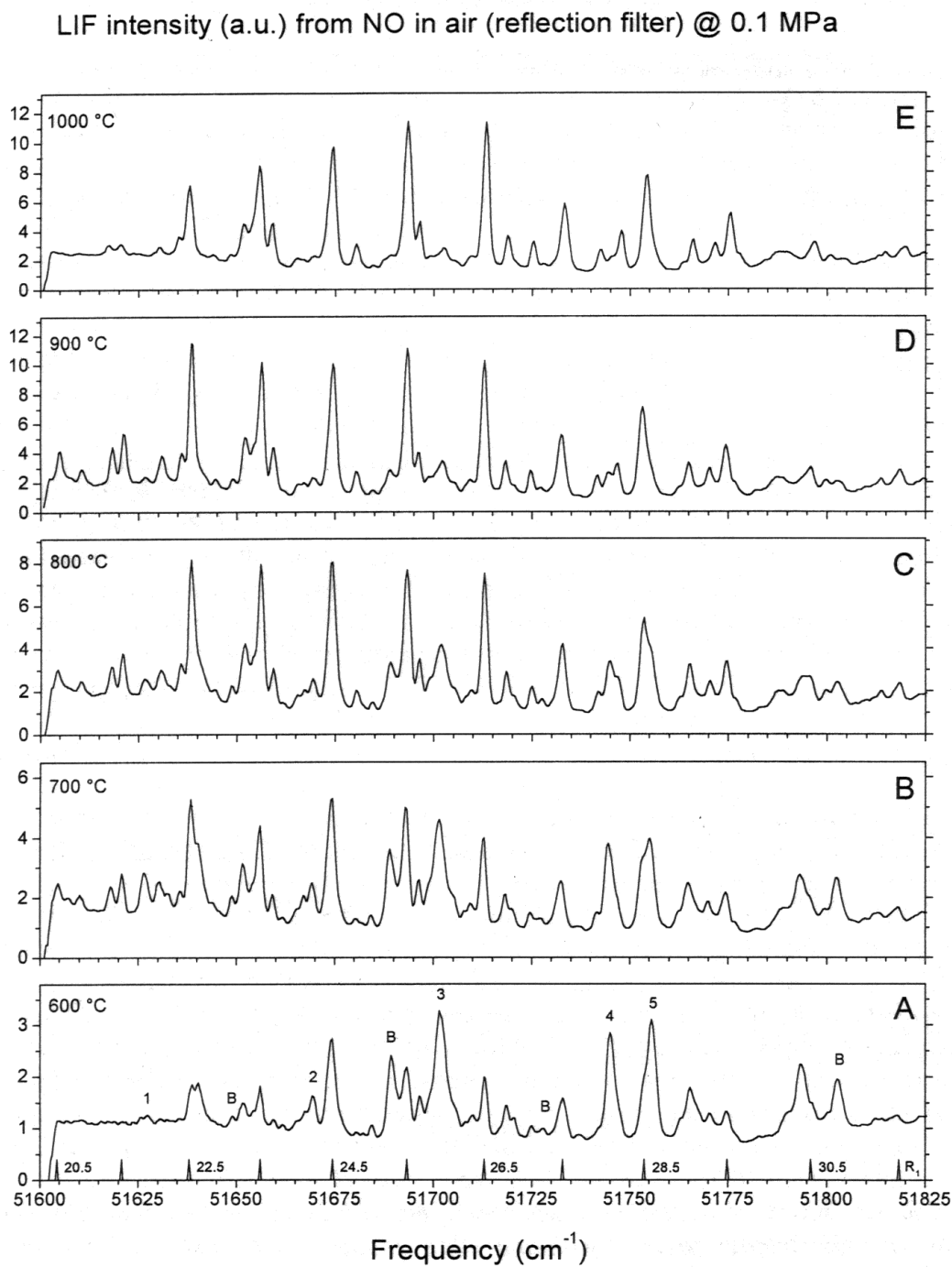


Figure 6.3 Five atmospheric excitation scans (500 ppm NO in air) as observed through the reflection filter at different cell temperatures. The NO $B \rightarrow X$ resonances in the bottom scan are marked B and the numbered peaks indicate the NO- O_2 coincidences discussed in the text: 1= $P_2(36.5)$ - $R(11)(14-3)$, 2= $P_1(37.5)$ - $R(29)(11-2)$, 3= $Q_2(33.5)$ - $P(17)(10-2)$, 4= $Q_2(35.5)$ - $R(3)/P(3)(14-3)$ and 5= $R_1(28.5)/Q_1(34.5)$ - $R(17)(10-2)$

temperatures ranging from 600 °C (bottom scan) to 1000 °C (top scan). The bottom scan of this figure is identical to the scan labelled D in the previous figure and all of its features can be assigned to NO $D(v'=0) \leftarrow X(v''=1)$ and $B(v'=7) \leftarrow X(v''=0)$ rotational resonances [44]. As the temperature rises the signals at the dominant coinciding rotational $D \leftarrow X$ resonances increase as a result of the increasing Boltzmann fractional populations of the probed levels. However, some other resonances display the opposite behaviour. Resonances of the NO $B \leftarrow X$ system at 51649 cm^{-1} ($P_2(28.5)$), 51689 cm^{-1} ($P_2(27.5)$), 51727 cm^{-1} ($P_2(26.5)$), 51801 cm^{-1} ($P_2(24.5)$) and 51805 cm^{-1} ($R_2(27.5)$) are fading with increasing temperature as a result of relatively faster growing fractional population densities of the first vibrationally excited state in the ground electronic state (see also chapter 5 of this thesis). It should be noted that around 51790 cm^{-1} the ArF excimer laser is known to show broadband action due to an intra-cavity C atom absorption [62]. The region of zero oscillator output broadens with the age of the gas fill to about 10 cm^{-1} and bearing the measurement order in mind, the decreasing signal levels in this wavelength region with increasing temperature are explained. Moreover, in about the same region around 51785 cm^{-1} the laser radiation is strongly absorbed by room temperature O_2 (i.e., the R(17) and P(15) resonances of the 4-0 Schumann-Runge band). Within the laser tuning range other regions where these O_2 absorptions occur are centred around 51740 cm^{-1} , 51685 cm^{-1} and 51625 cm^{-1} , respectively [54]. In atmospheric scans the resulting holes in the laser gain profile are much less pronounced than in the excitation scans at higher pressures, however, these ambient air laser absorptions turned out to be crucial for the identification of the weak NO signals at elevated pressures. Still, the decrease with increasing temperature of the numbered peaks around 51626 cm^{-1} ($P_2(36.5)$), 51669 cm^{-1} ($P_1(37.5)$), 51702 cm^{-1} ($Q_2(33.5)$), note that this feature is in fact the strongest observed in the bottom scan), 51745 cm^{-1} ($Q_2(35.5)$) and 51755 cm^{-1} ($R_1(28.5)/Q_1(34.5)$), respectively, cannot be explained by any of the foregoing considerations. From the discussion of fig. 6.2 the explanation is to be found in the coincidences of these mentioned NO lines with various O_2 Schumann-Runge resonances.

From the resemblance of the 1000 °C (top) scan of this figure to the 600 °C OMA spectrum in the previous figure (fig. 6.2B) it can be concluded that, at rising temperatures (i.e., increasing NO fluorescence) the O_2 interference within the bandwidth of the reflection filter apparently becomes less important until at 1000 °C the spectral structures are practically the same although the relative intensities differ somewhat due to the 400 °C temperature difference. The NO- O_2 coincidences primarily lead to absorption of the laser radiation whereas only a minority of the absorption events is followed by fluorescence emissions in the bandwidth of the reflection filter. According to the calculations of Lee *et al.* [54] both the intensity and the complexity of the O_2 absorption spectrum in the laser tuning range increases very rapidly with increasing temperature as a result of strongly absorbing O_2 Schumann-Runge transitions from the $v''=1, 2$ and 3 levels of the ground electronic state. They report that the overall absorption coefficient increases about 2 orders of magnitude on average in going from 300 K to 2000 K and considering the resulting strong absorptions of the laser radiation over the first part of the path in the cell before the measurement volume is reached (about 8 cm), the lower intensity of the above mentioned features in the 1000 °C scan might be caused by the attenuation of the laser intensity at the location of the measurement volume. However, the with temperature increasing peak signals indicate only a limited effect of these O_2 absorptions and it follows that in fact

some of the strongest features of the 600 °C bottom scan of this figure must be attributed to O₂ interference within the reflection filter bandwidth.

As for the transmission of this O₂ fluorescence at 193 nm excitation by the reflection filter, in their flame experiments Wodtke *et al.* [43] found no evidence for O₂ fluorescence around 208 nm (the central wavelength of the reflection filter). However, the neighbouring NO C→X vibrational bands at 204 nm and 211 nm, respectively, were observed to coincide with several rovibronic Schumann-Runge O₂ emission bands. These authors also report an overall reduction of the O₂ interference by at least a factor of 40 in case of narrow bandwidth excitation when compared with broadband excitation. Since this is not investigated for the experimental circumstances of the present study (i.e., lower cell temperatures and a somewhat larger laser linewidth) the contributions of O₂ fluorescence as transmitted by the reflection filter to the NO signals at the mentioned resonances are not known. However, on the evidence of the very strong features around the Q₂(33.5) resonance at 51702 cm⁻¹ observed at the lower cell temperatures in this figure, in case of broadband fluorescence detection these O₂ contributions might easily be stronger than the underlying NO features as in the bottom scans of this figure. The coincidences of the respective NO D←X rotational resonances with rovibronic resonances of O₂ in the Schumann-Runge system may be deduced from the 193 nm O₂ excitation scans as presented by Kim *et al.* [63] using ArF excimer laser radiation with a bandwidth of 1.3 cm⁻¹ and narrow band fluorescence detection around 239 and 232 nm, respectively. From these data the NO P₂(36.5) resonance (labelled 1 in fig. 6.3A) is observed to coincide with the O₂ R(11) resonance of the 14-3 Schumann-Runge band, the NO P₁(37.5) resonance (labelled 2 in fig. 6.3A) coincides with the O₂ R(29) resonance of the 11-2 vibronic band, the NO Q₂(33.5) resonance (labelled 3 in fig. 6.3A) is coinciding with the very strong O₂ P(17) resonance of the 10-2 vibronic band, the NO Q₂(35.5) resonance (labelled 4 in fig. 6.3A) coincides with both O₂ R(3) and P(3) resonances of the 14-3 vibronic band and, finally, the NO R₁(28.5)/Q₁(34.5) resonance (labelled 5 in fig. 6.3A) matches the O₂ R(17) resonance of the 10-2 vibronic band. Furthermore, these authors conclude that their excitation scan observed around 239 nm is best understood as arising from excitation out of the X(v''=3) state whereas the excitation scan measured at 232 nm predominantly shows features arising from excitation out of the X(v''=2) state. With respect to the lower vibrationally excited O₂ states in the ground electronic state both Kim *et al.* [63] and Wodtke *et al.* [64] observed only very weak signals arising from excitation out of the v''=0,1 vibrational states as a result of much smaller absorption cross sections and faster predissociation rates of the accessible vibrational states in the upper B state. However, in view of the lower cell temperatures in this work the contributions of rotational resonances in the O₂ X(v''=1) state to the 204 and 211 nm NO fluorescence cannot be ruled out when using the reflection filter. As for the dominant P(17) and R(17) 10-2 O₂ resonances around 51702 cm⁻¹ and 51755 cm⁻¹, respectively, Kim *et al.* [63] observed the fluorescence signals following excitation out of the X(v''=3) state at the same laser frequencies to be much less strong. This leads to the conclusion that the decreasing signal levels at the positions of the above mentioned NO-O₂ coincidences as observed at rising temperatures with broadband fluorescence detection most probably are brought about by corresponding changes in the fractional O₂ population densities of the v''=2 and v''=3 states in the ground electronic state, in particular.

6.4.2 Higher pressure excitation spectra

In figure 6.4 a set of excitation spectra recorded at 0.5 MPa is presented. Besides the engine scan recorded at 0.5 MPa in-cylinder pressure (E) and excitation scans from the cell at 600 °C (D) and 1000 °C (C) as observed through the reflection filter and by means of the OMA at 600 °C (A), this figure also contains an OMA O_2 excitation scan (B) recorded at 211 nm. Compared to the engine scan at atmospheric pressure (fig. 6.2E), the maximum intensity observed in the engine scan at 0.5 MPa is reduced by about a factor of 2. In this respect, it should be noted that in the fluorescence model the molecular absorption linewidth is accounted for by the overlap integral $g(\phi_{NO}; \phi_{las})$ in eq. (6.1) and that for any specific gas sample the product of the maximum intensity and the absorption linewidth is independent of the actual gas pressure (see also eq. (6.3)). Whereas in the scan at atmospheric pressure the feature around 51702 cm^{-1} was very weak, it seems to have completely disappeared in the 0.5 MPa engine scan. Since the average temperature in the engine is estimated to be about 870 °C (see chapter 5 of this thesis) a higher temperature excitation scan from the cell (C) is also shown in this figure. On the evidence of the weak signals around 51702 cm^{-1} (NO: $Q_2(33.5)/O_2$: P(17)) in the latter 1000 °C scan (C), the sensitivity of the signals around 51702 cm^{-1} to the temperature as observed at atmospheric pressure (fig. 6.3) is demonstrated here once more. The experimental background signal of these spectra recorded through the reflection filter is observed at the ends of the engine scan (E) and the 0.5 MPa scan (D) where the laser beam was blocked. In the OMA experiments the background signal is measured in the same way and subsequently subtracted from the recorded intensities. The vertical scales of the OMA spectra are adjusted accordingly. From the comparison of the vertical scales of the bottom OMA scans in this figure, at a pressure of 0.5 MPa the NO- O_2 fluorescence at 211 nm (B) is about an order of magnitude stronger than the maximum NO fluorescence at 208 nm (A). In view of this, the contributions of NO C(0)→X(3) fluorescence at 211 nm to the signals of the O_2 excitation spectrum (B) probably are very small. Confirmation for this is also found by noting that the spectrum labelled B strongly resembles the O_2 excitation spectrum observed at 232 nm as presented by Kim *et al.* [63]. Finally, from the comparison of the features in the bottom (600 °C) OMA scans the $R_1(24.5)/Q_1(30.5)$ resonance at 51674 cm^{-1} seems to be the least disturbed by O_2 .

Figure 6.5 shows the evolution of the D—X excitation spectra with rising pressure of 500 ppm NO in air and in N_2 as observed around 600 °C at 208 nm by the OMA system. The bottom two scans were recorded at 0.25 MPa, the 0.5 MPa spectrum from the NO- N_2 sample gas in the middle of this figure may be directly compared to the bottom NO-air spectrum of the previous figure (fig. 6.4A) and, finally, the top two scans were recorded at 1 MPa cell pressure. From a rough comparison, the maximum NO fluorescence signal from the NO-air mixture at a pressure of 0.25 MPa (B) is about an order of magnitude weaker than the fluorescence from the NO- N_2 sample (A). At 0.5 MPa the maximum signal from the NO-air sample (fig. 6.4A) is about 15 times weaker than the signal from the NO- N_2 mixture (C), whereas for the pressure of 1 MPa this ratio is only slightly smaller than at 0.5 MPa. Note that in going from 0.25 MPa to 1 MPa the fluorescence intensity from the NO- N_2 sample at the dominant resonances is reduced by about 50%, whereas the maximum NO-air sample fluorescence intensity decreases to about 25%. The pressure broadening of the lines is clearly demonstrated by the linewidths of the $R_1(24.5)/Q_1(30.5)$ resonance around 51675 cm^{-1} and at all pressures the lines

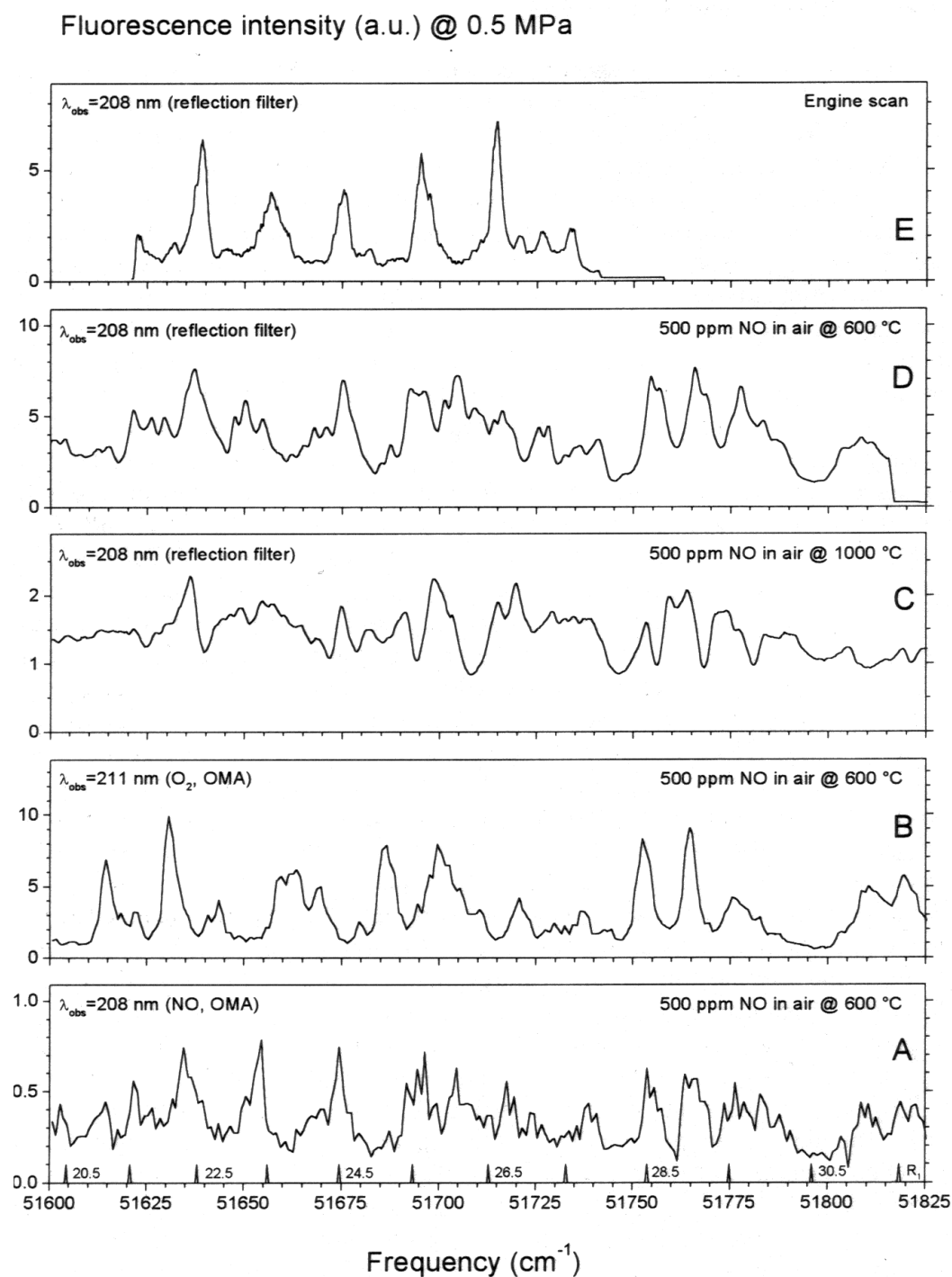


Figure 6.4 Four excitation scans at two different wavelengths and temperatures as measured at 0.5 MPa (500 ppm NO in air) with the OMA (scans A and B) and through the reflection filter (scans C and D). The top spectrum (E) was also measured using the reflection filter at 0.5 MPa in the 0.4 kW loaded engine. The scan in the middle is also recorded through the reflection filter at 1000 °C

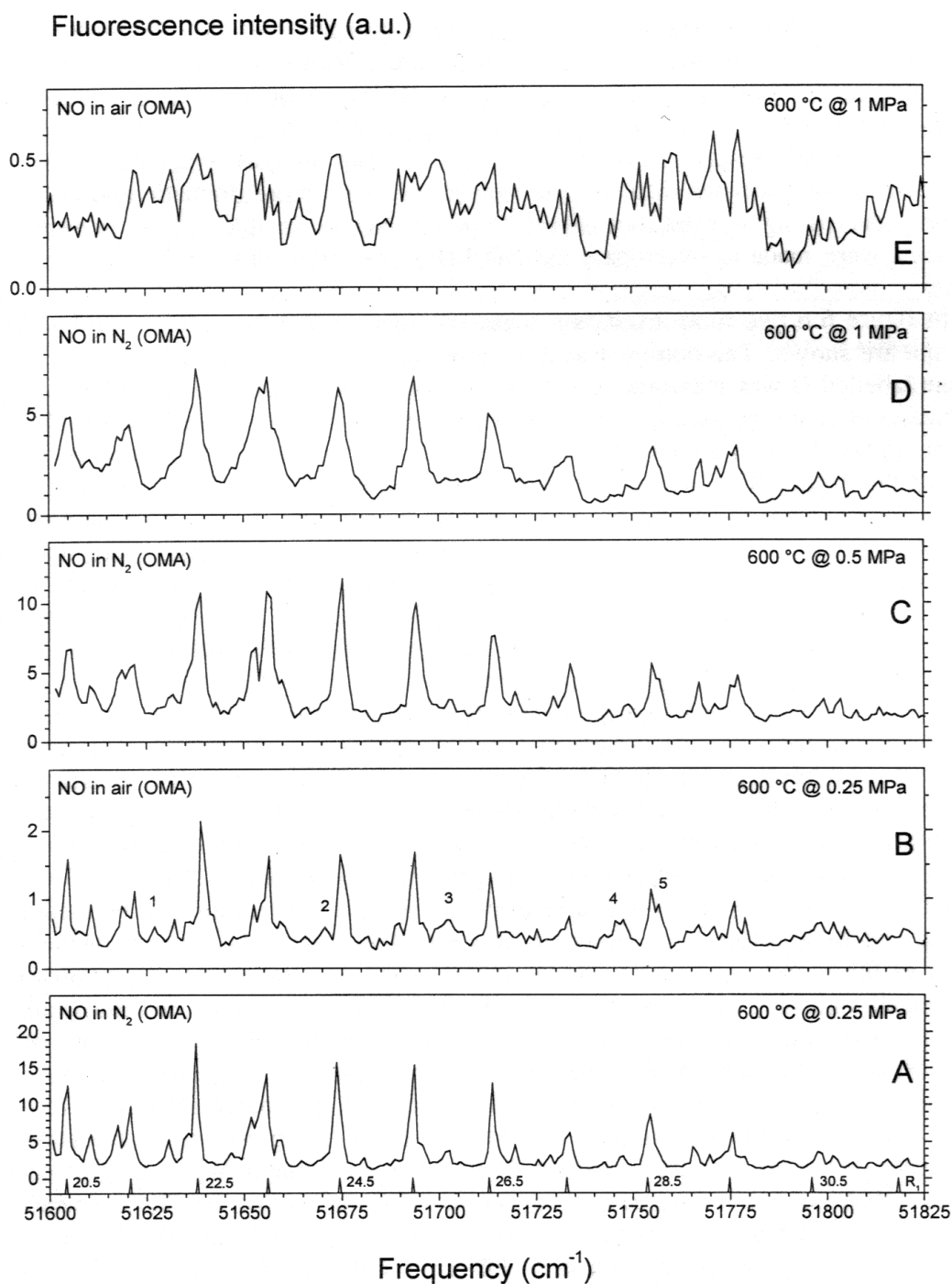


Figure 6.5 Two sets of 600 °C excitation scans (500 ppm NO in air or N_2) as observed with the OMA at different cell pressures. The scan in the middle was recorded at 0.5 MPa in the NO- N_2 gas sample with the OMA as well. The bottom two scans and the top two scans were measured at 0.25 MPa and 1 MPa, respectively. The indicated NO- O_2 coincidences are: 1= $P_2(36.5)$ - $R(11)(14-3)$, 2= $P_1(37.5)$ - $R(29)(11-2)$, 3= $Q_2(33.5)$ - $P(17)(10-2)$, 4= $Q_2(35.5)$ - $R(3)/P(3)(14-3)$ and 5= $R_1(28.5)/Q_1(34.5)$ - $R(17)(10-2)$

observed in the NO-air sample scans are somewhat broader than the lines in the NO-N₂ spectra. Comparing the bottom two OMA scans more evidence for O₂ fluorescence at 208 nm is found at the frequencies of the coinciding NO-O₂ resonances as discussed in the foregoing, viz. 51626 cm⁻¹, 51669 cm⁻¹, 51702 cm⁻¹, 51745 cm⁻¹, and 51755 cm⁻¹ (labelled 1 to 5 in fig. 6.5B, respectively). As the pressure rises the discrepancies between the scans recorded from the two different gas samples are ever more dramatic and because of the rapidly decreasing fluorescence signal from the NO-air sample, in the present study no attempts were made to interrogate the NO LIF signal from this sample at even higher pressures.

In figure 6.6 two more excitation scans recorded at 600 °C with the OMA system at 208 nm are shown. The bottom scan was observed from 250 ppm NO in N₂ at 2 MPa. The scan labelled D was measured at 4 MPa with only about 125 ppm NO in the mixture. Both measured scans are accompanied by results of the simulation code LIFBASE [30] (B,E) multiplied by (the smoothed version of) the laser intensity profile depicted in the middle of this figure (C). In both simulated scans the R₁(26.5)/Q₁(32.5) resonance is the strongest followed by the R₁(23.5)/Q₁(29.5) resonance around 51656 cm⁻¹, however, in both OMA spectra of this figure the latter resonance is the strongest. Note that these OMA spectra, as recorded from the NO-N₂ sample gas, are not disturbed by any O₂ interference other than ambient air absorptions. Nevertheless, whereas the bottom scan still shows a clear NO structure, the scan measured at 4 MPa (D) hardly shows any structure different from the laser intensity profile.

In figure 6.7 the pressure dependence as observed in the excitation scans recorded at 600 °C using the reflection filter is shown for pressures ranging from atmospheric pressure (bottom spectrum) to 5 MPa (top spectrum). The atmospheric pressure bottom scan was measured at a somewhat higher temperature (750 °C) than the other scans of this figure and this spectrum is shown here as a reference for its greater (NO) detail compared with the 600 °C scan as previously presented in the figs. 6.2D and 6.3A. From the discussion of fig. 6.3, most of the features of the bottom spectrum can be assigned to NO D←X and B←X resonances. However, in view of the relatively low cell temperatures all scans of this figure are expected to be contaminated with interfering O₂ fluorescence. As expected, at rising pressures the overall fluorescence intensity decreases and the linewidth increases, therewith complicating the unambiguous assignment of the resonances, up to the point where additional information on the dispersed fluorescence at a particular resonance may be required in order to identify the source (NO or O₂ or both). Spectral structures could be assigned to NO resonances for pressures below about 0.5 MPa (spectra recorded with the reflection filter) or below about 1 MPa (spectra recorded with the OMA system). The largest differences of the reflection filter spectra are observed in the two bottom scans at atmospheric pressure (A) and 0.5 MPa (B). From the foregoing, the growing signal around 51702 cm⁻¹ (NO: Q₂(33.5)/O₂: P(17)) may be considered to be indicative for the degree of O₂ contamination at rising pressures. In this respect it should be noted that for O₂ Schumann-Runge resonances predissociation is the dominant excited state loss mechanism and that predissociation (unlike collisional quenching) is independent of pressure (see e.g. [46,63,64]). Finally, by comparing the top two spectra of this figure to the laser intensity profile shown in fig. 6.6C, the effects of the additional O₂ absorptions of the laser radiation along the path in the cell (as discussed in the foregoing) become evident from the holes observed around 51640 cm⁻¹, 51670 cm⁻¹, 51710 cm⁻¹, 51770 cm⁻¹ and 51780 cm⁻¹, respectively.

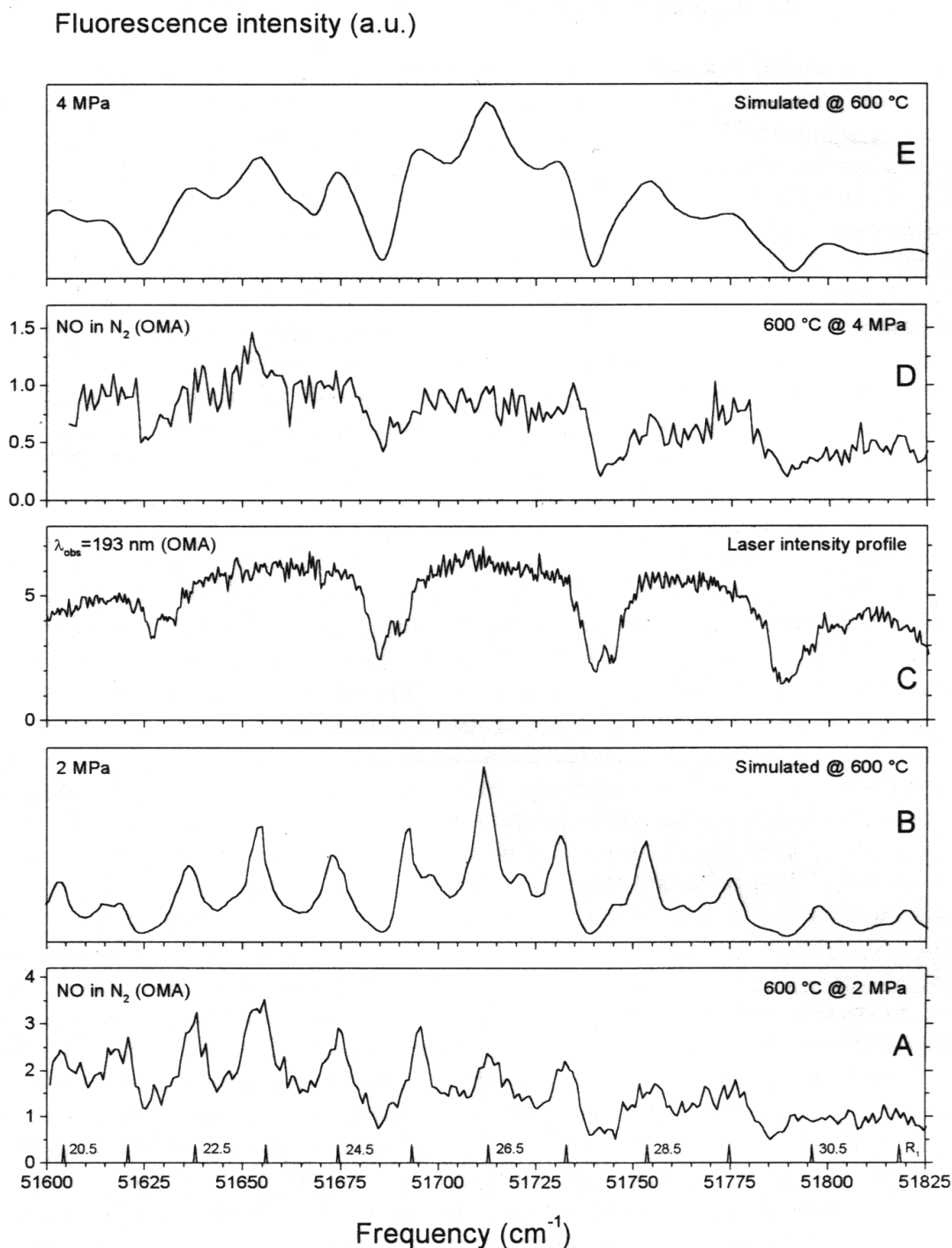


Figure 6.6 Two 600 °C excitation scans as observed with the OMA at different cell pressures. The bottom scan was recorded from 250 ppm NO in N_2 at 2 MPa whereas the spectrum labelled D was observed from 125 ppm NO in N_2 at 4 MPa. The scan in the middle was recorded from room temperature and atmospheric pressure N_2 with the OMA set to monitor the resonantly scattered laser light. The scans labelled B and E were simulated

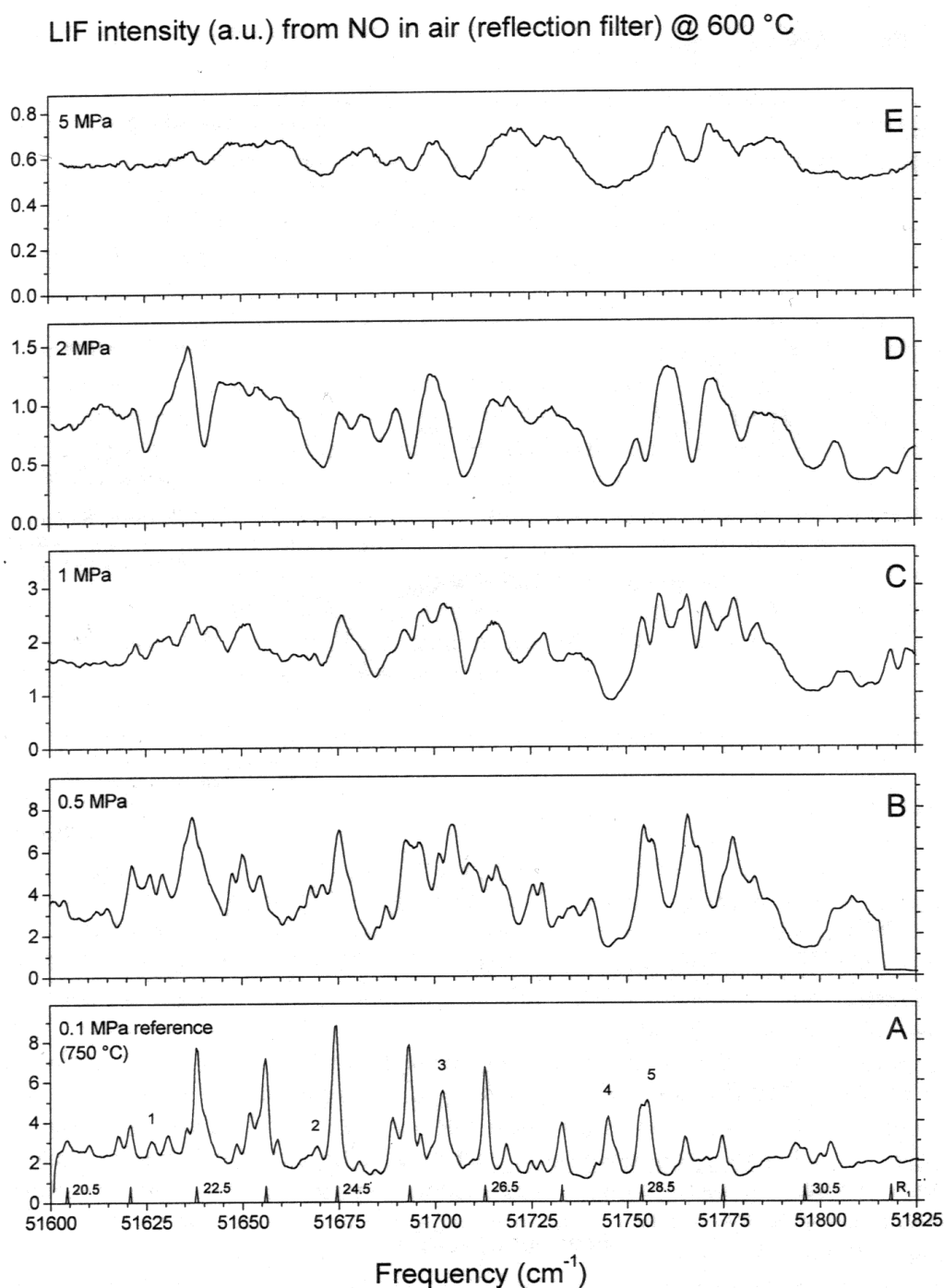


Figure 6.7 Four 600 °C excitation scans (500 ppm NO in air) and a 750 °C reference spectrum (A) as recorded through the reflection filter at various cell pressures ranging from 0.1 MPa to 5 MPa. The assignments of the NO-O₂ coincidences in the bottom scan are: 1=P₂(36.5)-R(11)(14-3), 2=P₁(37.5)-R(29)(11-2), 3=Q₂(33.5)-P(17)(10-2), 4=Q₂(35.5)-R(3)/P(3)(14-3) and 5=R₁(28.5)/Q₁(34.5)-R(17)(10-2)

6.4.3 Data analysis

Referring to eq. (6.2), at a given temperature (e.g. 600 °C) and pressure p the inverted normalized fluorescence signal ($1/Y'(p)$) equals the effective broadening factor. As the evaluation of both the fluorescence intensities Y and the FWHM linewidths at the various pressures obviously requires that the frequency-independent background signals observed in the spectra are properly accounted for, this topic is discussed first of all. In their LIF study of NO in high-pressure methane flames, Battles *et al.* [46] determine the O_2 background signal by tuning their laser off the (O_2 interference free) NO feature. However, by subtracting this off-resonant signal one implicitly assumes that this frequency-independent signal contains no contributions of (broadband) fluorescing NO molecules at all. This clearly cannot be true for the background signals observed in the excitation spectra from the NO- N_2 mixture presented later in this work, whereas, on the other hand, the background signals observed in the engine spectra may be expected to contain contributions of various other sources of broadband fluorescence than O_2 . As for the spectra recorded from the NO-air mixture, the contributions of NO fluorescence to the observed background signals are not known (yet). Note that in the case of narrow-band (OMA) fluorescence detection the NO fractions of the background signals probably are much larger than when using the reflection filter. Because of this uncertainty with respect to the NO part of the frequency-independent background signals the evaluation of the fluorescence intensities Y as well as the determination of the FWHM linewidths is performed with and without background subtraction by assuming no broadband NO fluorescence and 100% broadband NO fluorescence, respectively. For each spectrum the background signal as such is taken to be the minimum (off-resonant) signal observed in that particular spectrum. The results are averaged in order to produce a value corresponding to the situation that the NO fraction of the background fluorescence is 50% as well as the extreme values, the latter also serving as an estimate of the extent as to which the fluorescence model is sensitive to these background signals.

For pressures up to 1 MPa the fluorescence intensities Y are evaluated from the measured OMA spectra for the $R_1(24.5)/Q_1(30.5)$ resonance at 51674 cm^{-1} (with and without background subtraction as discussed in the foregoing). This particular resonance is chosen for its isolated position in the excitation scans at higher pressures (see figs. 6.5D and 6.5E) and the expected relatively weak interference from neighbouring O_2 Schumann-Runge resonances around this frequency (see figs. 6.4A and 6.4B). In figure 6.8 the effective broadening factors resulting from this evaluation for the respective measurement series are indicated by the open symbols, whereas the broadening factors as directly observed in the excitation scans are indicated by the solid symbols. The indications OMA and RF in the legend of this figure stand for the OMA measurements and the reflection filter measurements, respectively. Note that, for clarity, the RF results at 0.5 MPa are shown at a slightly higher pressure. All points represent the values found for the case that 50% of the frequency-independent background signals in the various scans originate from broadband fluorescing NO molecules. The error bars result from assuming 0% and 100% NO background levels. Referring to the discussion of the linewidths observed in the engine spectra in the previous chapter, the about equal effective broadening factors at 0.5 MPa as observed in the engine scans and the NO- N_2 OMA spectra should be noted. From the figure, in the case of the OMA spectra recorded from the NO- N_2 gas sample there is reasonable agreement between the broadening factors

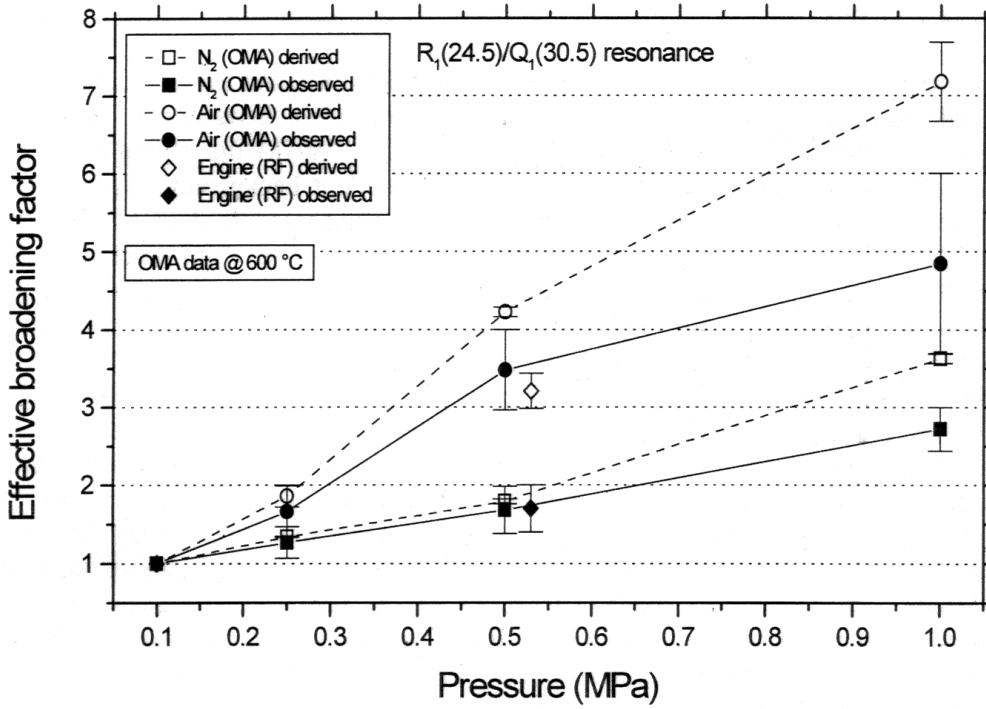


Figure 6.8 *Effective broadening factor as evaluated from the observed LIF intensities at the $R_1(24.5)/Q_1(30.5)$ resonance (open symbols) along with the broadening factor as derived from a direct comparison of the linewidths observed in the excitation scans presented in this work (solid symbols)*

as derived from the fluorescence intensities Y and the broadening factors as observed in the respective NO-N₂ OMA spectra. This indicates that the previous assumption on linear pressure broadening (section 6.3) is justified in case of the NO-N₂ sample. This also seems to be the case for the spectra recorded from the NO-air mixture although the discrepancy between derived and observed values grows with pressure. It is important to note that from the fluorescence model, the different slopes of the derived curves (open symbols) also reflect the effective cross sections of the sample gases involved. However, as will be shown, the large deviation of the broadening factors derived from the intensities Y in the NO-air sample scans and the engine spectra merely indicates that the previous assumption regarding the constant local laser intensity I in the cell, obviously, does not hold in the presence of (hot) O₂.

From rearranging eq. (6.1), one may write

$$\gamma_{\text{NO}}(p,T) \propto \frac{I(p,T) \eta_1(T) \sqrt{T}}{Y(p,T) \sigma_{\text{eff}}(T)} \quad (6.4)$$

where the pressure and temperature dependencies are explicitly given and the value of the overlap integral is approximated by $1/\gamma_{\text{NO}}(p,T)$ as discussed in section 6.3. By differentiating with respect to p one finds that the slope in case of with pressure varying laser intensities in the cell actually is given by

$$\gamma'_{\text{NO}}(p) = \frac{\eta_1(T) \sqrt{T}}{\sigma_{\text{eff}}(T)} \frac{I'(p)Y(p) - I(p)Y'(p)}{Y^2(p)} \quad (6.5)$$

where the primes now denote the first order derivatives (instead of normalized variables). Note that both $I'(p)$ and $Y'(p)$ are negative and that in the absence of O₂ absorptions in the cell (i.e., in the NO-N₂ experiments) $I'(p)$ only differs from zero as a result of the absorptions of the laser radiation by the 0.5‰ NO fraction of the molecules. It follows that if one were to correct for these absorptions, the resulting slope of the derived NO-air broadening factors would be less steep and consequently more in line with the slopes of the observed broadening in the NO-air experiments. As for the relatively larger broadening factors at 0.5 MPa for the NO-air OMA spectra, it should be noted that from similar considerations as given above for the laser intensity, these somewhat larger broadening factors most probably result from inaccuracies in the sample preparation of these specific measurements.

The slope of the observed NO-N₂ OMA broadening factors (solid squares) is found to be about 1.9 MPa⁻¹. In this respect, Reisel *et al.* [47] report the following expression for the broadening of NO A–X lines by N₂

$$\Delta\nu(\text{NO}) = 0.585 \left(\frac{295}{T}\right)^{0.75} p \quad (6.6)$$

with ν as the central frequency in cm⁻¹ and p in atm. The evaluation of this expression at 600 °C leads to a slope of about 2.6 MPa⁻¹ which is somewhat steeper than the slope observed in the present D–X study.

Finally, figure 6.9 shows the results of the evaluation of eq. (6.3) for each of the 5 dominant NO D–X resonances starting with the R₁(22.5)/Q₁(28.5) resonance and ending with the R₁(26.5)/Q₁(32.5) resonance. The effective cross section ratios $\sigma_{\text{eff}}(\text{air})/\sigma_{\text{eff}}(\text{N}_2)$ are derived from the observed intensities in the atmospheric pressure (600 °C) OMA spectra (the figs. 6.2B and 6.2A) and the ratios $\sigma_{\text{eff}}(\text{air})/\sigma_{\text{eff}}(\text{engine})$ are derived in the same way from the reflection filter experiments (the figs. 6.3C and 6.2E). For clarity, the individual resonances are only indicated by their R₁ component. The ratios are calculated by assuming equal linewidths in the OMA scans and the RF scans at atmospheric pressure, i.e., by setting the last factor at the right hand side of eq. (6.3) to unity. Again, the error bars indicate the maximum and minimum values as obtained by assuming 0% and 100% NO background levels, respectively, whereas the bars represent the situation in which 50% of the broadband background signal is assumed to come from NO molecules. It must be emphasized that the different values of the ratios for the various resonances in both the OMA and the reflection filter experiments most probably are not brought about by the different rotational quantum numbers of the probed levels. Referring to the discussion of the previous figure and noting that O₂ is involved in both OMA and RF effective cross section ratios presented here, the different ratios for the various resonances are believed to merely reflect the resulting absorptions of the laser radiation in the cell at the respective laser frequencies. From a similar reasoning as described above, it can be shown that any attenuations of the local laser intensity now tend to lead to larger values of the evaluated cross section ratios. The minimum value as derived from the reflection

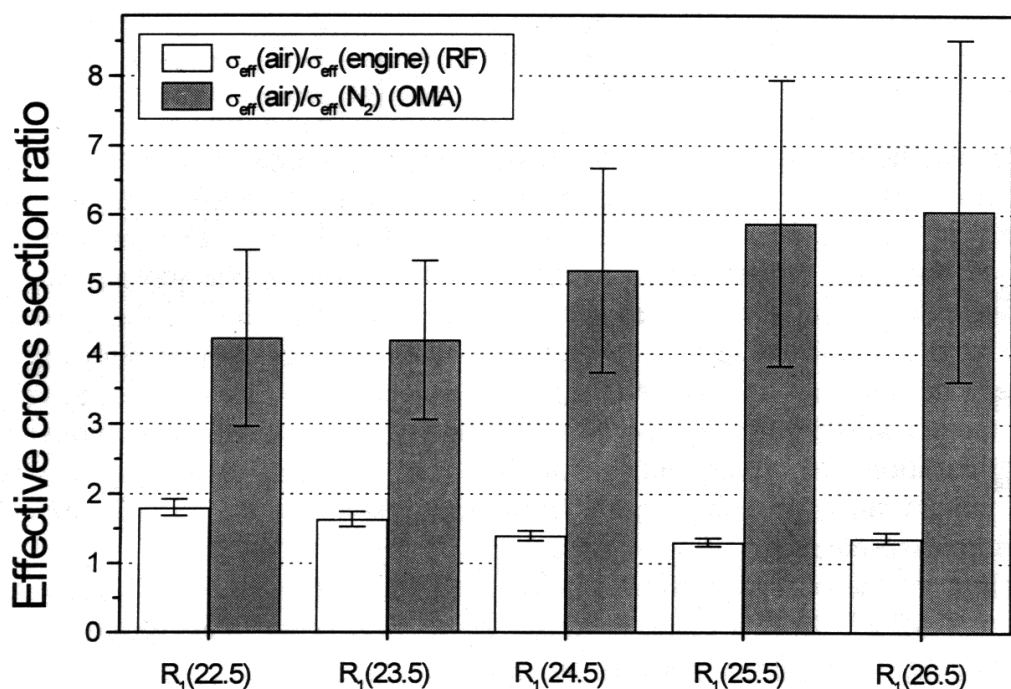


Figure 6.9 The resulting effective cross section ratios of NO $D^2\Sigma^+(v'=0)$ fluorescence quenching evaluated for the individual resonances of interest. The grey bars represent the values of the $\sigma_{\text{eff}}(\text{air})/\sigma_{\text{eff}}(\text{N}_2)$ ratio computed from the OMA experiments whereas the white bars represent the values of the $\sigma_{\text{eff}}(\text{air})/\sigma_{\text{eff}}(\text{engine})$ ratio as observed in the regular imaging setup using the reflection filter. The various resonances are indicated by their order in the R_1 progression only

filter experiments for the ratio $\sigma_{\text{eff}}(\text{air})/\sigma_{\text{eff}}(\text{engine})$ is about 1.3 for the $R_1(25.5)/Q_1(31.5)$ resonance and referring to the discussion of the engine spectra in the previous chapter, this value of 1.3 (as being around unity) is confirmed in the literature on internal combustion engines⁶. As for the observed minimum value of 4.2 for the ratio $\sigma_{\text{eff}}(\text{air})/\sigma_{\text{eff}}(\text{N}_2)$ in the OMA experiments, it should be noted that this ratio probably is even smaller as a result of the last factor on the right hand side of eq. (6.3) actually being somewhat smaller than unity (see figs. 6.2A and 6.2B). However, in the absence of data on the local laser intensity the comparison with data on the various collision cross sections for NO quenching as reported in [32,35] is difficult. Using the collision cross sections of O_2 (67 \AA^2) and N_2 (6.8 \AA^2) for D state quenching as reported by Asscher *et al.* [35] one finds (by evaluating the sum $\sum_i[\chi_i\sigma_i(T)/\sqrt{\mu_i}]$ while ignoring the differences of the respective reduced masses) an effective cross section ratio of about 2.8. However, the insertion of the cross

⁶ On the basis of the comparison of the 0.5 MPa engine scan recorded through the reflection filter and a 0.5 MPa OMA scan at 600 °C from the NO- N_2 mixture, in chapter 5 a value of about 0.5 for the ratio $\sigma_{\text{eff}}(\text{air})/\sigma_{\text{eff}}(\text{engine})$ is estimated. Here, by comparing the engine scan at atmospheric pressure to an atmospheric pressure RF NO-air spectrum at 800 °C a value of 1.3 is found for the same cross section ratio. This might indicate that the composition of the in-cylinder gas possibly varies with pressure since the respective cross sections for NO quenching do not. However, on the basis of the current set of data this cannot be verified any further.

sections for A state quenching as reported by Paul *et al.* [32] (26 \AA^2 for O_2 and 0.2 \AA^2 for N_2 , respectively) yields an effective cross section ratio of about 26.8, which is very much larger than the (minimum) value of 4.2 derived from the OMA spectra in this work.

6.5 Summary and conclusions

The effective cross section ratios for NO $D^2\Sigma^+(v'=0)$ fluorescence quenching as obtained from the application of a simplified fluorescence model to a single set of measurements show a better agreement with the cross section ratio derived from data of Asscher *et al.* [35] on NO D state collision cross sections of O_2 and N_2 than with the ratio derived from the data of Paul *et al.* [32] on the corresponding NO A state collision cross sections. As originally developed in 226 nm NO A \rightarrow X studies, under the assumption that (unknown) EET rates in the excited state effectively act as additional quenching rates, the model is also shown to adequately describe the D \rightarrow X fluorescence from the dominant resonances at higher pressures and temperatures, provided these resonances are reasonably free from O_2 interference. Another problem posed by the presence of O_2 is that the absorptions of the laser radiation erroneously are translated into larger effective broadening factors and effective cross section ratios. Because of this, in future experiments more attention should be paid to the precise monitoring of the local laser intensity.

Chapter 7

Epilogue

Although diesel engines have been subject to continuous development ever since their invention in 1897, about the physics and chemistry of the processes in their cylinders still little is known. A better understanding of these processes might very well be a crucial success factor in the fight against their toxic emissions. The objective of the experiments reported in this thesis was the development of non-intrusive laser-based diagnostic techniques facilitating the study of in-cylinder distributions of NO (nitric oxide) molecules in an optically accessible IDI diesel engine.

Following the absorption of laser photons, for a few nanoseconds, NO molecules are able to emit fluorescence, and by imaging this fluorescence from a plane in the cylinder, the distribution of NO molecules within that plane can be visualized. The LIF signal only occurs at very specific laser wavelengths typical for NO and this feature allows for the discrimination of NO molecules from all other molecular species contained in the in-cylinder gas. Apart from a number of spectroscopic and experimental constants, the intensity of the fluorescence from any particular point in the imaged area depends on the local density of NO molecules, the local laser intensity, the temperature and the pressure of the in-cylinder gas as well as on the local chemical composition. The dependence on the local temperature arises from the fact that not all NO molecules will absorb the incident laser photons as they do have to be in a very specific energetic state in order to be promoted to another specific (energetically higher lying) excited state. Using Boltzmann statistics this dependence can relatively easily be assessed and, hence, compensated for if the temperature is known. The dependence of the LIF signal on the pressure and the chemical composition of the in-cylinder gas mainly is a consequence of the fact that not all excited NO molecules do actually emit fluorescence. Presently unknown fractions of excited molecules lose their electronic energy in collisions with the other molecules and particles in the gas. They also may lose vibrational energy only and then emit fluorescence outside the wavelength region of the detection system or on a different time scale. This unknown collisional quenching of the fluorescence signal hampers the quantification of the imaged NO fluorescence distributions. However, by using a simplified fluorescence quenching model the quantitative interpretation of the essentially qualitative LIF results can be approached. The subsequent experiments described in this thesis were aimed at the detailed study of the dependence of the LIF signal on the mentioned parameters as to properly account for all their effects on the measured NO fluorescence distributions.

At the time of the first experiments in 1991, the imaging of molecular distributions by means of laser-induced fluorescence was a relatively new technique in internal combustion engine studies after having already proved to be a very powerful molecule-specific diagnostic tool in, from a spectroscopic point of view, less hostile experimental environments. The spectroscopic hostility of diesel engines mainly arises from the presence of many residual soot-particles in the in-cylinder gas throughout a large part of the combustion cycle. Besides by its obscuring of the optical access channels in the long run, the soot poses another problem by absorbing and scattering both the incident laser radiation and the induced fluorescence. Therefore, most of the research is performed using

low-sooting fuels while operating the engines in a skip-fired mode (i.e., the combustion is only invoked any selectable number of cycles) avoiding the need for lubrication in the cylinder therewith reducing soot concentrations at the same time. In some of the very first NO-LIF engine combustion studies reported in literature (e.g. Alataş *et al.* [8]) the soot production was reduced even further by supplying 20-40% extra oxygen to the air inlets of the test engines. However, also in the more recent experiments by Nakagawa *et al.* [14] about 20-35% extra oxygen was supplied to the air inlet of their continuously firing DI low-sooting-fuel-driven test engine. Although the very first experiments reported in this thesis were also performed using a low-sooting substitute fuel (n-heptane), it soon turned out that the experimental problems with respect to the soot production and the lubrication were sufficiently solved to allow for measurement sessions under steady-state engine operating conditions lasting up to about 45 minutes while using standard diesel fuel, about 10-15% oxygen-enrichments of the engine intake air and a minimized amount of an UV-transparent, non-flammable lubricant in the crank case of the engine. Of course, the improved availability of oxygen in the combustion chamber will affect the combustion process as a whole and in this sense, such an experimental measure certainly may be considered to be intrusive. However, in this respect, it should be kept in mind that the objective of the research reported in this thesis was the development of laser-based diagnostic techniques for the observation of NO molecules inside a running diesel engine in preparation for the study of the combustion process itself. Unfortunately, in the IDI test engine pertinent to this work the combustion chamber was not made optically accessible and as a consequence, the combustion process itself could not be studied (yet). However, when applying the developed diagnostic techniques to future studies of the combustion processes in e.g. optically accessible DI test engines, it is obvious that the intrusions posed by all experimental measures such as fuel type, oxygen-enrichment of the intake air and skip-fired engine operating conditions, should be even more carefully considered. In general, the higher combustion temperatures resulting from oxygen-enriched combustion tend to lead to lower soot production rates as well as higher NO concentrations. On the other hand, as a result of the construction of the optical access channels in the cylinder wall of the test engine, the compression ratio turned out to be about halved and in this respect, the additional oxygen in the combustion chamber serves as compensation for the lowered combustion temperatures in the test engine resulting from its modification. In recent generations of DI research engines more sophisticated designs of the optical access channels allow for maintaining the originally rated compression ratios, therewith eliminating the need for oxygen-enriched combustion in many cases. However, in contrast to the engine operating conditions of most of the experiments reported in this thesis, the use of low-sooting substitute fuels and skip-fired engine operating modes is still widespread amongst the most recently published engine combustion studies. Finally, the very fortunate feature of nearly unlimited periods of measuring time as displayed by the engine setup allowed for the recording of several unique and very convincing high-resolution excitation spectra (i.e., spectroscopic fingerprints) from in-cylinder NO at steady engine operating conditions as well as for the recording of overall in-cylinder NO fluorescence distributions measured in sufficiently large amounts of individual cycles as to average out any disturbing cyclic variations.

Some features observed in the (first) NO fluorescence distributions [9] gave rise to the development of image-processing techniques by which the effects of two major artifacts of the detection method can be removed from the initially imaged fluorescence

distributions. The resulting image-processing correction procedures [13] account for the various effects of the gradually decreasing transparency of the optical access channels (the effects for the laser input channel are somewhat different from those for the observation channel) as well as for the in-cylinder attenuation of the laser intensity. Both methods make use of several relevant cycle-averaged in-cylinder laser intensity distributions as measured by imaging the elastically scattered laser radiation at the various crank angles and engine conditions. The verification of the various assumptions underlying these image-processing correction routines also included imaging experiments using opposite propagation directions of the laser light-sheet through the cylinder. In these experiments the reconstructed NO distributions were found to be very similar for both laser propagation directions, as they obviously should. In another experiment the intensity of the 2D-LIF signal was found to be linearly dependent on the local in-cylinder laser intensity, therewith justifying the correction procedures with respect to the in-cylinder laser intensity distributions. The degree as to which saturation might occur at the in-cylinder laser intensities pertinent to this work, was estimated using spectroscopic data and relations found in the literature. From this estimate it is concluded that saturation effects most probably only are of minor significance in the experiments reported in this thesis. Whether the incident laser radiation was intrusive or not, was tested by measuring the sensitivity of the LIF signal from in-cylinder NO to photo-chemically induced effects possibly arising from the use of a high-power UV excimer laser (ArF, 193 nm). In this double-resonance experiment a second laser system was employed to produce tunable radiation around 226 nm, the latter wavelength being the commonly used alternative in most of the NO LIF experiments found in the literature. Photo-chemical effects, creating or annihilating NO, were not observed.

The reconstructed (more realistic) NO distributions at the various crank angles and loads of the diesel-fuel-driven engine led to further investigations of the dependence of the 2D-LIF signal on the other previously mentioned parameters. Calculations of the sensitivity of the 2D-LIF signal to the local gas temperature, using Boltzmann statistics, indicate an increase of the LIF signal by about 30% in case of in-cylinder temperature variations in the order of about 100 °C. This sensitivity of the 2D-LIF signal to the local gas temperature most probably explains the occurrence of several hot spots in the reconstructed NO distributions. In the absence of experimental data on the in-cylinder gas flows and the resulting in-cylinder temperature distributions, the pixel-averaged 2D-LIF intensity found in the reconstructed NO distributions is subsequently corrected for overall temperature effects as well as collisional quenching on the basis of a simplified model. The resulting curves of the NO density versus crank angle at the selected loads are calibrated by comparing the densities at the end of the expansion stroke (i.e., at atmospheric pressure) at the various loads with the corresponding tail-pipe NO_x concentrations observed. The reproducibility of the reconstructed NO distributions at the various crank angles and loads as well as the experimental accuracy were investigated by evaluating the normalized standard deviations of the mean pixel value contained in the ratios of reconstructed images as recorded in repeated measurements sessions using the same engine operating conditions. Some of the reconstructed NO distributions resulting from the previously mentioned experiments in which both laser propagation directions were used, were also included in this evaluation. From this analysis and from our own experience, the best reproducible NO distributions at the various crank angles were observed in case the engine was loaded. By assuming that the systematic errors are the

same for all selected crank angles, a worst case estimate of the experimental accuracy of the imaging experiments was found to be about 40%. Of course, this accuracy would be greatly improved if the resulting distributions could also be corrected for the effects of in-cylinder temperature gradients over the imaged area, which is not yet possible in the current absence of reliable data on the cycle-averaged in-cylinder temperature distributions.

Finally, the fluorescence quenching model used for the quantification of the 2D-LIF results in the form of the NO density curves is validated on the basis of a large set of NO excitation spectra recorded from various sample gases in a high-temperature high-pressure optically accessible cell. In these experiments both broadband and narrow-band fluorescence detection systems are used to investigate the interference by fluorescence from molecules other than NO (e.g. molecular oxygen) for cell pressures up to 5 MPa at temperatures ranging from 600 °C to 1000 °C. In the imaging experiments in the running engine, necessarily, a relatively broadband 2D optical filter (13 nm FWHM bandwidth) is used for the selection of a specific NO fluorescence wavelength region (around 208 nm in this work) from all interfering fluorescence in adjacent wavelength regions. From the reported set of 193 nm NO excitation scans recorded through a narrow-band 1D-filter (bandwidth 2 nm FWHM) at 208 nm, it is clear that the selectivity of the 2D-LIF imaging technique, as it stands, would be strongly improved by the expected future availability of tunable optical 2D-filters with much narrower bandwidths. For both narrow-band and broadband fluorescence detection the experimentally observed broadening of one of the least disturbed NO resonances at rising cell pressures up to 1 MPa, is compared to the broadening as derived from the fluorescence quenching model. Irrespective of the fluorescence detection bandwidth, the experimentally observed broadening is somewhat smaller than the broadening as predicted by the fluorescence model. However, in both cases the broadening increases linearly with the cell pressure. Unfortunately, due to the lack of data in the literature on the line broadening of NO resonances around 193 nm, no direct comparison with literature values can be made. However, the broadening factors for NO resonances around 226 nm as reported in the literature indicate similar line broadening for both excitation wavelengths. The presence of 20% oxygen in one of the sample gases pertinent to this chapter (i.e., an NO-air mixture) leads to considerably larger linewidths than experimentally observed and derived for a sample gas without oxygen (i.e., an NO-nitrogen mixture). As the LIF intensities decrease with increasing linewidths, it is concluded that molecular oxygen is a stronger quencher of the fluorescence than molecular nitrogen. In this respect, it should be noted that for NO A-state fluorescence the quenching by molecular oxygen is even stronger than the quenching of NO D-state fluorescence studied in this work [e.g. 32,35]. The probabilities for collisional quenching of excited NO molecules by the other molecular species in the sample gas usually are expressed in terms of the various molecule-specific collision cross sections. According to the fluorescence quenching model, the comparison of the LIF peak intensities at atmospheric pressure for the dominant NO resonances as observed in different sample gases provides a way to determine relative values for the NO quenching cross sections. In the case of narrow-band fluorescence detection these evaluations show an about 4.2 times larger quenching cross section found for the 20% oxygen containing NO-air sample compared to the quenching cross section of the NO-nitrogen sample. In the case of broadband fluorescence detection by comparing the LIF peak intensities at atmospheric pressure as observed in the excitation scan from the running engine with the peak intensities recorded from the NO-air

sample in the cell, an about 1.3 times larger quenching cross section for the NO-air sample gas is found in comparison to the quenching cross section of the in-cylinder gas. This value (as being around unity) also is confirmed in [60] where it is stated that at moderate loads the chemical composition of the diesel exhaust gas hardly differs from that of air. The experimental error in these evaluations predominantly results from the uncertainty with respect to the local laser intensity in the measurement volume during the measurement sessions; however, within this accuracy the quenching cross section ratios using narrow-band fluorescence detection can be compared to ratios that may be derived from reported data on the quenching cross sections of nitrogen and oxygen. For fluorescence following excitation around 193 nm, the quenching cross section ratio is derived to be about 2.8 which is in reasonable agreement with the value of 4.2 reported in this work. The value around 26.8 derived for the same quenching cross section ratio in the alternative case of excitation around 226 nm mainly results from the above mentioned stronger quenching of the NO A-state fluorescence by molecular oxygen.

Undoubtedly, the increasingly higher combustion pressures will be a most challenging factor in future LIF imaging experiments to reveal the NO formation processes in realistic diesel engines. Besides by severe attenuation of the in-cylinder laser intensity, the 2D-LIF signal will be weakened by increased collisional quenching as well. Whereas the problem of too low in-cylinder laser intensities perhaps can be solved by future generations of more powerful lasers and improved imaging optics, the stronger collisional quenching of the induced fluorescence becomes an increasingly larger problem. Life is complicated even more by interfering fluorescence from other molecular species (mainly molecular oxygen) leaking through the relatively broadband imaging filter used in this work; this filter, presently, still being the narrowest one available for 193 nm NO imaging studies. Future LIF imaging research in DI diesel engines on the NO formation processes at much higher pressures up to 10 MPa will suffer from the effects of increased collisional quenching on the LIF signal strength, up to the point where the LIF signals become too weak for imaging. Nevertheless, very recent results of Dec *et al.* [65] indicate that NO LIF imaging remains possible for engine pressures up to about 7 MPa, albeit using the alternative LIF detection scheme for NO around 226 nm. Yet unpublished results of Stoffels *et al.* [66] will include various dispersion scans of the fluorescence following 193 nm excitation as recorded from in-cylinder NO in a 2-stroke DI diesel engine at pressures up to 7.5 MPa. In these latter experiments it turns out that at the highest pressures the NO LIF signals probably are already too weak for imaging. It should be noted that both NO detection schemes are complicated by interfering fluorescence from molecular oxygen and that as a consequence of the predissociative character of the excited oxygen state, the intensity of this interfering fluorescence, unlike the intensity of the collisionally quenched NO fluorescence, hardly shows any pressure-dependence. It is obvious that on the basis of the results reported in this thesis no predictions can be made as to which LIF detection scheme and which narrow-band fluorescence filter setup will eventually enable imaging studies of NO formation at the even much higher in-cylinder pressures of future generation diesel engines (allegedly, up to 22 MPa!). In any case, at these future in-cylinder pressures of interest the subsequent identification, validation and quantification of the 2D-LIF results can be expected to be much more complicated than at the moderate engine pressures encountered in this thesis. Nevertheless, provided sufficiently strong NO signals can be observed at these high combustion pressures in the first place, there seem to be no other factors withstanding the correction and the quantification of the future results in a similar

way as described in this work. Present obstacles for this quantification like unknown absolute laser intensity distributions over the imaged area as well as unknown in-cylinder temperature distributions probably will be removed in the near future. At the time of writing, experiments on the determination of in-cylinder temperature distributions by means of two-line LIPF (Laser-Induced Predissociative Fluorescence) thermometry on oxygen in combination with the spectral analysis of the natural emission using Planck's law, are in progress. Considering the rate of development of the information technology, such combinations of simultaneously imaged NO-LIF and O₂-LIPF distributions certainly are amongst the most promising perspectives for future combustion research.

References

- [1] K.-P. Schindler, "Diesel combustion: Integrated Diesel European Action," Fisita Seminar, Turin, Italy (1990)
- [2] F.J.J.G. Janssen, "The selective catalytic reduction of nitric oxide with ammonia," Ph.D. Thesis, University of Twente, The Netherlands (1987)
- [3] J. Olbregts, "Termolecular reaction of nitrogen monoxide and oxygen: a still unsolved problem", *Int. J. Chem. Kin.* **17**, 835-848 (1985)
- [4] P.O. Wennberg, R.C. Cohen, R.M. Stimpfle, J.P. Koplow, J.G. Anderson, R.J. Salawitch, D.W. Fahey, E.L. Woodbridge, E.R. Keim, R.S. Gao, C.R. Webster, R.D. May, D.W. Toohey, L.M. Avallone, M.H. Proffitt, M. Loewenstein, J.R. Podolske, K.R. Chan, S.C. Wofsy, "Removal of stratospheric O₃ by radicals: in situ measurements of OH, HO₂, NO, NO₂, ClO and BrO," *Science* **266**, 398-404 (1994)
- [5] K. Binder, F. Wirbeleit, "Innere motorische Massnahmen zur Stickoxid-Reduktion bei NFZ-Dieselmotoren," Symposium on engine combustion, Essen, Germany, ESYTEC Energie- und Systemtechnik GmbH (1997)
- [6] P. Andresen, G. Meijer, H. Schlüter, H. Voges, A. Koch, W. Hentschel, W. Oppermann, E. Rothe, "Fluorescence imaging inside an internal combustion engine using tunable excimer lasers," *Appl. Opt.* **29**, 2392 (1990)
- [7] A. Arnold, F. Dinkelacker, T. Heitzmann, P. Monkhouse, M. Schäfer, V. Sick, J. Wolfrum, W. Hentschell, K-P. Schindler, "DI diesel engine combustion visualized by combined laser techniques," 24th Symposium on Combustion, Sydney (1992)
- [8] B. Alataş, J.A. Pinson, T.A. Litzinger, D.A. Santavicca, "A study of NO and soot evolution in a DI diesel engine via planar imaging," SAE Paper 930973 (1993)
- [9] Th.M. Brugman, R. Klein-Douwel, G. Huigen, E. van Walwijk, J.J. ter Meulen, "Laser-induced fluorescence imaging of NO in an n-heptane- and diesel-fuel-driven diesel engine," *Appl. Phys. B* **57**, 405-410 (1993)
- [10] W. Hentschel, K.-P. Schindler, O. Haahtela, "European diesel research IDEA-experimental results from DI diesel engine investigations," SAE Paper 941954 (1994)
- [11] Ch. Schulz, B. Yip, V. Sick, J. Wolfrum, "A laser-induced fluorescence scheme for imaging nitric oxide in engines," *Chem. Phys. Lett.* **242**, 259-264 (1995)
- [12] M. Knapp, A. Luczak, H. Schlüter, V. Beushausen, W. Hentschell, P. Andresen, "Crank-angle-resolved laser-induced fluorescence imaging of NO in a spark-ignition engine at 248 nm and correlations to flame front propagation and pressure release," *Appl. Opt.* **35**, 21 (1996)
- [13] Th.M. Brugman, G.G.M. Stoffels, N. Dam, W.L. Meerts, J.J. ter Meulen, "Imaging and post-processing of laser-induced fluorescence from NO in a diesel engine," *Appl. Phys. B* **64**, 717-724 (1997)
- [14] H. Nakagawa, H. Endo, Y. Deguchi, M. Noda, H. Oikawa, T. Shimada, "NO measurement in diesel spray flame using laser-induced fluorescence," SAE Paper 970874 (1997)

-
- [15] R.J. Donahue, G.L. Borman, G.R. Bower, "Cylinder-averaged histories of nitric oxide in a DI diesel engine with simulated turbocharging," SAE Paper 942046 (1994)
- [16] J. Meyer, M. Schreiber, M. Haug, A. Siemers, H.J. Schulpin, "Quantitative fuel distribution in a spark ignition engine," internal report University of Aachen (RWTH), Germany
- [17] J.E. Dec, Ch. Espey, "Soot and fuel distributions in a DI diesel engine via 2D-imaging," SAE Paper 922307 (1992)
- [18] E. Winklhofer, H. Fuchs, H. Philipp, "Diesel spray combustion - an optical imaging analysis," SAE Paper 930862 (1993)
- [19] M. Suzuki, K. Nishida, H. Hiroyasu, "Simultaneous concentration measurement of vapour and liquid in an evaporating diesel spray," SAE Paper 930863 (1993)
- [20] H.M. Ney, B. Johansson, M. Aldén, "Cycle-resolved two-dimensional laser-induced fluorescence measurements of fuel/air ratio correlated to early combustion in a spark-ignition engine," Proceedings of the NATO Advanced Study Institute on Unsteady Combustion, Praia da Granja, Portugal, Kluwer Academic Publishers (1993)
- [21] L.A. Melton, "Soot diagnostics based on laser heating," Appl. Opt. **23**, 13 (1984)
- [22] C.J. Dasch, "Continuous-wave probe laser investigation of laser vaporization of small soot particles in a flame," Appl. Opt. **23**, 13 (1984)
- [23] J.E. Dec, A.O. zur Loye, D.L. Siebers, "Soot distribution in a DI diesel engine using 2-D laser-induced incandescence imaging," SAE Paper 910224 (1991)
- [24] J.E. Dec, "Soot distribution in a DI diesel engine using 2-D imaging of laser-induced incandescence, elastic scattering and flame luminosity," SAE Paper 920115 (1992)
- [25] C. Espey, J.E. Dec, "Diesel engine combustion studies in a newly designed optical-access engine using high-speed visualization and 2-D laser imaging," SAE Paper 930971 (1993)
- [26] R.L. Vander Wal, K.J. Weiland, "Laser-induced incandescence: development and characterization towards a measurement of soot-volume fraction," Appl. Phys. B **59**, 445-452 (1994)
- [27] A.C. Eckbreth, "Effects of laser-modulated particle incandescence on Raman scattering diagnostics," J. Appl. Phys. **48**, 11 (1977)
- [28] A.C. Eckbreth, "Laser diagnostics for temperature and species in unsteady combustion," Proceedings of the NATO Advanced Study Institute on Unsteady Combustion, Praia da Granja, Portugal, Kluwer Academic Publishers (1993)
- [29] P.O. Witze, "In-cylinder diagnostics for production spark-ignition engines," Proceedings of the NATO Advanced Study Institute on Unsteady Combustion, Praia da Granja, Portugal, Kluwer Academic Publishers (1993)
- [30] J. Luque, D.R. Crosley, "LIFBASE: database and spectral simulation program (version 1.0)," SRI International Report MP 96-001 (1996)
- [31] J.R. Reisel, C.D. Carter, N.M. Laurendeau, "Einstein coefficients for rotational lines of the (0,0) band of the NO $A^2\Sigma^+ - X^2\Pi$ system," J. Quant. Spectrosc. Radiat. Transfer **47-1**, 43-54 (1992)
- [32] P.H. Paul, J.A. Gray, J.L. Durant Jr., J.W. Thoman Jr., "A model for temperature-dependent collisional quenching of NO $A^2\Sigma^+$," Appl. Phys. B **57**, 249-259 (1993)

- [33] H. Zacharias, J.B. Halpern, K.H. Welge, "Two-photon excitation of $\text{NO}(\text{A}^2\Sigma^+; v'=0,1,2)$ and radiation lifetime and quenching measurements," *Chem. Phys. Lett.* **43**, 1 (1976)
- [34] H. Zacharias, A. Anders, J.B. Halpern, K.H. Welge, "Frequency doubling and tuning with $\text{KB}_5\text{O}_8 \cdot 4\text{H}_2\text{O}$ and application to $\text{NO}(\text{A}^2\Sigma^+)$ excitation," *Opt. Comm.* **19**, 1 (1976)
- [35] M. Asscher, Y. Haas, "The quenching mechanism of electronically excited Rydberg states of nitric oxide", *J. Chem. Phys.* **76**, No. 5 (1982)
- [36] H. Scheingraber, C.R. Vidal, "Fluorescence spectroscopy and Franck-Condon-factor measurements of low-lying NO Rydberg states", *J. Opt. Soc. Am. B* **2**, No. 2 (1985)
- [37] H. Scheingraber, C.R. Vidal, "Measurement of Hönl-London factors on $^2\Sigma^+ \rightarrow ^2\Pi$ transitions in NO," *J. Chem. Phys.* **83-8**, 1985
- [38] J.W. Thoman Jr., J.A. Gray, J.L. Durant Jr., P.H. Paul, "Collisional electronic quenching of $\text{NO A}^2\Sigma^+$ by N_2 from 300 to 4500 K", *J. Chem. Phys.* **97**, No. 11 (1992)
- [39] M.C. Drake, J.W. Ratcliffe, "High temperature quenching cross sections for nitric oxide laser-induced fluorescence measurements", *J. Chem. Phys.* **98**, 3850-3865 (1993)
- [40] M.P. Lee, B.K. McMillin, R.K. Hanson, "Temperature measurements in gases by use of planar laser-induced fluorescence imaging of NO," *Appl. Opt.* **32**, 27 (1993)
- [41] M.J. Frost, M. Islam, I.W.M. Smith, "Infrared-ultraviolet double resonance measurements on the temperature dependence of rotational and vibrational self-relaxation of $\text{NO}(\text{X}^2\Pi, v=2, j)$," *Can. J. Chem.* **72**, 606-611 (1994)
- [42] R. Zhang, D.R. Crosley, "Temperature dependent quenching of $\text{A}^2\Sigma^+$ NO between 215 and 300 K", *J. Chem. Phys.* **102**, No. 19 (1995)
- [43] A.M. Wodtke, L. Huwel, H. Schlüter, G. Meijer, P. Andresen, H. Voges, "High-sensitivity detection of NO in a flame using a tunable ArF excimer laser", *Opt. Lett.* **13**, 910 (1988)
- [44] M. Versluis, M. Ebben, M. Drabbels, J.J. ter Meulen, "Frequency calibration in the ArF excimer laser tuning range using laser-induced fluorescence of NO," *Appl. Opt.* **30**, 5229 (1991)
- [45] M. Versluis, M. Boogaarts, R. Klein-Douwel, B. Thus, W. de Jongh, A. Braam, J.J. ter Meulen, W.L. Meerts, G. Meijer, "Laser-induced fluorescence imaging in a 100 kW natural gas flame," *Appl. Phys. B* **55**, 164-170 (1992)
- [46] B.E. Battles, R.K. Hanson, "Laser-induced fluorescence measurements of NO and OH mole fraction in fuel-lean, high-pressure (1-10 atm) methane flames: fluorescence modelling and experimental validation", *J. Quant. Radiat. Transfer* **54**, 521-537 (1995)
- [47] J.R. Reisel, N.M. Laurendeau, "Quantitative LIF measurements and modelling of nitric oxide in high-pressure $\text{C}_2\text{H}_4/\text{O}_2/\text{N}_2$ flames", *Combustion and Flame* 101: 141-152, Elsevier Science Inc. (1995)
- [48] M.S. Klassen, D.D. Thomsen, J.R. Reisel, N.M. Laurendeau, "Laser-induced fluorescence measurements of nitric oxide formation in high-pressure premixed methane flames", *Combust. Sci. and Tech.* **110-111**, 229-247 (1995)

-
- [49] A.O. Vydrov, J. Heinze, M. Dillmann, U.E. Meier, W. Stricker, "Laser-induced fluorescence thermometry and concentration measurements on NO A-X (0,0) transitions in the exhaust gas of high-pressure CH₄/air flames," *Appl. Phys. B* **61**, 409-414 (1995)
- [50] J.R. Reisel, W.P. Partridge Jr., N.M. Laurendeau, "Transportability of a laser-induced fluorescence calibration for NO at high pressure", *J. Quant. Radiat. Transfer* **53**, 165-178 (1995)
- [51] R. Loudon, "The quantum theory of light," 2nd edition, Clarendon Press, Oxford (1983)
- [52] A.A. Radzig, B.M. Smirnov, "Reference data on Atoms, Molecules and Ions," Springer Series in Chem. Phys. Vol. 31 (1985)
- [53] A.M. Versluis, "Combustion diagnostics at atmospheric pressures using a tunable excimer laser," Ph.D. Thesis, University of Nijmegen, The Netherlands (1992)
- [54] M.P. Lee, R.K. Hanson, "Calculations of O₂ absorption and fluorescence at elevated temperatures for a broadband argon-fluoride laser source at 193 nm," *J. Quant. Spectrosc. Radiat. Transfer*, 425 (1986)
- [55] B. Dillies, K. Marx, J.E. Dec, C. Espey, "Diesel engine combustion modelling using the coherent flame model in Kiva-II," SAE Paper 930074 (1993)
- [56] W. Demtröder, "Laser spectroscopy, basic concepts and instrumentation," 2nd enlarged edition, Springer Verlag, Berlin (1995)
- [57] K.P. Huber, G. Herzberg, "Molecular spectra and molecular structure. IV. Constants of diatomic molecules," Van Nostrand-Reinhold, New York (1979)
- [58] Th.M. Brugman, J.J. ter Meulen, NOVEM report Dept. of Molecular and Laser Physics, University of Nijmegen (1993)
- [59] G.G.M. Stoffels, private communication
- [60] J.B. Heywood, "Internal combustion engine fundamentals," McGraw-Hill Book Co., international edition, Singapore (1988)
- [61] H. Pitsch, H. Barths, N. Peters, "Modellierung der Schadstoffbildung bei der dieselmotorischen Verbrennung," ESYTEC Energie- und Systemtechnik GmbH, Erlangen, Germany (1997)
- [62] M. Versluis, G. Meijer, "Intra-cavity C atom absorption in the ArF excimer laser tuning range," *J. Chem. Phys.* **96**, 3350-3351 (1992)
- [63] G.-S. Kim, L.M. Hitchcock, E.W. Rothe, G.P. Reck, "Identification and imaging of hot O₂(v''=2, 3, or 4) in hydrogen flames using 193 nm- and 210 nm-range light," *Appl. Phys. B* **53**, 180-186 (1991)
- [64] A.M. Wodtke, L. Huwel, H. Schlüter, H. Voges, G. Meijer, P. Andresen, "Predissociation of O₂ in the B state," *J. Chem. Phys.* **89**, 1929-1935 (1988)
- [65] J.E. Dec, R.E. Canaan, "PLIF imaging of NO formation in a DI diesel engine," SAE Paper 980147 (1998)
- [66] G.G.M. Stoffels, E.-J. van den Boom, C.M.I. Spaanjaars, N. Dam, W.L. Meerts, J.J. ter Meulen, J.L.C. Duff, D.J. Rieckard, "In-cylinder measurements of NO formation in a diesel engine," SAE Paper in preparation (1998)

Summary

The non-intrusive two-dimensional detection of nitric oxide (NO) in the cylinder of a diesel engine by means of laser-induced fluorescence (LIF) is the central theme of this thesis. Chapter 1 provides a general introduction including a brief discussion of the underlying environmental considerations as well as an overview of the laser-based imaging diagnostics in i.c. engines as reported in the literature. In the same chapter the LIF spectroscopy of NO is discussed in detail and the dependence of the LIF signal to several parameters is studied on the basis of a two-level rate equation model. This chapter concludes with an overview of the imaging techniques used in the experiments discussed in this thesis. The principal components of the experimental setup are described in great detail in chapter 2. Some of the issues discussed there have turned out to be crucial for the success of the experiments as reported in the subsequent chapters. In chapter 3 the results of the first imaging experiments in the idling engine are reported for two different fuels: n-heptane and standard diesel fuel. Besides the in-cylinder NO fluorescence distributions at various crank angles presented in this chapter, excitation spectra recorded from in-cylinder NO at atmospheric pressure using the respective fuels are also reported. In chapter 4 the detection method is further validated on the basis of a number of experiments in the standard-diesel-fuel-driven engine testing the various underlying assumptions. The sensitivity of the LIF signal to photo-chemically-induced effects possibly arising from the use of a high-power UV excimer laser, is investigated by means of a double-resonance experiment. The dependence of the LIF signal on the actual laser power is experimentally verified as well. The degree as to which saturation might occur at the in-cylinder laser intensities pertinent to this work, is estimated using data and relations found in the literature. Finally, in this chapter image-processing methods are introduced which enable the correction of imaged NO fluorescence distributions for both soot-deposits on the windows and in-cylinder laser extinction. In chapter 5 these image-processing methods are applied to NO fluorescence distributions recorded at various crank angles and loads of the diesel-fuel-driven engine. The sensitivity of the 2D-LIF signal to the local gas temperature is calculated using Boltzmann statistics. In the absence of data on the in-cylinder temperature distributions, the pixel-averaged LIF intensities found in the corrected fluorescence distributions are subsequently corrected for overall temperature effects and collisional quenching on the basis of a simplified fluorescence model. The resulting curves of the NO density versus the crank angle (i.e., in-cylinder pressure) at various loads are calibrated by comparing the densities at BDC (atmospheric pressure) with the corresponding tail-pipe densities as recorded by a NO_x -monitor. Both the reproducibility of the combustion and the experimental error are assessed on the basis of a statistical criterium. This chapter also contains two NO excitation spectra recorded from the loaded engine at atmospheric pressure and at an in-cylinder pressure of 0.5 MPa, respectively. The reliability of the fluorescence model used in chapter 5 is studied in more detail in chapter 6 on the basis of a large set of excitation spectra recorded from various NO sample gases in a high-pressure high-temperature cell. In these experiments both broadband and narrow-band fluorescence detection are used as to investigate the effects of interfering fluorescence from other molecules than NO. The pressure-broadening of the NO $R_1(24.5)/Q_1(30.5)$ D-X resonance as directly observed in the spectra is compared with

the broadening as derived from the fluorescence model. According to this model, the comparison of the observed LIF peak intensities at atmospheric pressure for the various NO sample gases provides a way to determine the NO D-X quenching cross section ratio of these sample gases. The results of this evaluation for the various dominant resonances is compared to values found in literature. Finally, the last chapter of this thesis provides an overview of and a context for the results of the experiments reported in this work as well as some remarks and recommendations with respect to the future imaging experiments.

Samenvatting

Het centrale thema van dit proefschrift is de twee-dimensionale detectie van stikstofmonoxyde (NO) in de cilinder van een dieselmotor middels laser geïnduceerde fluorescentie (LIF). Hoofdstuk 1 bevat een algemene inleiding van het onderwerp alsmede een korte beschouwing van de milieu-overwegingen die aan dit onderzoek ten grondslag liggen. Tevens bevat dit hoofdstuk een overzicht van de meest gebruikte laser-diagnostische afbeeldingstechnieken in verbrandingsmotoren zoals die beschreven zijn in de literatuur over dit onderwerp. Ook de LIF-spectroscopie van NO wordt uitgebreid behandeld en aan de hand van een twee-niveaus rate equations model wordt voor diverse parameters de afhankelijkheid van de intensiteit van de fluorescentie nagegaan. Het hoofdstuk wordt afgesloten met een beschrijving van de afbeeldingstechnieken die zijn gebruikt bij de experimenten die in dit proefschrift beschreven worden. Op de eigenschappen van de belangrijkste componenten van de meetopstelling wordt zeer uitgebreid ingegaan in hoofdstuk 2. Sommige onderwerpen uit dit hoofdstuk zijn cruciaal gebleken voor het succes van de experimenten zoals ze in de verschillende volgende hoofdstukken aan de orde zullen komen. In hoofdstuk 3 worden de resultaten van de eerste experimenten in de stationair draaiende motor beschreven voor een tweetal brandstoffen: n-heptaan en gewone dieselolie. Buiten de in de cilinder gemeten NO fluorescentiebeelden bij verschillende krukashoeken, worden in dit hoofdstuk ook de met de beide brandstoffen corresponderende excitatiespectra zoals gemeten bij atmosferische druk gepresenteerd. In hoofdstuk 4 wordt de detectiemethode verder gevalideerd door de verschillende aannamen te testen aan de hand van een aantal experimenten in de op dieselolie draaiende motor. De gevoeligheid van het LIF signaal voor fotochemie, die mogelijk zou kunnen optreden door het gebruik van een hoog-vermogen UV excimer laser, wordt onderzocht met behulp van een dubbelresonantie experiment. Ook is voor het LIF signaal de afhankelijkheid van het laservermogen in de cilinder experimenteel nagegaan. De mate waarin verzaadiging een rol zou kunnen spelen bij de gebruikte laservermogens wordt afgeschat aan de hand van gegevens en verbanden zoals die in de literatuur te vinden zijn. Tot slot worden er in dit hoofdstuk beeldverwerkende methoden gepresenteerd waarmee het mogelijk is om de oorspronkelijk gemeten NO fluorescentieverdelingen te corrigeren voor zowel de roetaanslag op de vensters als voor de optredende verzwakking van de laserintensiteit in de cilinder. In hoofdstuk 5 worden de beeldverwerkende methoden losgelaten op NO fluorescentieverdelingen gemeten bij verschillende krukashoeken en belastingen van de op dieselolie draaiende motor. Door het gebrek aan gegevens over de temperatuursverdelingen in de cilinder worden de gemiddelde pixelwaarden, zoals aangetroffen in de gecorrigeerde fluorescentieverdelingen, op basis van een vereenvoudigd fluorescentiemodel achtereenvolgens gecorrigeerd voor globale temperatuurseffecten en effecten van de botsingsgeïnduceerde quenching (letterlijk vertaald: afknijpen) van de fluorescentie. De resulterende NO dichtheden als functie van de krukashoek (lees: de druk in de cilinder) bij de verschillende belastingen worden gecalibreerd door de verkregen dichtheden bij atmosferische druk aan het eind van de expansieslag te vergelijken met de met behulp van een NO_x-meter gemeten dichtheden in het uitlaatgas. Ook wordt aan de hand van een statistisch criterium zowel de reproduceerbaarheid van de verbranding als de experimentele fout bepaald. Dit hoofdstuk bevat tevens twee NO excitatiespectra die in de belaste motor

gemeten zijn bij, respectievelijk, atmosferische druk en een druk van 0,5 MPa. De betrouwbaarheid van het in hoofdstuk 5 gebruikte fluorescentiemodel wordt uitgebreid onderzocht in hoofdstuk 6 aan de hand van een grote collectie NO excitatiespectra gemeten in een aantal NO gasmengsels bij verschillende drukken en temperaturen in een speciaal daartoe ontworpen gesloten meetcel. Teneinde de storende invloed van fluorescentie van andere moleculen te bepalen zijn deze experimenten uitgevoerd met zowel breedbandige als smalbandige fluorescentiedetectie. De in de verschillende spectra waargenomen drukverbreding van de NO $R_1(24,5)/Q_1(30,5)$ D-X resonantie wordt vergeleken met de drukverbreding die volgt uit het fluorescentiemodel. Volgens dit model kunnen de verhoudingen van de NO D-X quenchingswaarschijnlijkheden voor de verschillende gasmengsels worden bepaald door de maximale LIF intensiteiten bij atmosferische druk met elkaar te vergelijken. Voor de belangrijkste D-X resonanties wordt het resultaat van deze vergelijkingen getoetst aan de gevonden literatuurwaarden. Tenslotte worden in het afsluitende hoofdstuk 7 de belangrijkste resultaten van dit proefschrift in een breder perspectief gezet en tevens worden er enige kanttekeningen gemaakt en een aantal aanbevelingen gedaan ten aanzien van toekomstige experimenten.

Appendix

Engine make: HATZ-Samofa (1956)
Engine type: single-cylinder 4-stroke IDI diesel engine
Bore, stroke, swept volume: 86 mm, 100 mm, 580 cc

Originally rated power: 6 kW
Maximum power after modification: 1.8 kW (n-heptane), 0.9 kW (diesel fuel)
Compression ratio after modification: 1:9 - 1:8
Effective compression volume after modification: 70 - 80 cc
(including leakage along the optical ports)

Full optical access: $> 70^\circ$ ATDC
Crank position timing accuracy: 1.2° CA
Engine lubricant: Fomblin Y-25 (Montedison, Italy)

Oxygen-enrichments: 10 - 15 vol%
Exhaust gas temperatures: 250°C @ no load, 400°C @ 0.8 kW load

Inlet valve timing: opens at 1.5° BTDC, closes at 18° ABDC
Exhaust valve timing: opens at 23° BBDC, closes at 1.5° BTDC
Fuel injection starts at 15° BTDC

Curriculum Vitae

Ik ben geboren op 20 juli 1952 in Amsterdam waar ik het grootste deel van mijn jeugd heb doorgebracht. In 1970 heb ik het eindexamen HBS-B behaald aan het Keizer Karel College te Amstelveen. Vervolgens ben ik Technische Natuurkunde gaan studeren aan de toenmalige Technische Hogeschool Twente in Enschede. Omdat ik na 4 jaar door allerlei prettige omstandigheden nog steeds niet mijn propadeuse had gehaald leek het iedereen het beste om er maar een punt achter te zetten en ben ik gaan werken voor de kost. In de periode 1974-1985 heb ik verschillende beroepen uitgeoefend, waarvan ik er drie wil noemen: van 1975 tot 1977 ben ik Röntgen-laborant geweest in een streekziekenhuis in Oldenzaal en aansluitend heb ik tot 1984 in de buitendienst gewerkt als service-engineer voor kopieerapparatuur met als rayon geheel Noord- en Oost-Nederland. In die jaren reed ik gemiddeld zo'n 120.000 km per jaar en uit die tijd stamt vermoedelijk ook mijn liefde voor dieselmotoren. Daarna volgde een korte periode waarin ik als free-lance componist van elektronische film- en theater-muziek het hoofd boven water heb getracht te houden. Uiteindelijk ben ik in 1985 opnieuw begonnen met de studie Natuurkunde aan de Katholieke Universiteit Nijmegen, waar ik in 1991 afstudeerde aan de afdeling Moleculen en Laser-Fysica op een foto-akoestisch onderwerp. Van september 1991 tot maart 1996 heb ik in dienst van de KUN en de Stichting Technische Wetenschappen (STW) onder begeleiding van Prof. Dr. J.J. ter Meulen, Dr. W.L. Meerts en Dr. N. Dam gewerkt aan het promotie-onderzoek, waarvan de resultaten in dit proefschrift beschreven zijn.

Op 28 april 1992 ben ik met Joke Pannekoek getrouwd. Op 16 juni 1996 is onze zoon Boris geboren en op 23 oktober 1997 kwam onze dochter Bethany ter wereld.

Publications

F.G.C. Bijnen, Th.M. Brugman, F.J.M. Harren and J. Reuss in Photo Acoustic and Photo Thermal Phenomena III, edited by D. Bicanic (Springer Verlag, Heidelberg, 1992) 34-37.

Th.M. Brugman, R. Klein-Douwel, G. Huigen, E. van Walwijk and J.J. ter Meulen, "Laser-induced fluorescence imaging of NO in an n-heptane- and diesel-fuel-driven diesel engine", Appl. Phys. B 57, 405-410 (1993).

Th.M. Brugman, G.G.M. Stoffels, N. Dam, W.L. Meerts and J.J. ter Meulen, "Imaging and post-processing of laser-induced fluorescence from NO in a diesel engine", Appl. Phys. B 64, 717-724 (1997).

STELLINGEN

I

On the evidence of at least some of the unfiltered images presented in the most recent publication of J.E. Dec *et al.*, their statement that the in-cylinder attenuation of the laser intensity is not significant primarily seems to be based on wishful thinking.

J.E. Dec, R.E. Canaan, SAE Paper 980147 (1998)

II

In their rush to present high-pressure NO LIF distributions in internal combustion engines, some authors clearly fail to produce any convincing spectroscopic evidence that the presented LIF images do actually and exclusively originate from NO.

III

Whether the application of the 2D-LIF NO detection method to internal combustion engine studies poses an intrusion or not, mainly depends on the construction of the optical ports as well as on the degree of realism for the engine operating conditions.

Chapters 4 and 7 of this thesis

IV

The future translation of in-cylinder NO densities into NO_x concentrations will require additional experimental data on the oxidation-chemistry of NO under the conditions prevailing in diesel engines.

V

In internal combustion engine studies the information contained in cycle-averaged images and in single-shot images is essentially different.

VI

Considering the about an order of magnitude longer lifetime of the electronically excited NO A state when compared with the NO D state, the fluorescence from the latter state will be the least affected by collisional quenching.

A.A. Radzig, B.M. Smirnov, Springer Series in Chem. Phys. Vol. 31 (1985)

VII

De verplichte jaarlijkse roetest voor dieselmotoren is op zich een goede zaak, echter de meting van de roetuitstoot bij hoge toerentallen van een onbelaste motor is niet representatief voor de werkelijke uitstoot en leidt tot absoluut onaanvaardbare risico's voor de voertuigbezitter.

VIII

In de wintermaanden veroorzaakt de uitstoot van koude katalysatoren tijdens de eerste paar gereden kilometers niet alleen oogirritaties bij de andere weggebruikers maar bovendien zal de toegebrachte schade over de gemiddelde afstanden in het stadsverkeer, ondanks het toenemend stagneren daarvan, niet of nauwelijks worden gecompenseerd door de verminderde schadelijkheid van de uitstoot wanneer de katalysatoren eenmaal opgewarmd zijn.

IX

De gestaag voortschrijdende verloedering van de Nederlandse taal wordt sterk in de hand gewerkt door om de paar jaren de spelling te veranderen.

X

De bereikbaarheid van Nijmegen vanuit het Noorden tijdens de spits getuigt van werkelijk briljant ambtelijk bestuur indien men de term Knooppunt Arnhem-Nijmegen (KAN) letterlijk wenst op te vatten.

XI

Het met een hoger geluidsvolume uitzenden van reclameboodschappen op televisie bevordert slechts het gebruik van de mute- of zenderkeuzeknop van de afstandsbediening.

XII

Het handhaven van snelheidsbeperkingen bij wegwerkzaamheden terwijl er niet gewerkt wordt en de doorgang niet wezenlijk belemmerd is, geeft aanleiding tot onnodige filevorming en ergernis.

Theo Brugman, november 1998